

Aus der
Kinderchirurgischen Klinik und Poliklinik im Dr. von Haunerschen Kinderspital
Klinikum der Ludwig-Maximilians-Universität München



**Identifying therapeutic agents targeting NFE2L2/KEAP1-mutated
pediatric liver tumors**

Dissertation
zum Erwerb des Doctor of Philosophy (Ph.D.)
an der Medizinischen Fakultät
der Ludwig-Maximilians-Universität München

vorgelegt von
Andrei Rotari

aus
Chishinau / Republik Moldau

Jahr
2025

Mit Genehmigung der Medizinischen Fakultät der
Ludwig-Maximilians-Universität München

Erstes Gutachten:	Prof. Dr. Roland Kappler
Zweites Gutachten:	Prof. Dr. Irene Schmid
Drittes Gutachten:	Prof. Dr. Markus Guba
Viertes Gutachten:	Prof. Dr. Gerald Denk

Dekan:	Prof. Dr. med. Thomas Gudermann
--------	---------------------------------

Tag der mündlichen Prüfung: 02.09.2025

Table of content

Table of content	2
Abstract:	5
List of figures	7
List of abbreviations	8
1. Introduction	11
1.1 Hepatoblastoma.....	12
1.1.1 Etiology.....	12
1.1.2 Genetic mutations and epigenetic aberrations	13
1.1.3 Clinical features and diagnosis of HB	14
1.1.4 Histology.....	15
1.1.5 Staging and molecular risk stratification	16
1.1.6 Treatment regimens.....	17
1.2 The NFE2I2-KEAP1 pathway	19
1.3 Aim of the study.....	22
2. Material and Methods	23
2.1 Material.....	23
2.1.1 Antibodies.....	23
2.1.2 Buffers and solutions.....	23
2.1.3 Cell culture material	25
2.1.4 Cell lines and patient-derived xenografts (PDX)	26
2.1.5 Kits	27
2.1.6 Laboratory equipment	27
2.1.7 Reagents, chemicals, plasmids.....	29
2.1.8 Software.....	32
2.2 Methods	33
2.2.1 Apoptosis assay.....	33
2.2.2 Cell sorting.....	33
2.2.3 Cell culture.....	34
2.2.4 cDNA synthesis.....	35
2.2.5 Colony formations assay.....	35
2.2.6 Connectivity map (CMap)	35
2.2.7 DNA extraction	36
2.2.8 Genotyping of GFP positive cells	36
2.2.9 Growth curve assay	37
2.2.10 H&E staining.....	37
2.2.11 Immunofluorescence on frozen samples	37
2.2.12 Immunofluorescence in cells	37

2.2.13 Live and death staining of three-dimensional tumor spheroids	38
2.2.14 MTT viability assay	38
2.2.15 Mycoplasma test	39
2.2.16 Plasmid design	39
2.2.17 Proliferation assay	41
2.2.18 Real Time Polymerase Chain Reaction	42
2.2.19 Reporter assay	42
2.2.20 RNA extraction	43
2.2.21 RNA Sequencing	43
2.2.22 Real Time Quantitative Polymerase Chain Reaction	44
2.2.23 Sanger sequencing	44
2.2.24 Spectrophotometer – ND 1000 NanoDrop	45
2.2.25 Stable Transfection	45
2.2.26 Statistical analysis	46
2.2.27 Western blot	46
3. Results	49
3.1 Main mutations identified in a cohort of 189 hepatoblastoma patients	49
3.2 Clinical and transcriptomic insights into NFE2L2 mutated hepatoblastoma patients	50
3.3 Characterization of cell lines and patient derived xenografts used within this study	52
3.4 CRISPR-Cas9 engineering of NFE2L2 and KEAP1 clones	55
3.5 <i>NFE2L2</i> and <i>KEAP1</i> disruption enhances NFE2L2 activity and target gene expression	59
3.6 Morphology and growth analysis in WT versus NFE2L2 or KEAP1 models	62
3.7 <i>NFE2L2</i> and <i>KEAP1</i> mutations increase resistance towards cisplatin and doxorubicin	63
3.8 Validation of NFE2L2 and KEAP1 mutant models using RNA sequencing and Gene Set Enrichment Analysis (GSEA)	65
3.9 <i>In silico</i> drug prediction identifies Na ⁺ /K ⁺ -ATPase inhibitors as a novel class of drugs against NFE2L2 activated pediatric liver cancers	66
3.10 NFE2L2 target genes are downregulated upon treatment with ATPase inhibitors	68
3.11 Protein levels upon treatment with bufalin	69
3.12 Bufalin inhibits short/long term proliferation, reduces tumor spheroid growth and induces apoptosis in HepT1 cells	71
3.13 Bufalin re-establishes sensitivity towards cisplatin or doxorubicin in NFE2L2 activated cells	73
3.14 ATPase inhibitors are predicted using RNA sequencing data derived from NFE2L2 mutated patients	75

3.15	AKR1B10 is a promising biomarker clinically relevant in NFE2L2/KEAP1 mutated hepatoblastoma patients	77
4.	Discussion	81
4.1	Perspectives and future directions	85
	References.....	87
	Supplementary figures	95
	Acknowledgements.....	102
	Affidavit.....	104
	Confirmation of congruency	105
	List of publications	106

Abstract:

Hepatoblastoma (HB) is the most common pediatric liver cancer, with the *CTNNB1* gene being the most mutated one (88%). Other mutated genes reported are *NFE2L2* (5%) and *KEAP1* (1%), which are known to confer chemoresistance and poor prognosis to the patients. These mutations disrupt the regular NFE2L2-KEAP1 axis, leading to a constitutive activation of NFE2L2-ARE signaling with enhanced transcription of downstream genes that confer resistance towards standard chemotherapy. As the treatment options for this subgroup of patients still rely on standard chemotherapy, we aimed to identify a novel therapeutic strategy to circumvent drug resistance in this group of patients. Moreover, we wanted to identify a reliable biomarker to improve stratification of these patients prior to their treatment.

Relying on the CRISPR-Cas9 gene editing system we generate six NFE2L2 and four KEAP1-mutated cell models mimicking the mutations found in patients. After an extensive characterization of the cellular models through genotyping, Western blotting, localization of NFE2L2 protein, NFE2L2 activity, proliferation rate and, most importantly, response towards standard chemotherapy, our findings indicate that we have generated a robust set of cellular models that mimic the patient's condition. Using transcriptomic profiles of three NFE2L2 mutated patients and our ten cellular models, we integrated these data into a drug prediction tool known as Connectivity Map, which identified ATPase inhibitors as a potential therapeutic class of drugs to be used in NFE2L2 activated cancers. Among all ATPases, bufalin, a cardiac glycoside, emerged as the most promising compound due to its strong anti-tumor effects. Our experiments proved that bufalin significantly inhibited long and short-term proliferation, induced apoptosis, and restored cisplatin and doxorubicin sensitivity in our NFE2L2/KEAP1-mutated models. Mechanistically, we found that bufalin downregulated NFE2L2 and KEAP1 mRNA and protein levels, likely through a negative feedback loop. Therefore, the combination of bufalin with standard chemotherapy presents a novel strategy to tackle chemoresistance in NFE2L2/KEAP1-mutated HB patients. These comprehensive findings warrant further preclinical and clinical evaluation of bufalin as an alternative treatment regimen for this subgroup of patient.

In parallel, we wanted to identify a possible biomarker to facilitate future identification and stratification of NFE2L2/KEAP1-mutated HB patients. Relying on our RNA sequencing data derived from the patients and the models we observed a set of eight consistently upregulated genes, with *AKR1B10* being the most significantly expressed.

Therefore, we performed immunofluorescence analysis on different types of pediatric liver cancers, including HB, and found that the patients that carried NFE2L2 mutations expressed moderate to high levels of AKR1B10, suggesting its potential as a promising biomarker candidate.

In summary, within this study we identified bufalin as the most promising drug candidate to be used in combination with standard chemotherapy in NFE2L2/KEAP1-mutated HB patients to resensitize cells to chemotherapy. Moreover, we propose AKR1B10 as a novel and reliable biomarker candidate to identify this subgroup of patients in larger cohorts. Altogether, our findings offer a novel and attractive avenue for the identification and treatment of NFE2L2/KEAP1-mutated HB patients.

List of figures

Figure 1 Incidence and mortality of cancers in the world.	11
Figure 2 Protein structure of NFE2L2, KEAP1 and regulation of NFE2L2.	20
Figure 3 HB mutation landscape and domain mapping of NFE2L2/KEAP1.....	49
Figure 4 Transcriptomic analysis of NFE2L2-mutated HB patients.	51
Figure 5 Characterisation of cell line and PDXs used within the study.....	53
Figure 6 Flow chart of CRISPR-Cas9 editing system.....	56
Figure 7 Characterisation of NFE2L2 and KEAP1 models.....	57
Figure 8 NFE2L2 localisation, activity and AKR1B10 expression in mutants.	60
Figure 9 Morphology and growth in WT and mutant cells.	63
Figure 10 Drug response in the models towards cisplatin and doxorubicin.....	64
Figure 11 Transcriptomic profiling and GSEA of NFE2L2/KEAP1 mutants.....	65
Figure 12 In silico drug prediction using NFE2L2/KEAP1 models.	67
Figure 13 AKR1B10 expression in mutants upon treatment with ATPases.	68
Figure 14 Effects of ATPases inhibitors on NFE2L2 pathway, AKR1B10, and viability in HepT1 cells.	70
Figure 15 Cellular consequences in HepT1 cells upon treatment with bufalin.	72
Figure 16 Bufalin enhances cytotoxic effects of cisplatin and doxorubicin in the models.	74
Figure 17 Drug prediction and gene expression analysis in NFE2L2-mutated patients.	76
Figure 18 AKR1B10 protein localisation in parental, mutant cells and human liver cancer tissues.	78
Figure 19 Genetic alterations in NFE2L2/KEAP1 mutated patients.	95
Figure 20 Identification of gRNAs in NFE2L2 gene using ChopChopTool.....	95
Figure 21 Plasmid maps of designed vectors.....	96
Figure 22 Commonly up-regulated genes in NFE2L2/KEAP1 models.	96
Figure 23 Lists of top 50 up-regulated genes fed into CMap.	98
Figure 24 Hallmarks of bufalin against cancer.	98
Figure 25 16 human liver cancer tissues analysed using H&E and IF.....	101

List of abbreviations

5-FU	5-Fluorouracil
ABCB1	ATP-Binding Cassette Subfamily B Member 1
AFP	Alfa Fetoprotein
AKR1B10	Aldo-Keto Reductase Family 1 Member B10
ALT	Alternative Lengthening of Telomers
APC	Adenomatous Polyposis Coli
AREs	Antioxidant Response Elements
ATP	Adenosine Triphosphatase
AXIN1/AXIN2	Axis inhibition protein 1/Axis inhibition protein 2
β -hCG	β -human chorionic gonadotropin
β -TrCP	beta-Transducin Repeat-Containing Protein
bp	base pair
BTB	Broad complex-Tramtrack-Bric-a-brac
BWS	Beckwith–Wiedemann Syndrome
Calcein-AM	Calcein-Acetoxymethyl
Cas9	CRISPR-associated protein 9
CMap	Connectivity Map
CHIC	Children's Hepatic tumors International Collaboration
CLB	Cell Lysis Buffer
CNC	Cap'n'Collar
COG	Children's Oncology Group
CRISPR	clustered regularly interspaced short palindromic repeats
CTNNB1	Catenin-beta 1
DEGs	Differentially Expressed Genes
ddH ₂ O	double distilled water
DGR	Double Glycine Repeat
dH ₂ O	distilled water
DMSO	Dimethyl Sulfoxide
DMEM	Dulbecco's Modified Eagle Medium
DNA	Deoxyribonucleic Acid
dNTPs	Deoxynucleotide Triphosphates
DOD	Death Of Disease
DPBS	Dulbecco's Phosphate Buffered Saline
DTT	1,4-Dithiothreitol
D3T	1,2 dithiole 3 thione
EDTA	Ethylendiamine tetraacetic acid
EdU	Ethynyl Deoxyuridine
EMA	European Medicine Agency
FAP	Familial Adenomatous Polyposis
FBS	Fetal Bovine Serum
FDA	Food and Drug Administration
FPKM	Fragments Per Kilobase of transcript per Million mapped reads
GCL	Glutamate–Cysteine Ligase

GCO	The Global Cancer Observatory
GFP	Green Fluorescent Protein
GPOH	German Society for Pediatric Oncology and Hematology
GSEA	Gene Set Enrichment Analysis
GSH	Glutathione
GSK3 β	Glycogen Synthase Kinase 3 Beta
GSTs	Glutathione S-Transferases
HB	Hepatoblastoma
HEM-NOS	Hepatocellular malignant neoplasm, Not Otherwise Specified
H&E	Hematoxylin and Eosin
HCC	Hepatocellular Carcinoma
HDR	Homology-Directed Repair
HMOX1	Heme Oxygenase-1
IARC	International Agency for Research on Cancer
IF	Immunofluorescence
IGFBP3	Insulin-like Growth Factor Binding Protein 3
ISL	Isoliquiritigenin
IVR	Intervening Region
JPLT	Japanese Study Group for Pediatric Liver Tumors
KEAP1	Kelch Like ECH Associated Protein 1
KD	knockdown
LB	Lysis Buffer
LOF	Loss Of Follow-up
mRNA	messenger RNA
MTT	3-(4,5-dimethylthiazol-2-yl)-2,5-diphenyltetrazolium bromide
Neh	Nrf2-ECH homology
NES	Normalized Enrichment Scores
NFE2L2	Nuclear factor erythroid-derived 2-like 2
NQO1	NADPH Quinone Dehydrogenase 1
NRF2	Nuclear Factor (erythroid-derived 2)-like 2
OE	Overexpression
PAM	Protospacer Adjacent Motif
PBS	Phosphate Buffered Saline
PCR	Polymerase chain reaction
PDX	Patient-derived xenograft
PENSTREP	Penicillin-Streptomycin
PEI	Polyethylenimine
PFA	Paraformaldehyde
PHITT	Pediatric Hepatic International Tumor Trial
PI	Propidium Iodide
PKC	Protein Kinase C
PMSF	Phenylmethylsulfonyl fluoride
PL	Parthenolide
PRETEXT	PRETreatment EXTent of disease
RIN	RNA integrity number

RNA	Ribonucleic acid
RNA-seq	RNA sequencing
ROCK	Rho-associated protein kinase inhibitor
ROS	Reactive Oxygen Species
rpm	Revolutions Per Minute
RPMI	Roswell Park Memorial Institute
RT	Room Temperature
SCUD	Small Cell Undifferentiated
SD	Standard Deviation
SEM	Standard Error of the Mean
SF	Sulforaphane
SDS	Sodium dodecyl sulfate
sgRNA	single guide RNA
SIOPEL	Société Internationale d'Oncologie Pédiatrique
SSC	Side Scatter
STS	Sodium Thiosulfate
TBP	TATA box binding protein
TERT	Telomerase Reverse Transcriptase
WP	Wikipathways
WT	Wildtype

1. Introduction

In 2022 the International Agency for Research on Cancer (IARC), recorded a global incidence of cancer close to 20 million and a mortality related to cancer of 10 million (1). Six of the most common cancers (see **Fig. 1**), which occurs in males and females, contribute to 50% of newly diagnosed cancers and to 54% of deaths from cancer.

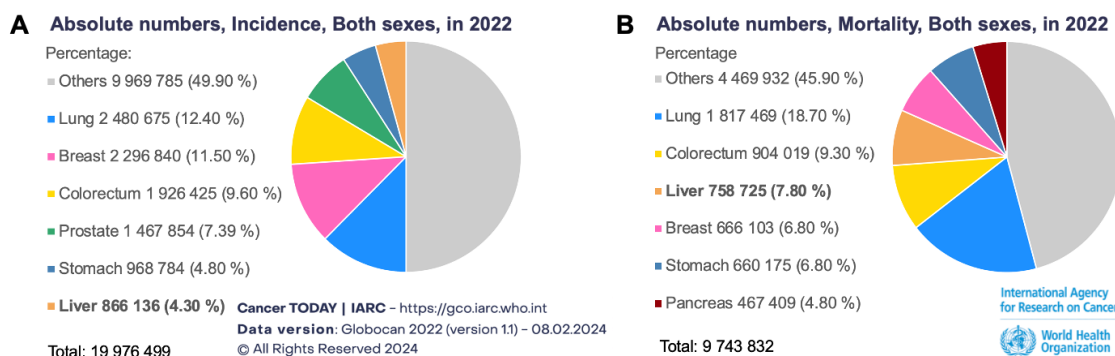


Figure 1 Incidence and mortality of cancers in the world. Pie charts displaying cancer absolute numbers for both sexes in 2022 for A incidence and B mortality. Data retrieved from The Global Cancer Observatory (GCO) (<https://gco.iarc.fr/en>).

The most diagnosed cancer worldwide is lung cancer with a total of 12.4% cases, followed by breast (11.5%), colorectal (9.6%), prostate (7.4%), stomach (4.8%) and liver cancer (4.3%) (1). Furthermore, cancer deaths are mainly caused by lung cancer (18.7%), subsequently in descending order: colorectum (9.3%), liver (7.8%), breast (6.9%), stomach (6.8%) and pancreas cancer (4.8%) (1). With growing population and increasing life span, new cancer incidence is projected to reach 35 million by 2050. This increasing cancer challenge poses a significant threat to public health and economy. This means that it is important to implement effective prevention and cancer treatment protocols to reduce disease incidence, improve survival rates, lower healthcare costs and enhance quality of life.

As reported by the Global Cancer Observatory (GCO) database, liver cancer is listed as the 6th leading type of cancer throughout the world and the 3rd leading cause of cancer-associated mortality (see **Fig. 1**) (1). There are different type of liver cancers, nevertheless, 90% of all liver cancers reported are represented by hepatocellular carcinoma (HCC) which occurs in adults (2). In contrast, hepatoblastoma (HB) is the most common malignant hepatic tumor in children under the age of five years old and it accounts for about 1% of all childhood malignancies (3).

1.1 Hepatoblastoma

1.1.1 Etiology

The yearly incidence of HB is about 1.2 to 1.5 cases per million children below the age of 15 years old, although most of the cases are diagnosed before the age of five as previously mentioned (4). The complete origin of HB is not clearly defined as many of the cases are sporadic however, some genetic disorder, environmental and development factors have been linked to HB.

For instance, children affected by Beckwith–Wiedemann Syndrome (BWS) have a higher risk (7.5%-10%) of developing childhood tumors which include HB, Wilms' tumor and neuroblastoma within the first four years of life (5, 6). A child with two or more of the following features (e.g., macroglossia, hemihypertrophy, omphalocele) is often suspected of having BWS. However, only genetic testing can confirm the diagnosis by identifying abnormalities in the chromosome 11p15 region, specifically in two imprinting centers (BWSIC1 and BWSIC2) (5).

HB has been also linked to familial adenomatous polyposis (FAP) syndrome (7). These patients carry genetic alteration in the adenomatous polyposis coli (*APC*) gene, that can cause an early development of colon cancer and increasing potential of HB occurrence within the first years of life compared to the general population (7, 8). Development of hundreds or more of adenomatous polyps in the colon can be triggered by FAP, which is an autosomal dominant condition (7).

Kabuki Syndrome, Neurofibromatosis Type 1, Prader–Willi Syndrome, trisomy 18 (Edwards Syndrome), Noonan Syndrome, Fanconi Anemia, Simpson–Golabi–Behmel Syndrome, Tyrosinemia Type 1, DiGeorge Syndrome, and Sotos Syndrome have been reported as rare genetic syndromes linked to HB, typically documented in only one or two cases (9, 10).

Epidemiological studies have highlighted several environmental risk factors involved in the initiation of HB. Maternal and paternal preconception smoking, for example, is tied to an increasing risk of HB, and IARC has classified parental tobacco smoke as a carcinogen for this condition (10-12). Additional factors include oxygen therapy, drugs like furosemide, total parenteral nutrition, exposure to radiation, plasticizers and other toxins, though the mechanisms underlying these associations remain unclear (12). Lastly, developmental factors like prematurity and low weight at birth have also been connected to an increased risk of HB (13).

1.1.2 Genetic mutations and epigenetic aberrations

In a previous study, 125 somatic mutations were identified across 15 HB patients, averaging 2.9 mutations per tumor (14). In addition, a study by Gröbner and colleagues analyzed a cohort of 961 tumors from children, adolescents, and young adults, representing 24 distinct molecular cancer types (15). The findings revealed that HB had the lowest number of coding mutations per megabase, marking HB as a very simple tumor.

A handful of genomic studies have established that most of the HB patients carry mutations in catenin-beta 1 (*CTNNB1*) gene (14, 16, 17). Most of the mutations occur in exon 3 as either point mutation or large deletion. These type of mutations usually occur in the amino-terminal domain of β -catenin, which affects phosphorylation sites essential for its degradation (18). This results in the stabilization of β -catenin, preventing its normal proteasomal degradation and enabling its oncogenic activity.

As previously mentioned, *APC* mutations are associated with HB, specifically in the context of FAP. These mutations are germline mutations associated with FAP, or somatic mutations found in sporadic cases of HB (7, 19). *APC* mutations impair the formation of the β -catenin destruction complex, preventing β -catenin breakdown (19). Other sporadic mutations were found in axis inhibition protein 1 (*AXIN1*) gene and axis inhibition protein 2 (*AXIN2*) gene (20, 21). These mutations were primarily located in functional domains of AXIN1 and AXIN2, including regions that bind key components like APC, GSK3 β , and β -catenin (20, 21). Disruption of AXIN1 and AXIN2 function leads to an inability to degrade β -catenin.

The Wnt signaling pathway is an important system activated during embryogenesis that is fundamental in the early liver development. A series of processes like cell proliferation, differentiation, survival and migration are regulated by Wnt signaling pathway (22). Therefore, impairment of Wnt signaling can contribute to several diseases, particularly to cancer. Mutations in key components like β -catenin, APC, or AXIN often result in abnormal activation of the pathway. In other words, mutations in either *CTNNB1*, *APC* or *AXIN1/AXIN2* disrupt the normal breakdown of β -catenin, facilitating its accumulation and relocation to the nuclear compartment. Inside the nuclear compartment the binding of β -catenin to transcription factors including lymphoid enhancer factor (LEF) or T-cell factor (TCF), promotes oncogenic gene expression and tumorigenesis (19, 23).

Another frequently mutated gene in liver cancers, including HB, is the nuclear factor erythroid-derived 2-like (*NFE2L2*) gene, reported to have heterozygous point mutations within exon 2 (14, 17, 24, 25). A less frequently mutated gene is the Kelch-like ECH-

associated protein 1 (*KEAP1*) gene, which has recently been reported to be mutated in HB (25). *NFE2L2* or *KEAP1* mutations both result in constitutive activation of the NFE2L2 pathway with overexpression of its target genes resulting in metabolic changes in the cells, leading to reduced response to chemotherapy in cancer patients (26). As *NFE2L2* and *KEAP1* mutations are the central focus in this study, the detailed regulation of NFE2L2 will be discussed in section 1.2 of the introduction.

An additional altered gene found in HB with HCC-like features and poor prognosis is telomerase reverse transcriptase (*TERT*) gene (14, 17, 25). At the ends of eukaryotic chromosomes, telomeres are present, which are nucleoprotein complexes ensuring chromosomal integrity (27). With every cell division the telomeres gradually shorten if there is no telomerase activity which results in cell aging and eventually death (27). Cancer cells found a way to maintain telomere length allowing them to divide indefinitely. This is achieved in two ways; either through mutations in the TERT promoter, which increase telomerase activity or through alternative lengthening of telomeres (ALT), both resulting in unlimited cell division (28, 29).

Other rare mutations in HB have also been identified in genes such as *FGFR3*, *PIK3CA*, *CAPRN2* and several genes related to the ubiquitin ligase complex such as *RNF169*, *ARID1A*, *TRPC4AP*, *MLL2*, *KLHL22* and *SPOP* (17, 30-32).

Epigenetic aberrations have also been described in HB, especially through hypermethylation of gene promoters that lead to the silencing of tumor suppressor genes. For instance, Eichenmüller and colleagues reported hypermethylation of the hedgehog interacting protein (*HHIP*) promoter, a negative regulator of the Hedgehog signaling pathway, which results in pathway activation and driving HB growth and progression (33). Regel and colleagues reported in metastatic HB patients with vascular invasion a hypermethylation of the insulin-like growth factor binding protein 3 (*IGFBP3*) promoter that leads to its silencing (34).

Many cancers, including HB, display whole chromosome aneuploidy often with additions of chromosomes 1, 2, 8 and 20 and loss of chromosomes 4, 11 and 18 (14, 16, 17, 32, 35).

1.1.3 Clinical features and diagnosis of HB

A patient with HB, generally presents an abdominal mass that is found by the parents or the physician (36). In addition, other systemic symptoms can be observed which may

include generalized fatigue, weight loss, vomiting, thrombocytosis, symptoms of peritoneal irritation, and severe anemia (36, 37). Generally, high alpha-fetoprotein (AFP) serum levels are found in roughly two thirds of the HB patients (7). AFP remains the most important clinical marker for the clinical diagnosis and subsequent tracking of the response to the treatment or relapse in HB (37). Screening of AFP levels together with abdominal ultrasound and computed tomography scan is necessary to establish the extension of the condition (7, 38). Additionally, magnetic resonance imaging is employed for pre-surgical planning due to better soft tissue contrast, and even post-chemotherapy and surgery to evaluate the treatment (7).

For the clinicians, even though bilirubin and liver enzymes are usually normal, the presence in a patient of a hepatic mass together with high serum levels of AFP is already enough to make an initial diagnosis (36, 39). Of note, in rare cases a precocious puberty has been reported, this is due to secretion by the tumor of β -human chorionic gonadotropin (β -hCG) (37). After emphasizing that AFP is the most highly considered marker in HB, it's hard to define an exact range of serum levels that defines the stage of the disease. The Children's Hepatic Tumors International Collaboration (CHIC) has tried to define a risk stratification system based on AFP serum levels. Generally, AFP >1,000 ng/mL is observed in standard-risk HB patients, AFP 100–1,000 ng/mL is reported in intermediate risk, and finally AFP <100 ng/mL is linked to a poor outcome and it is often seen in aggressive tumor subtypes (37).

1.1.4 Histology

In 2011 the Children's Oncology Group (COG) together with the Japanese Study Group for Pediatric Liver Tumors (JPLT), the German Society for Pediatric Oncology and Hematology (GPOH) and the Société Internationale d'Oncologie Pédiatrique - International Childhood Liver Tumors Strategy Group (SIOPEL) organized the International Pathology Symposium in order to develop a unified classification system to improve diagnosis, risk stratification and therapeutic approaches of liver cancers in children. The teams involved in this research worked together towards a harmonized classification of tumor histopathology (40). According to SIOPEL, histologically HB can be divided into 3 main types; epithelial which occurs in 56% of the cases, epithelial and mesenchymal and hepatocellular malignant neoplasm not otherwise specified (HEM-NOS) which accounts for the rest 44% (see **Table 1**) (3, 40, 41).

Classification of HB according to SIOPEL

Whole epithelial type: this type includes subtypes
Fetal (including purely fetal HB)
Embryonal/mixed fetal and embryonal
Macrotrabecular
Small cell undifferentiated (SCUD) (formerly called anaplastic)
Cholangioblastic
Mixed epithelial and mesenchymal type
Stromal derivatives
Teratoid
HB not otherwise specified (HB-NOS)

Table 1. Table showing the classification of hepatoblastoma (HB) according to the International Childhood Liver Tumors Strategy Group - Société Internationale d'Oncologie Pédiatrique (SIOPEL). Table adapted from Terrada et al., 2014.

Each type can also be divided into subtypes, for the epithelial type we have a fetal pattern, a macrotrabecular, an embryonal, a small cell undifferentiated (SCUD) variant and finally a cholangioblastic variant formally discussed and refined during the COG Symposium in 2011 (3, 40). The mixed epithelial and mesenchymal type can be divided into 2 subtypes, without teratoid features or a teratoid variant (3, 40). One important note is that most of HBs are very heterogeneous, meaning there might be mixed histological components rather than a single histological type (40). Moreover, for a better diagnosis and prognosis of HB it is fundamental to do a histopathological analysis (42). For instance, HB cancers with predominantly fetal histology have been linked with a more favorable outcome, whereas HB cancers with predominantly embryonal or SCUD have been linked with a unfavorable outcome (43).

1.1.5 Staging and molecular risk stratification

Internationally different research groups are trying to optimize treatment of HB patients, this means that there are different staging systems. This implies that data comparison and collaboration is difficult. Hence, the CHIC collaboration has formed by the four major research groups; SIOPEL, COG, GPOH and JPTL. The end goal of CHIC was to establish a unified staging system for HB patients. By using data retrieved from 1,605 patients that received medical care in eight different multicentric HB trials over the course of 25 years, the CHIC collaboration aimed to generate an international common approach to staging and risk stratification of HB patients (44). Therefore, they used previously defined key

prognostic factors such as: PRETEXT (PRETreatment EXTent of disease) groups I–IV, AFP serum levels (≤ 100 ng/mL, 101–1,000, $> 1,000$ ng/mL), age at diagnosis (< 3 years, 3–7 years, ≥ 8 years) and PRETEXT annotation factors such as contiguous extrahepatic tumor (E), multifocal tumor (F), macrovascular involvement of all hepatic veins (V) or portal bifurcation (P), spontaneous rupture (R) and metastatic disease (M) (44, 45). They identified key combinations of factors that best predicted outcome, which ultimately led to the definition of four distinct risk categories: high, intermediate, low and very low.

Besides these staging criteria discussed, scientist tried to define some molecular markers and gene expression signatures to improve stratification of HB patients. In a publication by Cairo and colleagues two molecular subtypes of HB were defined, the C1 subtype with a late fetal liver, more differentiated, characterised by a less invasive phenotype and a favorable outcome (16). The C2 subtype is characterised by early embryonic liver, less differentiate, highly proliferative and clinically aggressive features (16). In order to distinguish between C1 and C2 subtype tumors a 16-gene signature was established. C2 tumors displayed an increased Myc signaling and stem-like features with high rates of infiltration into the vascular system, metastasis and unfavorable prognosis (16). Despite the effort to establish the 16-gene signature that has shown high potential to estimate outcome of the patients, it is yet not commonly used for risk assessment.

1.1.6 Treatment regimens

In 1970s the overall survival rate of HB patients was roughly about 30%. However, with the implementation of chemotherapy before or after surgery and novel surgical techniques (i.e. liver transplantation, hepatic exclusion and Pringle manoeuvre), the overall survival rate has reached over 70-80% (42, 45-48). This breakthrough was achieved not only because of new approaches to treat this highly malignant tumor, but also because of the successful collaboration between the four major research groups mention before: GPOH, JPLT, COG and SIOPEL. A handful of studies have proven that complete surgical resection or liver transplantation is the most important factor for a full tumor removal and associated with better outcome of the patients (48-51). Moreover, across multiple trials, cisplatin remains the backbone in both standard and high-risk patients (46, 48, 49, 51, 52). Additionally, risk stratification using the PRETEXT system has proven to significantly improve treatment and outcome of the patients (45, 51-53). In a study done by Perilongo and colleagues, it has been proven that standard-risk patients can be treated with cisplatin alone rather than combining cisplatin with doxorubicin (51). This approach

reduced the side effects coming from doxorubicin such as cardiotoxicity or even cardiomyopathy induced by free radical formation, mitochondrial damage and impaired calcium processing and sarcomere structure (54). Even though cisplatin-based chemotherapy has been key in improving the outcome and survival of HB patients over the last 30 to 40 years, cisplatin has been associated with toxicities. In particular, cisplatin can induce ototoxicity and eventual hearing loss in 25-90% of the children (55). The ototoxicity is thought to be caused through the generation of reactive oxygen species (ROS), inflammation and mitochondrial dysfunction that eventually leads to cell damage and apoptosis in the cochlea (56). Additionally, cisplatin has been proven to induce nephrotoxicity by damaging directly the glomeruli and renal tubular, impairing filtration and eventually leading to irreversible loss of kidney function (57).

The SIOPEL-1 study proposed a combination of cisplatin along with doxorubicin as a preoperative chemotherapy followed by surgical resection (36, 45). For the SIOPEL-2 study, the treatment strategies varied based on risk categories. For instance, the standard-risk patients were treated only with cisplatin, whereas the high-risk patients received alternative cycles of cisplatin and a combination of carboplatin and doxorubicin (46). The SIOPEL-3 study further intensified chemotherapy regimens for high-risk patients by using alternative cycles of cisplatin and carboplatin plus doxorubicin to improve response and achieve tumor resectability (48, 51). In SIOPEL-4 trial, high-risk patients were treated with intensive pre-operative chemotherapy by combining cisplatin with doxorubicin, followed by tumor resection or liver transplantation if necessary (47). However, if the tumors still remain unresectable after the initial treatment, additional cycles of carboplatin and doxorubicin were administered before surgery (47). The SIOPEL-6 trial determined whether addition of sodium thiosulfate (STS) given in combination with cisplatin could prevent hearing loss in children with standard-risk (58).

After SIOPEL-6, the international research groups GPOH, JPLT, COG and SIOPEL formed a consortium to work together in the Pediatric Hepatic International Tumor Trial (PHITT). The goal of this collaboration was to standardise, evaluate and refine treatment options for liver tumors in children including HB and HCC (<https://clinicaltrials.gov/study/NCT03017326>). The following drugs are being explored in the trial: cisplatin, carboplatin, doxorubicin, vincristine, irinotecan, etoposide, sorafenib, oxaliplatin, and 5-fluorouracil (5-FU). This trial recruited patients from 2017 to 2024 and enrolled 450 patients globally. Overall, this extensive clinical trial aims to reach significant advance in

understanding and management of pediatric liver cancers with a standardized worldwide therapeutic strategy based on risk stratification.

Overall, over the last 3 decades cisplatin, carboplatin and doxorubicin have remained the primary chemotherapeutic agents. Despite aggressive treatment regimens in high-risk patients, characterised by vascular invasion and metastasis, their survival rate still remains under 60%. (48). Therefore, there is an urgent need, already for 3 decades, for alternative therapeutic strategies for high-risk-patients.

1.2 The NFE2L2-KEAP1 pathway

The nuclear factor (erythroid-derived 2)-like 2 (NRF2) protein is encoded by the nuclear factor erythroid-derived 2-like 2 (*NFE2L2*) gene (59). NFE2L2 is a protein member of the Cap'n'Collar (CNC) family of basic leucine zipper (bZIP) transcription factors that plays an important role in the response towards oxidative stress (59, 60). The NFE2L2 protein is composed of seven Nrf2-ECH homology (Neh) domains, each one with a specific role (**Fig. 2 A**).

A NFE2L2 (605 AA)



B KEAP1 (624 AA)

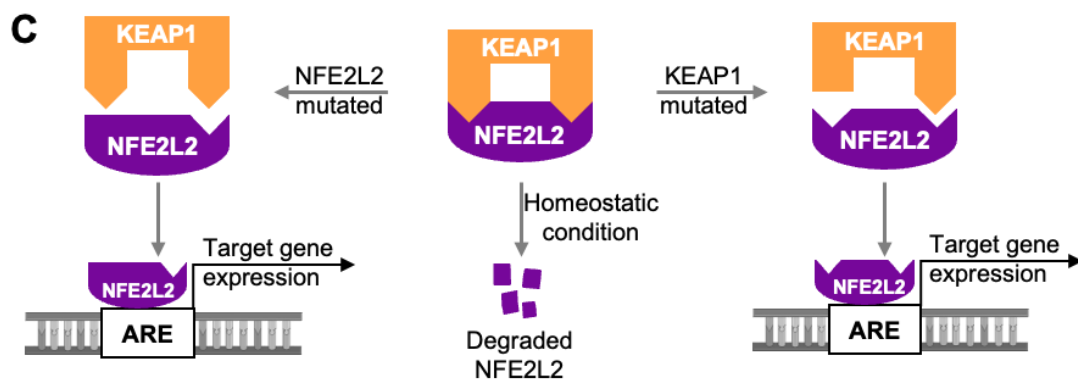


Figure 2 Protein structure of NFE2L2, KEAP1 and regulation of NFE2L2. **A** NFE2L2 protein consists of 605 amino acids and holds seven well-conserved functional domains, known as Neh1 to Neh7. The Neh2 domain is highlighted as it includes the DLG and ETGE motifs, which are fundamental for the binding to KEAP1. **B** KEAP1 protein is composed of 624 amino acids and is made of three important distinct domains: an intervening region (IVR), a broad complex-tramtrack-bric-a-brac (BTB) and a segment composed of six kelch repeats (KELCH domains). The KELCH domains are highlighted as they facilitate binding to NFE2L2. **C** Under homeostatic conditions, NFE2L2 interacts with two KEAP1 molecules via its Neh2 domain. The interaction between these two proteins results in polyubiquitination and proteasomal degradation of NFE2L2. In the presence of mutations in either NFE2L2 or KEAP1, this interaction is disrupted. As a result, NFE2L2 is not degraded but instead becomes stable and is transported in the nuclear compartment. Within the nuclear compartment, NFE2L2 interacts with specific regions known as anti-oxidant response elements (ARE), in turn this induces the transcription of genes involved in cellular defense mechanisms.

The Neh1 domain holds the CNC-bZIP region, this domain of the protein is involved in dimerization with small Maf proteins and binding to DNA (61-63). The Neh2 domain is the most important domain investigated within this project, because it contains two motifs (DLG with low affinity and ETGE with high affinity) that are prone to mutation and play a key role in binding to KEAP1 protein (61, 62, 64). The Neh3 domain acts as a transactivation domain via CHD6, it assists in transcriptional activation (63). The Neh4 and Neh5 are protein segments involved in transactivation via CBP/BRG1 (62, 65). The Neh6 domain contains two motifs (DSGIS and DSAPGS) rich of serines that can be phosphorylated by glycogen synthase kinase-3 beta (GSK-3 β) (64, 66). The phosphorylation enables NFE2L2 to bind to beta-transducin repeat-containing protein (β -TrCP) and form the Cul1 E3 ubiquitin ligase complex resulting in the degradation of NFE2L2 (64, 66). Lastly, the Neh7 domain is involved in repression of NFE2L2 activity through its interaction with retinoid X receptor alpha (RXR α) (67).

Under basal conditions, meaning in non-stressed healthy cells, NFE2L2 protein is localized in the cytoplasm and is recognized by the KEAP1-Cul3-Roc1 E3 ligase complex which adds ubiquitin tags to several lysin residues of the NFE2L2 protein (68). This ubiquitination marks NFE2L2 for proteasomal degradation. In the presence of oxidative stress (e.g. ROS), electrophiles, several chemical inducers (e.g. sulforaphane), or other signals,

NFE2L2 protein translocates to the nucleus (69, 70). In the nuclear compartment NFE2L2 interacts with antioxidant response elements (AREs) in the promoter regions of different genes coding for phase II detoxifying enzymes like glutathione S-transferases (GSTs) and NADPH quinone oxidoreductase 1 (NQO1) (69, 71). Peroxiredoxins and heme oxygenase-1 (HMOX1) are essential antioxidant enzymes activated by NFE2L2 (72-74). Additionally, NFE2L2 activates genes that produce glutamate-cysteine ligase (GCL), that is crucial for the synthesis of glutathione (GSH). (72-74).

NFE2L2 mutations were reported in vast range of cancers such as lung adenocarcinoma, squamous cell carcinoma, large cell neuroendocrine carcinoma, head and neck cancer, ovarian cancer, HB and HCC (14, 17, 24, 25, 75-77). These mutations impair NFE2L2 protein binding to KEAP1, leading to constitutive NFE2L2 activation (gain of function) and resistance to chemotherapeutic drugs (**Fig. 2 C**) (26, 75).

Three important segments are denoted inside the KEAP1 protein: an intervening region (IVR), a broad complex-tramtrack-bric-a-brac (BTB) and a domain composed of six kelch repeats (alternatively called KELCH domains) (**Fig. 2 B**). The IVR segment contains several cysteine residues that function as redox sensors (78-81). When these cysteines residues get oxidised by electrophiles or reactive oxygen species, they change the conformation of KEAP1 protein allowing it to disassociate from NFE2L2 (82). NFE2L2 eventually becomes stable and can translocate to the nuclear compartment (82). The BTB domain dimerizes KEAP1 and binds to Cul3, enabling KEAP1 to act as a substrate recruiter for the Cul3 E3 ubiquitin ligase complex (62, 78-80). BTB and IVR domains are both involved in Cul3 interaction. Lastly, the KELCH domains are composed of six kelch repeats that directly bind to NFE2L2 protein (62, 80, 83).

Genetic alteration in the *KEAP1* gene have been reported to occur in many cancers such as lung cancer, epithelial ovarian cancer, HCC and only recently in HB (25, 77, 79, 84, 85). KEAP1 mutations impair the function of important domains such as BTB or KELCH, which in turn results in loss of function of KEAP1 and no degradation of NFE2L2 protein (**Fig. 2 C**) (84, 85). Therefore, *KEAP1* mutations lead to enhance NFE2L2 activation, promote multidrug resistance, enhanced cancer cell growth and shorter survival of the patients (14, 17, 79, 84, 85).

Altogether, NFE2L2-ARE signaling activation can lead to either beneficial or detrimental outcomes based on the circumstances. On the beneficial side, NFE2L2 is able to help cells to protect from oxidative stress by expressing antioxidant and cytoprotective genes. On the detrimental side, persistent activation of NFE2L2-ARE signaling in cancer cells can

lead to tumor progression by enhancing cell proliferation, resistance to chemotherapy and metastasis. Given its central role in cancer development and progression, the KEAP1-NFE2L2 signaling pathway is a promising therapeutic target. Strategies to restore KEAP1 function or inhibit NFE2L2 hyperactivation are being explored.

1.3 Aim of the study

The survival rates of hepatoblastoma, a very rare and aggressive liver cancer diagnosed in children, has reached significant improvements over the last four decades through the introduction of chemotherapy and novel surgical techniques. However, there is a subgroup of patients that still faces poor outcome due to non-response towards standard treatments, which involve the use of cisplatin and doxorubicin. Several studies have identified that tumors carrying *NFE2L2* and *KEAP1* mutations are less likely to respond to chemotherapy.

Therefore, this study aims to identify a new therapeutic approach for patients carrying *NFE2L2* and *KEAP1* mutations. To address this, the CRISPR/Cas9 editing system will be used to develop several engineered models mimicking *NFE2L2* and *KEAP1* mutations found in HB patients. By using the transcriptomic profiles of these models and the drug predicting tool Connectivity Map, we aim to identify a novel drug to be used in patients carrying these mutations. In parallel to this study, we sought to identify a diagnostic biomarker to identify patients carrying these mutations early on and predict their drug response.

2. Material and Methods

2.1 Material

2.1.1 Antibodies

Abcam, Cambridge, UK

NFE2L2, host rabbit (EP18084) (ab62352)

Cell Signaling Technology, Danvers, Massachusetts, USA

β -Actin #4967, host rabbit

KEAP1 (D6B12), host rabbit (8047)

Dako Agilent Technologies, Santa Clara, CA, USA

Polyclonal Goat Anti-Mouse Immunoglobulins HRP

Polyclonal Goat Anti-Rabbit Immunoglobulins HRP

Invitrogen, Karlsruhe, Germany - Thermo Fisher, Waltham, MA, USA

GAPDH Monoclonal (6C5), host mouse

Goat anti-Rabbit IgG (H+L) Alexa Fluor Plus 647 highly cross adsorbed (A32733)

Gt anti-Rb IgG (H+L) super clonal secondary Alexa Fluor 555 conjugated (A27039)

Merck / Sigma Aldrich, Darmstadt, Germany

Alpha-Tubulin (clone DM1A) (T9026), host mouse

AKR1B10 (HPA020280), host rabbit

2.1.2 Buffers and solutions

Bradford dye 1x

- 10 ml Bradford dye 5x
- 40 ml dH₂O (distilled water)
- Filter

Cell lysis buffer (CLB)

- 1 ml LB
- 500 mM PMSF
- 2 mM DTT
- 1 mM Na₃VO₄
- 1 mM B-glycerophosphate
- 5 mM Sodium fluoride
- 50 μ l of protease inhibitor

Crystal violet solution

- 0.5% crystal violet
- 20% methanol
- 80% distilled H₂O

Freezing Medium

- 48.8% FBS
- 39% DMEM
- 12.2% DMSO

Lysis buffer (LB)

- 1.5 ml TrisHCl 30 mM (stock 1 M)
- 1.5 ml NaCl 150 mM (stock 4 M)
- 0.5 ml Triton-X (1 %)
- 5 ml Glycerol (10%)
- 1 tablet of proteinase inhibitor per 25 ml of LB
- Complete to 50 ml of PBS or dH₂O

MTT1 Solution

- Thiazolylblau (MTT, 3-(4,5-Dimethylthiazolyl-2)-2,5-diphenyl-2H-tetrazoliumbromid) 200 mg
- 40 ml of PBS
- Filter (40 µm)

MTT2 concentrated solution

- 4.15 ml 37 % HCl
- 45.85 ml H₂O

MTT2 Solution

500 µl of MTT2 concentrated solution

- Ad. 50 ml of SDS 10%

PBS-T

- 1 l of PBS 1x
- 1 ml of Tween 20

PBS 1x

- 1 l of PBS 2x
- 1 l of dH₂O

Proteinase K (10 mg/ml)

- 100 mg Proteinase K
- 10 ml of H₂O

SDS 10%

- 10 g SDS ultra pure
- Ad. 100 ml of H₂O

STE-Buffer

- 20 ml 5 M NaCl

- 100 ml 10 % 50 ml 1 M Tris pH 8 SDS
- 2 ml 0.5 M EDTA pH 8
- To a final volume of 1000 ml dH₂O

TBS-T Buffer 10X

- TBS
- 0.1% Tween 20

Tris-glycine –SDS Running Buffer 10X

- 14.4% glycine
- 3% Tris base
- 1% SDS
- pH 8.3-8.7

0.4% Triton X100

- 0.4 g of Triton X100
- Ad. 100 ml of PBS 1X

1x MES

- 50 ml of 20x MES
- Ad. 1 l dH₂O

3% BSA solution in PBS

- 3 g of BSA powder
- Ad. 100 ml of PBS 1X

4% PFA solution

- 4 g of PFA
- Ad. 100 ml of PBS 1X
- Warm to 60 °C
- Add NaOH crystals until the solution becomes clear
- Adjust final pH to 7.4 with HCl 37%

5 % milk

- 5 g of milk powder
- 100 ml PBS-T

2.1.3 Cell culture material

B. Braun, Melsungen, Germany

Gloves Vasco Nitril Soft blue

Omnifix 10 ml syringe

Corning, Corning, NY, USA

Costar Stripette Serologic Pipettes 5 ml, 10 ml, and 25 ml

Ultra-low attachment round-bottom 96-well plates

Epredia, Portsmouth, USA

Cover slips 24x24 mm

Microscope slides ground 45° frosted

Round cover slips 18 mm diameter

Feather Safety Razor Co., Ltd., Osaka, Japan

Feather disposable scalpel

Feather microtome blades S35 type

Greiner bio-one, Frickenhausen, Germany

Falcon tubes 15 ml and 50 ml

Greiner Bio-One, Kremsmünster, Austria

Easy strainer 40 µm

Invitrogen, Karlsruhe, Germany - Thermo Fisher, Waltham, MA, USA

Nunc CryoTube

NUNC, Langenselbold, GermanyCell culture T-Flasks 25cm², 75cm², and 175cm²

Petri dishes 100mm

Plates, non-pyrogenic, 6-well, 12-well, 24-well, 48-well, and 96-well

Omnilab, Bremen, Germany

Eppi's Safe-Lock farblos 1.5 ml and 2 ml

Pall life sciences, Port Washington, NY, USA

Syringe Filter 0.2 µm

Sakura color products corporation, Osaka, Japan

Tissue-Tek

Sarstedt AG & Co., Nümbrecht, Germany

Biosphere Filtertips 1-10 µl, 10-100 µl, and 100-1,000 µl

Cell scraper

VWR International, Darmstadt, Germany

Agarose, universal

2.1.4 Cell lines and patient-derived xenografts (PDX)

HepT1 human, liver, hepatoblastoma

(86)

HuH6 human, liver, hepatoblastoma

JCRB, Osaka, Japan

HuH7 human, liver, adult HCC

JCRB, Osaka, Japan

Hep3B human, liver, pediatric HCC	ATCC, Manassas, VA, USA
HepG2 human, liver, HEM-NOS	ATCC, Manassas, VA, USA
214 human, liver, hepatoblastoma	XenTech, Evry, France
303 human, liver, HEM-NOS	XenTech, Evry, France

2.1.5 Kits

Agilent Technologies Santa Clara, California, USA

Agilent RNA 6000 Nano Kit

LGC Standards, Teddington, Middlesex, UK

Universal mycoplasma detection kit

New England Biolabs, Durham, NC, USA

T4 DNA Ligase, 10x buffer for T4 DNA Ligase with 10 mM ATP

Promega Madison, Wisconsin, USA

Dual-Luciferase® Reporter Assay System

GoTaq® G2 Hot Start Taq Polymerase

QIAGEN Hilden, Germany

Plasmid Mini Kit

QIAquick Gel Extraction Kit

Thermo Scientific, Wilmington, DE, USA

CellEven Caspase-3/7 Green

Click-iT EdU Alexa Fluor 555 Imaging Kit

SuperScript II Reverse Transcriptase

2.1.6 Laboratory equipment

Agilent Technologies, California, USA

2100 Bioanalyzer

Assistent, Sondheim vor der Rhön, Germany

Counting chamber Neubauer Improved 0.100 mm depth

BD Biosciences, Franklin Lakes, New Jersey, USA

BD FACSAria III

Benchmark Scientific, Sayreville, New Jersey, USA

MyFuge™ Mini Centrifuge

BMG LABTECH, Offenburg, Germany

FLUOstar Omega

Eppendorf, Hamburg, Germany

Centrifuge 5702

Compact Mastercycler personal

Eppendorf / New Brunswick Scientific - Excella E24 incubator shaker series

Mastercycler realplex2 epgradient S

Research plus pipette 10, 100 and 1,000 µl

Thermomixer comfort

GFL, Wien, Austria

Water bath GFL1083

Heidolph, Schwabach, Germany

Heidolph MR 3001 with heating and magnetic stirrer

Intas Science Imaging, Göttingen, Germany

Intas UV-Systeme

Integra Biosciences, Zizers, Switzerland

Integra Assist

Integra Pipetboy 2

Lightweight Electronic Pipettes 125 and 1,250 µl

Invitrogen, Karlsruhe, Germany - Thermo Fisher, Waltham, MA, USA

Bio-Rad Hercules, California, USA

ChemiDoc RS+

EVOS M7000

Heraeus Fresco 17 Centrifuge

Mini-Sub Cell GT Cell Electrophoresis Systems

NanoDrop 1000

PowerPac Basic

Rolling system tube revolver

SimpliAmpo Thermal Cycler

Trans-Blot Turbo Transfer System

Wide Mini-Sub Cell GT Cell Electrophoresis Systems

XCell SureLock Blot Module

Leica, Wetzlar, Germany

Leica cryostat CM 1510-1

Kendro, Asheville, North Carolina, USA

Centrifuge Heraeus Biofuge pico

Herasafe Laminar flow safety cabinet

KERN, Frankfurt am Main, Germany

Scale EMB 600-2

Kisker-Biotech, Steinfurt, Germany

Arpege 140 air liquide

LMS, Brigachtal, Germany

Mini centrifuge Harmony MCF-2360

Merck / Sigma Aldrich Burlington, Massachusetts, USA

Hettich ROTANTA 460R centrifuge

Mettler-Toledo Columbus, Ohio, USA

pH Meter FiveEasy F20

Mitsubishi Marunouchi, Chiyoda, Tokyo

Mitsubishi Thermoprinter P93D

Sanyo, Tokyo, Japan

CO₂-Incubator MCO-20AIC

Fridge -80 °C MDF-U55V

Sartorius Göttingen, Germany

Scale TE124S

Scientific Industries, NY, USA

VortexGenie2

Tecan, Männedorf, Switzerland

Tecan Sunrise

ZEISS Oberkochen, Germany

Microscope Axiovert 40 CFL

2.1.7 Reagents, chemicals, plasmids

Addgene, Watertown, MA, USA

pSpCas9 (B.B)-2A-GFP

Apotheke Klinikum der Universität München, Munich, Germany

Phosphate-Buffered Saline (PBS) 2x

AppliChem, Darmstadt, Germany

Ethidium Bromide solution 1 % BioChemica

Glycerol

BioLegend, San Diego, CA, USA

Calcein-acetoxymethyl (Calcein-AM)

Bio-Rad Hercules, CA, USA

Bradford dye 5x

SsoAdvanced Universal SYBR Green Supermix

Trans-Blot Turbo Mini 0.2 µm PVDF Transfer Packs

Carl Roth, Karlsruhe, Germany

AquaCare

Bovines Serum albumin Fraktion V, NZ-Origin

Chloroform

Dry milk powder

DTT (1,4-Dithiothreitol)

Ethylenediaminetetraacetic acid (EDTA)

Hematoxylin

Hydrochloric Acid (HCl) 37%

LB-Agar (Luria/Miller)

LB-Medium (Luria/Miller)

Magnesium chloride

Phenol

ROTI Mount Aqua

RotiHistol

Sodium chloride

Sodium dodecyl sulfate (SDS) ultra pure

Sodium fluorid

Sodium hydroxide (NaOH)

Thiazolylblau

TrisHCl

DM-drogerie markt, Karlsruhe, Germany

Super shine & stay nail polish (transparent)

Dr. Masayuki Yamamoto, Tohoku University, Japan

pNQO1-ARE-Luc

H. Kerndl, Weissenfeld, Germany

Double distilled water (ddH₂O)

Invitrogen, Karlsruhe, Germany - Thermo Fisher, Waltham, MA, USA

Advanced Dulbecco's Modified Eagle Medium (DMEM) / F12 (1X)

Amersham ECL Prime Western Blotting Detection Reagent

BbsI

DH5α (Competent cells)

Dulbecco's Phosphate Buffered Saline (DPBS) (1X)

ExoSAP-IT™ reagent
Fetal Bovine Serum (FBS)
GeneRuler 100 bp
Hoechst 33342
Hydrophobic barrier pen
L-glutamine
LDS Sample buffer (4x)
MES SDS Running Buffer (20x)
Novex™ WedgeWell™ 4 - 20 %, Tris-Glycin, 1.0 mm x 12 well, Mini-Protein-Gel
PageRuler Prestained Protein Ladder
Penicillin-Streptomycin (PenStrep)
Restore Western Blot Stripping Buffer
Roswell Park Memorial Institute (RPMI) medium 1640 (1X)
S.O.C. Medium
SuperScript II Reverse Transcriptase
Trypsin-EDTA 0.05%
Ultra Pure Distilled Water DNase/RNase Free

Merck / Sigma Aldrich, Darmstadt, Germany

Ampicillin
 β -glycerophosphate
Crystal violet
Dimethyl sulfoxide (DMSO)
Eosin
Ethanol
Glas Beads
Isopropyl alcohol
Paraformaldehyde
Phenylmethanesulfonyl fluorid (PMSF)
Polyethylenimine branched
Proteinase K 10 mg/mL
Propidium Iodide (PI)
Sodium azide 0.1 M solution
Sodium orthovanadate (Na_3VO_4)
3-(4,5-dimethylthiazol-2-yl)-2,5-diphenyltetrazolium bromide (MTT)
TRI Reagent
Triton X100
Trypan Blue solution
Tween 20

New England Biolabs, Durham, NC, USA

T4 Polynucleotide Kinase (PNK)
T4 Polynucleotide Kinase buffer 10x
1 kb DNA ladder

Nippon Genetics, Tokyo, Japan

Midori Green Advance DNA Stain

Promega, Madison, WI, USA

FuGENE HD Transfection Reagent

pRL-CMV vector

Roche, Basel, Switzerland

dNTPs (Deoxynucleoside Triphosphate Set)

Primer random p(dN)₆

Selleckchem, Chesterbrook, PA, USA

Bufalin

Cisplatin

Digoxin (NSC 95100)

Doxorubicin

Y-27632, Rho-associated protein kinase inhibitor (ROCK)

Tocris, Bristol, United Kingdom

Ouabain

2.1.8 Software

GraphPad, La Jolla, CA, USA

GraphPad Prism 8.2.1

Technelysium Pty Ltd, South Brisbane, Australia

Chromas

Microsoft, Redmond, WA USA

Office 2016

Eppendorf Hamburg, Germany

Realplex 2.2

Bio-Rad Hercules, CA, USA

Image Lab 6-0-1

CMap Broad Institute Cambridge, MA, USA

CMap version 1.1.1.43 Tool Query

Invitrogen, Karlsruhe, Germany - Thermo Fisher, Waltham, MA, USA

Evos Analysis

NIH, Bethesda, MD, USA

ImageJ

Bioconductor open source software for bioinformatics

Bioconductor package DESeq2

Intas Science Imaging, Göttingen, Germany

INTAS GelDoc

SnapGene, Boston, MA, USA

SnapGene Viewer 4.1.5

Serial cloner open source free software

Serial cloner 2.6.1

BMG LABTECH, Offenburg, Germany

Omega software version 5.11 R3

Tecan, Männedorf, Switzerland

Magellan software version 7.2

2.2 Methods

2.2.1 Apoptosis assay

1×10^5 cells are seeded in 1,000 μ l/well in a 24-well plate. 24 h later cells are treated with the desired compound and vehicle. Afterwards, based on the supplier's instructions CellEvent Caspase-3/7 Green Detection Reagent is used to detect apoptotic cells, by identifying cells expressing active caspase-3/7 substrates. Cells are counterstained using Hoechst 33342 (with a dilution of 1:1,000, and a final concentration of 0.01 mg/ml). Using EVOS M7000 imaging system representative images are captured.

2.2.2 Cell sorting

24-48 h after transfection start selection by sorting the cells that express green fluorescent protein (GFP) (cells were priorly transfected with pSpCas9(B.B)-2A-GFP plasmid). Transfected cells that are in the 24-well plate are trypsinized with 200 μ l of trypsin, collected with 3 ml PBS 2% FBS solution in a falcon tube. Cells are spinned down for 5 min at 1,500 rpm. Supernatant is sucked and cell pellet is dispersed at a final volume of 200 μ l with PBS 2% FBS. We also prepared a reference for each cell line which is purely a cell suspension of un-transfected 1×10^5 cells resuspended in 200 μ l of PBS supplemented with 2% FBS. For the sorting, BD FACSAria III machine is used with a nozzle of 100

µm in order to have a low pressure which results in less mechanical stress on the sorted cell.

2.2.3 Cell culture

The cell lines HepT1, Hep3B, HuH6, HuH7 and HepG2 are cultured in RPMI 1640 medium containing 1% (v/v) penicillin-streptomycin (PenStrep) and 10% (v/v) fetal bovine serum (FBS) at 37 °C in a humidified atmosphere with 5% CO₂. The patient-derived xenograft (PDX) cell lines 214 and 303 are grown in Advanced DMEM/F12 supplemented with 1% (v/v) PenStrep, 10% (v/v) FBS, 1% (v/v) L-glutamine and ROCK inhibitor at a final concentration of 20 µM.

Thawing cells

Retrieve a vial of cryopreserved cells from the liquid nitrogen tank and thaw the cells at 37 °C for 1 - 2 min. Using a pipette of 1,000 µL transfer cells into a falcon tube with 9 ml of prewarmed medium. Gently agitate the tube and centrifuge for 5 minutes at 1,400 revolutions per minute (rpm). Suck out most of the medium, resuspend the sedimented cells and gently transfer them into a 6-well plate or T25 flask based on the pellet containing either 2 or 5 ml of medium.

Splitting cells

Take out the flask from the incubator, suck out the media without touching the basal part of the flask, and introduce 2 ml of PBS for T25 flask (or 3 ml for T75). Wash the cells by gently shaking and suck out the PBS. Put 0.5 ml of trypsin into the T25 flask (or T75 1 ml) and keep cells in the incubator for 2 - 5 min to detach them from the flask. Dilute the trypsin with 3 ml medium (for T25), to stop the trypsin activity and split cells into new medium-containing flasks (for T25 5 ml, for T75 10 ml, and for T175 20 ml).

Counting cells

Prepare a cell suspension in fresh media by trypsinization and transfer 10 µl into a 1.5 ml tube containing 90 µl of Trypan Blue (dilution factor 1:10). Moisten the coverslip by exhaled breath and slide it over the hemocytometer. Fill one side of the hemocytometer with 10 µl stained cell suspension and view under the microscope using 20X magnification. Count the number of viable cells (seen as bright cells) and calculate their concentration using the following equation:

Viable cell count = [(number live cells counted) / (number of large squares in the hemocytometer counted)] x dilution factor x 10,000

Freezing cells

Trypsinize cells and transfer them to a 15 ml falcon tube. Spin down at 1,400 rpm for 5 min, remove media, and redisperse sedimented cells in 500 μ l 4 °C-cold serum free DMEM. Add ~10 ml 4 °C cold freezing medium and carefully resuspend cells by pipetting up and down. Aliquot quickly into cryovials and cryopreserve at –80 °C for 1-3 days before transferring to liquid nitrogen for long-term preservation.

2.2.4 cDNA synthesis

In a final volume of 7 μ l of DNase/RNase Free H₂O, 2 μ g of total RNA is diluted. Then pipette in 5 μ l of random hexamers (20 ng/ μ l) and incubate for 10 min at 70 °C. After this step add 1 μ l of dNTP mix (10 mM), 2 μ l of 0.1 M DTT and 4 μ l of 5x 1st strand buffer. The reaction is maintained at room temperature for 10 minutes, then incubated at 42 °C for 2 minutes. Subsequently, 1 μ l of SuperScript II reverse transcriptase is introduced, and the solution is gently mixed by pipetting gently up and down. Next, incubate at 42 °C for 1 h. Lastly, heat at 70 °C for 15 min, which will inactivate the reaction. Bring the final volume to 100 μ l using DNase/RNase Free H₂O and store cDNA at -20 °C.

2.2.5 Colony formations assay

In a 6-well plate 5×10^3 cells are seeded at a final volume of 2 ml. 24 h later the treatment with the desired compound and vehicle is started. 6 days later remove the medium and wash cells with 2 ml of PBS. Then 2 ml of crystal violet 0.5% solution is added and incubate at RT for 2 h. Discharge crystal violet solution and immerse the plates in a beaker full of tap water. Wash extensively until all crystal violet is removed. Lastly, air dry the plates on a table at RT. Capture images using any digital camera or for higher magnification use the 10X objective of EVOS M7000 imaging system.

2.2.6 Connectivity map (CMap)

Differentially expressed genes coming from the RNA sequencing are used for drug prediction using the map query tool from the Broad Institute version 1.1.1.43. To generate a query with a list of perturbagens, an alphanumeric name is given to the query and selected as query parameters “Gene expression (L1000)”, “Touchstone”, “individual query” and selected the “1.0” version available. In the next step the top 50 up regulated genes recognised by the query and organised by p-value are inserted. As a readout CMap gives a list of perturbagens made of gene knockdown or gene overexpression experiments or compounds.

2.2.7 DNA extraction

Adherent cells of a T25 flask are washed with PBS and then trypsinized. Cell pellet is then transferred into a 1.5 ml tube and 500 µl of STE-Buffer and 30 µl of Proteinase K solution (10 mg/ml) is added. Incubate the pellet at 55 °C for 2 – 3 h based on the pellet size. Afterwards, add 500 µl of phenol and hand mix for 5 minutes. Centrifuge at 4 °C for 10 min at 3,000 rpm. Take supernatant into a new 1.5 ml tube, then add 500 µl of chloroform and hand mix for 5 min. Now centrifuge again at 4 °C for 10 min at 3,000 rpm. Take supernatant into a 15 ml falcon tube and add 1,500 µl of ethanol absolute 99.8% and hand mix shortly. Leave it for 5 min at RT and DNA will precipitate. Take a new clean 1.5 ml tube and add 500 µl of ethanol 70%. Collect DNA pellet using a 1,000 µl pipette from the falcon tube to the small tube that contains 70% ethanol. Centrifuge for 10 min at 12,000 rpm. Trash the ethanol and air-dry DNA pellets putting the tube upside down. DNA pellet is dissolved in 50 - 150 µl of DNase/RNase Free H₂O based on pellet size. After this step the DNA concentration is measured by using a spectrophotometer.

2.2.8 Genotyping of GFP positive cells

5,000 sorted cells are seeded in a petri dish and left to recover after all the mechanical stress. After a week, depending on the proliferation rate of the cell line, individual colonies will be formed. Select a couple of colonies that radiate from a single center and pick them up using a 100 µl pipette, use half of it for genotyping and half for stock maintenance.

To the 50 µl cell suspension (for sequencing) add 45 µl of NaOH 50 mM. Now incubate at 100 °C for 15 min, then add 4 µl of Tris HCl pH 7.4 1M. From the mixture take 2 µl and perform RT-PCR. In the table below can be seen which primer pairs to use to sequence either the KEAP1 or NFE2L2 mutated clones. For the PCR always use a positive and a negative control; for the positive control use high molecular weight DNA, for the negative control use the PCR mixture without DNA. When you have a band in the agarose gel at the expected length, take 5 µl of the PCR product and clean it using ExoSAP-IT reagent according to the manufacturing protocol. Send the cleaned PCR product for sequencing with the forward primer.

Gene	Amplicon size	FWD: 5' ->3'	RV: 5' ->3'
KEAP1	381 bp	GCTACCTGGAGGCTTACAACC	TACCCGGATCTCAGTGTCTTG
NFE2L2	313 bp	GTAGACCCTTAGTAGTTTGA	GGTTCAGATCTTAGCTCCTC

2.2.9 Growth curve assay

Cells are starved prior to seeding for 24 h in serum free media and the following amounts of cells are seeded: for HepG2 and HuH6 5×10^3 , for HuH7 and Hep3B 2×10^3 , for 214 4×10^3 and 303 9×10^3 cells. 4h post seeding the first MTT-viability test is carried out marking time 0 h (see description in section 2.2.14 MTT viability assay). Viability test is carried out from this point at 24 h, 48 h, 72 h, 96 h and 120 h.

2.2.10 H&E staining

Cryosections, 5 μ m thick, are fixed in 4% PFA/PBS for 10 minutes and stained with hematoxylin for 4 min and eosin for 15 seconds. The slides are then mounted in RotiHistol. Next, images are captured using EVOS M7000 imaging system.

2.2.11 Immunofluorescence on frozen samples

From frozen patient samples, 5 μ m cryosections are generated using a cryostat and placed on a microscope slide. Cryosections on a slide are left to air dry for 5-10 min. For fixation, slides are incubated in 4% PFA (pH 7.4) for 15 min at RT. Slides are then washed 3 times for 5 min with ice-cold 1xPBS. For permeabilization, incubate the slides in 0.5% Triton X100 for 60 min at RT. For blocking, incubate the slides in PBS-T with 3% BSA for 30 min at RT. Next, air dry the slides, use hydrophobic barrier pen to mark the borders around the tissue to be stained. Incubate slides with primary antibody overnight at 4 °C in a humidified chamber. The day after wash the slides with PBS 3 times for 5 min. Then add secondary antibody for 1 h at RT. If needed counterstain with Hoechst 33342 (dilute 1:1,000, final concentration of 10 μ g/ml). Remove secondary antibody and wash 3 times for 5 min. Let slides dry and add mounting media ROTI Mount Aqua and seal the slides with a cover slip and nail polish around. Capture images using the EVOS M7000 imaging system.

2.2.12 Immunofluorescence in cells

Round glass cover slips (18 mm in diameter) are washed before in EtOH, then in PBS and finally placed in a 12 well plate. In general, 1×10^5 cell are seeded per well and allowed for 24 h to attach to the cover slips. As cells tend to cluster in the middle of the cover slip, try to distribute equally by mixing and distributing the cells dropwise. Once cells are attached (24 h later), cells can be treated/transfected or just directly stained depending on the experimental setup. Old media is removed and cells are washed with 1x PBS. Then 300 μ l of 4% PFA is added directly on the cover slip and incubated for 10 - 15 min. PFA

is removed and cells are washed 3 times with PBS for 5 min. Next 300 μ l of Triton X100 is added and incubated for 15 - 20 min. Next, remove Triton X100 and wash 3 times with PBS for 5 min. For blocking, add 250 μ l of 3% BSA (diluted in PBS-T) for 30 min. Blocking solution is removed and cells are washed with PBS-T for 5 min. Carefully remove the cover slips from the 12-well plate and let them dry for 10 - 20 min with the cells facing up. Mark the periphery of the cover slips with a hydrophobic barrier pen and wait 20-30 min to dry. Next, add the primary antibody diluted in 3% BSA PBS-T solution (approximately 50-100 μ l are required for one cover slip). Incubate cover slips in a humidified chamber at 4 °C overnight. The day after, remove primary antibody and wash with PBS 3 times for 5 min. Determine the correct Alexa fluor conjugated secondary antibody to use based on the host of primary antibody. Add the secondary antibody and Hoechst 33342 (diluted 1:1,000, final concentration of 0.01 mg/ml) diluted in 3% BSA PBS-T solution and incubate for 1 - 2 h at RT in the dark. Wash secondary antibody with PBS 3 times for 5 min. Place the cover slips on a flat surface and let them dry for 15 min in the dark. Add one drop of ROTI Mount Aqua on the slide and mount the cover slips. Let the cover slip to settle for 20 - 30 min and then seal with nail polish. Try to avoid dust, fiber or air bubbles during sealing. Capture images using EVOS M7000 imaging system.

2.2.13 Live and death staining of three-dimensional tumor spheroids

To obtain three-dimensional spheroids, 1×10^3 cells in 100 μ l are seeded per well into ultra-low attachment round-bottom 96-well plates and maintained in humidified incubator for 5 days. On the fifth day media is refreshed, representative pictures are captured and spheroids are treated with either 100 nM of bufalin or DMSO (marking day 0 of treatment). Three days post treatment, spheroids are washed with PBS once and representative pictures are captured. Afterwards, dead and viable cells are assessed by co-staining three-dimensional spheroids with 2.5 μ g/ml propidium iodide (PI; to visualise dead cells) and 1 μ M Calcein-AM (to visualise viable cells) at 37 °C for 20 minutes. Before imaging, spheroids are washed twice with PBS. Additionally, analysis of spheroid volume on the third day is measured using the following formula $V = [(L) \times (W)^2] / 2$ (87). EVOS M7000 is employed to capture all microscopy images.

2.2.14 MTT viability assay

Cells are seeded in 96-well plates at a density of 25×10^3 cells/well in culture media. 24 h later cells are treated with vehicle and selected drugs at defined concentration for each

cell line. 72 h later from the treatment, the culture media is taken out and 100 µl/well of MTT1 solution is added to the cells. 4h later 100 µl/well of MTT2 solution is added and incubated overnight at 37 °C in the incubator. The day after absorbance is measured at 595 nm using Tecan Sunrise plate reader.

2.2.15 Mycoplasma test

To ensure that all cell lines and PDXs used for this project are Mycoplasma negative we used the LGC Standards Universal mycoplasma detection kit and followed the manufacturer's protocol.

2.2.16 Plasmid design

sgRNA - oligonucleotide design

Copy provided sequence (e.g. a 1 kb relevant genomic locus) or put the gene name into ChopChopTool (<https://chopchop.cbu.uib.no/>) and select best target site with zero off-target effects. As input into ChopChopTool the gene target is pasted, then Homo sapiens (hg38/GRCh38) as species, using CRISPR-Cas9 for generating knockout. Add a CACC overhang to the 5'-end of the top and a AAAC overhang to the 5'-end of bottom oligonucleotide and order them from Eurofins (<https://eurofinsgenomics.eu/de/>). According to the Ran and colleagues' guidelines, if the backbone uses a human U6 promoter to drive expression, it is recommended to add a guanine (G) to the start of the target sequence (88). But if the target sequence already starts with a G there is no need to add it. We targeted two genes of interest, *NFE2L2* and *KEAP1*. Regarding the *NFE2L2* gene we designed 2 plasmids, targeting the introns flanking exon 2. In principle transfecting the cells with these two plasmids at the same time would allow deleting exon 2 completely. The position for the *KEAP1* sgRNA is designed according to the publication by Zheng and colleagues (89). Oligonucleotides designed for each gene can be seen in the table below:

Gene	Top (with overhang in red)	Bottom (with overhang in red)
NFE2L2 intron 1-2	5' CACCGTG - TAGCGTTCCGTGACAGTG 3'	5' AAACCACTGTCACGGAACGC - TACAC 3'
NFE2L2 intron 2-3	5' CACCGAT - TACTGGCGTTACTGTGTG 3	5' AAACCACACAGTAACGCCAG - TAATC 3'
KEAP1	5' CACCA GCGTGCCCCGTAACCG- CAT 3'	5' AAACATGCGGTTACGGGGCAC - GCT 3'

Oligonucleotide Annealing and Phosphorylation

Lyophilized top and bottom strand oligonucleotides are dissolved to a final concentration of 100 µM using Ultra Pure Distilled Water DNase/RNase Free. To anneal and phosphorylate the sgRNA the following solution is prepared:

Component	Amount (μl)
sgRNA top (100 μM)	1
sgRNA bottom (100 μM)	1
T4 Polynucleotide Kinase Reaction Buffer, 10x	1
T4 PNK (polynucleotide kinase)	1
DNase/RNase Free H ₂ O	6
Total	10

In a thermocycler, oligonucleotides are phosphorylated and annealed. The following steps are taken; 37 °C for 30 min, followed by 95 °C for 5 min and finally ramp down to 25 °C at 5 °C per min. Phosphorylated and annealed oligonucleotides are diluted 1:200 with 1 μl (10 μM) of annealed oligonucleotides to 199 μl of RT (room temperature) DNase/RNase Free H₂O (final concentration of 0.05 μM).

Plasmid linearization and gel extraction

As described, the subsequent mixture is prepared for linearizing the pSpCas9(B.B)-2A-GFP vector:

Component	Amount (μl)
plasmid	4 (=2 μg)
10x G buffer	2
BbsI	2
DNase/RNase Free H ₂ O	12
Total	20

Set a thermocycler at 37 °C for 4 h and run digested plasmid on a 1% agarose gel. If you are going to perform gel extraction, always use ethidium bromide for the gel, not the alternatives such as Midori Green. Next, following the supplier's instructions from QIAquick gel extraction kit, the linearized plasmid from the gel is isolated.

Ligation

Prepare the following mixture for ligating the double-stranded and annealing sgRNA oligonucleotides into the linearized plasmid:

Component	Amount (μl)
Linearized plasmid	4 (100 ng)
Diluted oligo duplex (1:200)	2 (0.05 μM)
10x T4 DNA Ligase buffer	2
T4 DNA Ligase	1
DNase/RNase Free H ₂ O	11
Total	20

It is recommended also setting up a no-insert, pSpCas9(B.B)-2A-GFP negative control for ligation. Let the reaction to take place overnight by incubating in a heat block or thermocycler at 16 °C.

Transformation

Prepare LB-Agar plates using the following amounts: 20 g of LB-Agar and 500 ml of ddH₂O. Put everything in a 500 ml glass bottle and autoclave. After this step wait until

the LB-Agar reaches 30 to 40 °C and add 500 µl of ampicillin (stock concentration 100 mg/ml) to reach a final concentration of 100 µg/ml. Once ampicillin has been homogeneously mixed with LB-Agar, pour 20 ml of LB-Agar in each petri dish and allow the agar to solidify for 30 minutes. Petri dishes can be stored upside down with the lid facing down at +4 °C.

12.5 g of LB-medium are added to 500 ml of ddH₂O and autoclaved, in this way LB-medium is obtained. Add 500 µl of ampicillin. Preheat agar plates and SOC media at least 30 min before using them in bacterial incubator at 37 °C. Competent DH5α bacteria are thawed on ice and added to 20 µl of the ligation mixture. Next, the mixture is left for 45 min on ice, followed by a heat-shock it for 45 sec at 42 °C and then back on ice for 2 min. Pipe 250 µl SOC media and agitate (at an angle of 45°) for 1 h at 37 °C at 220 rpm shaker. Spin down at 5,000 rpm for 5 min. Discard the supernatant and redisperse pellet with 100 µL of SOC medium. Plate 100 µl on an ampicillin plate and incubate at 37 °C overnight. Use glass beads to homogeneously distribute the bacteria in the plate. The day after pick two colonies using a sterile pipette tip and add it to 3 ml LB media (with ampicillin already inside) and shake it at 37 °C for 4 - 8 h. Add 5 ml LB media in a new 50 ml falcon tube, now transfer the 3 ml LB media to the fresh medium and shake it at 220 rpm shaker at 37 °C overnight.

Plasmid extraction

Extract plasmid DNA from bacterial cultures using the QIAprep Spin Miniprep Kit, following the manufacturer's protocol.

Sequencing of the plasmid

Confirm each colony's sequence by performing Sanger sequencing from the U6 promoter using the U6-specific primer.

U6 Fw primer	5' GAGGGCCTATTTCCTGATTCC 3'
--------------	-----------------------------

Send to GENEWIZ from Azenta Life Sciences for sequencing following the guidelines described in Methods 2.2.23 Sanger sequencing. Plasmid maps for all three vectors can be found in Supplementary Fig. 21.

2.2.17 Proliferation assay

In a 24-well plate 1x10⁵ cells are seeded in 1,000 µl/well. Cells are incubated for 24 h, next treatment with desired compound and vehicle is applied. By employing the Click-iT EdU cell proliferation kit and following the manufacturer's instructions, short-term growth is detected. Cells are counterstained using Hoechst 33342 (1:1,000 dilution to a final concentration of 0.01 mg/ml). Capture images using EVOS M7000 imaging system.

2.2.18 Real Time Polymerase Chain Reaction

In order to amplify a candidate exon or part of a plasmid the following mixture is made and incubated in a Mastercycler: 50 ng DNA, 1 μ M of forward and reverse primer, 0.4 μ l 10 mM dNTPs, 2 μ l 5x Flexi buffer, 13.2 μ l ddH₂O, 1.2 μ l of MgCl₂ (25 mM), 0.2 μ l of Maxima HS Taq polymerase. The following instructions are considered for the incubation; hot start for 4 min at a temperature of 94 °C, followed by denaturation for 40 sec at 94 °C, annealing for 40 sec at 54 °C, extension for 25 sec at 72 °C, a final extension for 10 min at 72 °C, and last samples can be hold at 14 °C.

The annealing temperature is determined by the length and composition of the primers and is typically set about 2 - 5 °C below their melting temperature. The following table contains the primers used within this project:

Gene	Use	FWD: 5' ->3'	RV: 5' ->3'
NFE2L2	Find mutations in exon 2 in DNA (use LiM13 tag for seq.)	GTAAAACGACGGCCAGTACCATCA-ACAGTGGCATAATGTG	GGCAAAGCTGGAAC-CAAATCCAG
NFE2L2	Use this primer pairs only on cDNA. PCR product (485 bp) contains exon 2 and 3	CACGGTCCACAGCTCATCAT	AAGACTGGGCTCTCGA TGTG
KEAP1	KEAP1 clones_seq. (381 bp) in DNA	GCTACCTGGAGGCTTACAACC	TACCCGGATCTCA-GTGTCTTG
NFE2L2	Use this primer pair to sequence NFE2L2 clones and proof the 10kb deletion (including exon 2). PCR product 313 bp (at DNA level)	GTAGACCCTTAGTAGTTTGA	GGTTCAGATCT-TAGCTCCTC
U6	Validation of gRNA inserted in plasmid	GAGGGCCTATTTCCCATGATTCC	
LiM13 tag	Tag used for sequencing NFE2L2 exon 2	GTAAAACGACGGCCAGT	

2.2.19 Reporter assay

1x10⁵ cells in 400 μ l in 24-well plates are transfected with 200 ng of pNQO1-ARE-Luc and 10 ng of pRL-CMV plasmid (for 303 5 ng, due to high transfection efficiency). As transfection reagent either FuGENE or PEI is used depending on the cell line, see table

below. 48 h post transfection, reporter gene activity is assessed using the Dual-Glo Luciferase Reporter Assay System following the guidelines from the supplier. Luminescence is measured using the FLUOstar Omega machine and analysis is performed using the Omega software version 5.11 R3.

Cell line or PDX	Add serum free media to a final volume of (μl):	Transfection reagent	Ratio: DNA (μg) : Transfection reagent (μl)	Final amount added of: DNA (μg) and Transfection reagent (μl)
HepT1	80	FuGENE	1:3	0.210 + 0,63
HuH6	12	PEI	1:5	0.210 + 1,05
HuH7	80	FuGENE	1:4	0.210 + 0,84
Hep3B	40	FuGENE	1:4	0.210 + 0,84
HepG2	40	FuGENE	1:3	0.210 + 0,63
214	12	PEI	1:3	0.210 + 0,63
303	20	FuGENE	1:3	0.205 + 0,62

2.2.20 RNA extraction

Remove growth medium from cells of a 6-well plate and wash them with PBS to remove any floating dead cells. Then 0.5 ml of TRI Reagent is added to the plate and incubated shortly. The lysate is transferred in a 2 ml tube (at this step the lysate can be frozen if needed). Incubate the lysate at RT for 5 min, then add 200 μl of chloroform and mix for 15 sec and let the tubes for 3 min at RT. After this step centrifuge at 4 °C for 15 min at 12000 rpm, a separation phase will form. The upper phase contains the RNA, therefore is transferred in a new 2 ml tube. Now we need to precipitate the RNA, so to the volume of supernatant we add the same volume of isopropanol and mix. Tubes are incubated for 10 min at RT and then centrifuged at 4 °C for 15 min at 12000 rpm. Now add 1500 μl of pre-chilled 70% ethanol and mix thoroughly. Centrifuge again at 4 °C for 5 min at 7500 rpm. Discharge supernatant, the RNA pellet (white color) should remain at the bottom, air dry the pellet until it becomes clear. Dissolve RNA in 25 - 50 μl of DNase/RNase Free H₂O based on the size of RNA pellet. To ensure that the isolated RNA has a good quality, we can measure the RNA integrity number (RIN) using a bioanalyzer 2100. The RIN value can go from 1 to 10 and a value between 7 - 10 is accepted as a good quality. To measure the RIN value, we relied on the 2100 Bioanalyzer and used the Agilent RNA 6000 Nano Kit following the manufacturer's protocol.

2.2.21 RNA Sequencing

Library preparation is carried out using 2 μg of total RNA with the TruSeq Stranded mRNA kit, and sequencing is subsequently conducted on a HiSeq2500 system (100 bp paired-end reads) at the Munich Genome Analysis Competence Center. The STAR aligner (v2.4.2a) is used to align reads to known genes from the HG19 (GRCh37) human

genome assembly and UCSC database, applying modified parameters (--two-pass-Mode=Basic). HTSeq-count (v0.6.0) quantified gene read counts, while DESeq2 (Bioconductor) normalized the data for differential gene expression analysis between clones and parental cell lines, as well as between hepatoblastoma patients with or without NFE2L2 mutations.

2.2.22 Real Time Quantitative Polymerase Chain Reaction

To measure the mRNA levels of a target gene in a sample we performed real time PCR. The following mixture is prepared: 1 µl of forward and reverse primer at a concentration of 1 µM, 2 µl of cDNA (40 ng), 6 µl of DNase/RNase Free H₂O and 10 µl of SYBR Green Supermix. Then the sample is incubated in a Mastercycler realplex² epgradient S and using the software Realplex 2.2 the following program is created; an initial denaturation for 2 min at a temperature of 95 °C, followed by denaturation for 15 sec at 95 °C, annealing for 15 sec at 58 °C, and lastly extension 20 sec at 68 °C,

Gene	Meaning	FWD: 5' ->3'	RV: 5' ->3'
AKR1B10	Aldo-keto reductase family 1 member B10	GCATTGTTGA-GAACATTCAGGTCT	CGTTACAGGCCCTCCAGTTT
NFE2L2	Nuclear factor erythroid 2-related factor 2	CGGTATGCAACAGGACATTGAG	GGCTTCTGGACTTGAACCAT
KEAP1	Kelch-like ECH-associated protein 1	ATTGGCTGTGTGGAGTTGCA	TGGCAGTGGGACAGGTTGA
TBP	TATA box binding protein (house keeping gene)	GCCCGAAACGCCGAATAT	CCGTGGTTCGTGGCTCTCT

2.2.23 Sanger sequencing

PCR-amplified exons are analysed on a 1 % agarose gel by gel electrophoresis. The PCR product is then cleaned using ExoSap-IT following the manufacturer's protocol. For DNA sequencing we relied on the GENEWIZ from Azenta facility and followed their guidelines for the amount of DNA and primer, see table below:

Template				Primer		Template + Your Primer
DNA Type	Submitted in	Concentration	Volume	Concentration	Volume	Pre-Mixed Total Volume

Plasmids purified	1.5 ml reaction tube	30-100 ng / μ l	5 μ l	5 pmol/ μ l (μ M)	5 μ l	10 μ l
PCR fragments purified		10-50 ng / μ l				

Chromas v1.45 software is used to analyse sequences of amplified exons.

2.2.24 Spectrophotometer – ND 1000 NanoDrop

The concentrations of DNA or RNA samples are determined with ND 1000 NanoDrop machine. Firstly, the machine is calibrated using the solvent used to dissolve the nucleic acids, which is DNase/RNase Free H₂O. Then 1 or 2 μ l of the sample is added to the NanoDrop machine and the concentration is measured in ng/ μ l. To assess the purity of DNA or RNA samples the ratio of absorbance at 260 nm and 280 nm is considered. Generally, a ratio of \sim 1.8 is desired for pure DNA and a ratio of \sim 2.0 for pure RNA.

2.2.25 Stable Transfection

Seed the following amounts of cells in 24-well plates using normal culture media supplemented with FBS, antibiotics and L-Glutamine (and ROCK for PDXs): 303, 1.5×10^5 ; 214, 1×10^5 ; HepT1, 1×10^5 ; HepG2, 2×10^5 ; HuH7, 1×10^5 ; Hep3B, 1×10^5 ; HuH6, 0.8×10^5 . After seeding let grow for 24 h. The day after rinse the cells with PBS and add 400 μ l of 2% FBS media (with no antibiotics or L-Glutamine). Transfect each cell line with plasmid + FuGENE or polyethylenimine (PEI). In the table below are all optimal transfection conditions for each cell line and PDX:

Cell line or PDX	Transfection reagent	Ratio of: DNA (μ g) : Transfection reagent (μ l)	Final amount added of: DNA (μ g) and Transfection reagent (μ l)	Add serum free media to a final volume of (μ l):
HepT1	FuGENE	1:3	1.6 + 4.8	80
HuH6	PEI	1:5	0.24 + 1.2	12
HuH7	FuGENE	1:4	1.6 + 6.4	80
Hep3B	FuGENE	1:4	0.8 + 3.2	40
HepG2	FuGENE	1:3	0.8 + 2.4	40
214	PEI	1:3	0.24 + 0.72	12
303	FuGENE	1:3	0.4 + 1.2	20

The FuGENE/DNA mixture in serum free media is incubated at RT for max 15 min, whereas for the PEI-containing mixture for max 20 min. Next add the transfection mixture to the cells dropwise. The day after, refresh cells by taking out 250 μ l of media and adding fresh 250 μ l of normal culture media (+ FBS and antibiotic and L-Glutamine where necessary).

2.2.26 Statistical analysis

Data are presented as mean \pm standard deviation (SD) or as the mean \pm standard error of the mean (SEM). The data underwent statistical analysis by comparing differences between two groups with Student's t-test. We used the software GraphPad Prism version 8.2.1. p-values that are less than 0.05 are considered statistically significant.

2.2.27 Western blot

Cells from a T25 flask are rinsed with 5 ml of PBS, next 2 ml of PBS is added. Cells are then scraped from the base of the flask and placed to a 15 ml falcon tube. Cells are spinned for 5 min at 1500 rpm, supernatant is discarded, and pellet is resuspended with 1 ml of PBS and placed in a 1.5 ml tube. A second centrifugation is performed for 5 min at 8,000 rpm and thereafter supernatant is discarded. After this step cell pellets can be stored at -20 °C. Keep cell pellets on ice during the next steps. Add 20 - 100 μ l of cell lysis buffer (CLB) based on pellet size. Resuspend gently the pellet in CLB and incubate for 20 min, centrifuge at 13,300 rpm in 4 °C. Supernatant contains the proteins, therefore is collected into a new 1.5 ml Eppendorf tube and kept on ice. After this step proteins can be stored at -80 °C.

To assess protein concentrations Bradford assay is employed. Therefore, we first need the following Bradford standards: 0, 100, 200, 400, 600, 800, 1000 and 1200 μ g BSA/ml lysis buffer. In a 96 well plate add in one row 10 μ l of each Bradford standard, in a second row add 1 μ l of protein suspension of interest (in duplicates). After this step apply 200 μ l of 1x Bradford dye. Maintain for 10 minutes in the dark and then measure the absorbance at 595 nm. Concentration of proteins can be calculated based on coefficient of determination or R squared for the regression evaluation of the standard series (R² should not be smaller than 0.960).

For protein denaturation, 10 μ g of protein solution is prepared in a 1.5 ml tube and adjusted to 26 μ l with water. Then add 10 μ l of LDS 4x and 4 μ l of sample buffer 10x. Mix everything and plate tubes in a heating block for 10 min at 70 °C. Afterwards place tubes on ice to prevent renaturation. Once proteins are denaturated, they can be maintained at 4 °C for a week, but for long-term storage at -20 °C.

Afterwards is performed a running of the proteins in SDS gel. Place the holder into the Western blot tank (XCell SureLock Blot Module). If only 1 gel will be run, a dummy gel is placed to fill the second empty holder. Fill the tank with 1x MES buffer. Take the

precast gel from Invitrogen (Novex™ WedgeWell™ 4 - 20%), remove comb and isolation tape from the gel and place the gel in the tank holder and fix the handle for stabilization. Start loading the samples and the PAGERuler according to your loading map. After this step, fill the tank to the rim with 1x MES buffer and start with 80V for staggering gel, increase it to 100V and then to 120V for the separating gel. If the gel is run for more than 2.5 h, remember to place the tank on ice to prevent the gel to melt.

After run is completed, the gel is removed, placed in water and always kept wet as it's very fragile. The plastic chamber that holds the gel is opened with the help of a spatula and then the staggering part is cut out. Open a Trans-Blot Turbo Mini 0.2 μ m PVDF Transfer Pack and place bottom part into turbo blot chamber and use roller to discharge air bubbles. Place the gel gently over the membrane, remove air gaps again using a roller and then place the top stack to complete the transfer sandwich and use roller to stabilize the gel. Seal the cassette firmly without disturbing the sandwich and run it for 7 min at 25V using the Trans-Blot Turbo Transfer System (for proteins over 180 kDa run for 10 min).

Following transfer, remove the membrane and rinse it in water briefly. Incubate then the membrane in 5% milk and shake for 45 min at RT at 57 rpm. After blocking, wash membrane 6 times for 5 minutes with PBS-T, then place the membrane with primary antibody dilution of interest overnight at 4 °C on rolling system tube revolver.

Following primary antibody incubation, wash membrane 6 times for 5 min with PBS-T and then place the membrane in secondary antibody diluted (5% milk PBS-T) for 1 h at RT on a shaker plate at 57 rpm. Secondary antibody should be selected according to the origin of the primary antibody.

Imaging can be performed after this last step. Therefore, wash membrane 6 times for 5 minutes with PBS-T following secondary antibody incubation. Prepare a fresh ECL prime Western blotting detection reagent by combining solution A and B (1:1 ratio). Vortex the prepared solution and keep it protected from light. Apply active ECL mixture over the membrane and incubate in darkness for 3 - 5 minutes. After this step use the ChemiDoc RS+ machine to capture pictures of the membrane with exposure of 5 sec to 5 min depending on the protein.

Stripping step removes the primary and secondary antibodies from the membrane and allows to check the membrane for another protein of interest. To do that, rinse the membrane with PBS shortly and then immerse it into stripping buffer for 30 - 60 minutes on a shaker at RT. Then remove stripping buffer and rinse the membrane with water. Wash

again the membrane with PBS for 5 minutes. Now perform the re-blocking with milk and continue with primary and secondary antibody as described.

3. Results

3.1 Main mutations identified in a cohort of 189 hepatoblastoma patients

Considering a cohort of 189 HB patients analyzed by whole exome sequencing coming from 3 different studies, we can state that the most mutated gene is *CTNNB1*, which accounts for 88% of the mutations (**Fig. 3 A**) (14, 17, 25).

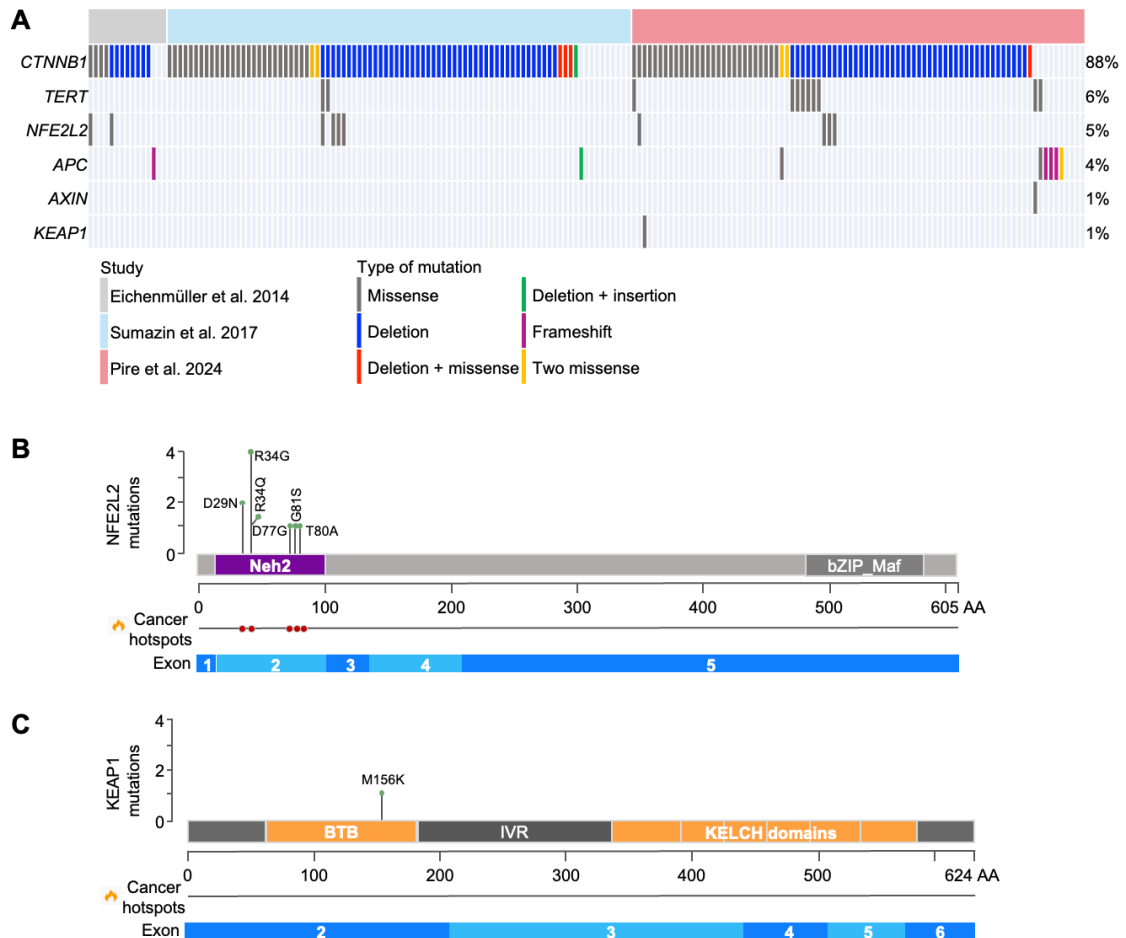


Figure 3 HB mutation landscape and domain mapping of *NFE2L2/KEAP1*. **A** Illustration of the mutational landscape of 189 HB patients from whole exome sequencing studies. Mutation types of the genes *CTNNB1*, *TERT*, *NFE2L2*, *APC*, *AXIN* and *KEAP1* are presented by a specific color code. **B** Linear structure of the *NFE2L2* protein (top) and cDNA (bottom), showcasing critical domains such as *Neh2*, where mutations frequently occur (cancer hotspots). **C** Linear structure of the *KEAP1* protein with critical domains such as *KELCH* domains, showing a mutation located within the functional domain *BTB* encoded by exon 2.

The second most mutated gene is *TERT* with a frequency of 6%, followed by 5% *NFE2L2*, 4% *APC*, 1% *AXIN* and 1% *KEAP1* mutations. This study focuses on *NFE2L2* and *KEAP1* mutations in HB, which are known to lead to constitutive activation of the NFE2L2 pathway, enabling tumor cells to resist oxidative stress, reprogram metabolism and evade chemotherapy (26, 90). Thus, in the present work we wanted to assess the functional role of these mutations starting with where they occur and what kind of mutations are they. Relying on the cBioPortal open-source platform (<https://www.cbioportal.org/>), we fed in the system all *NFE2L2* and *KEAP1* mutations coming from the cohort of 189 HB patients (fed information can be found in the supplementary Fig. 19). All identified *NFE2L2* and *KEAP1* mutations were displayed in a lollipop plot map (**Fig. 3 B and C**) together with the linear protein, if it's a hotspot cancer mutation and in which exon the mutation occurs.

In *NFE2L2* only heterozygous point mutations were identified occurring in exon 2 affecting the binding of the translated protein to KEAP1. Additionally, cBioPortal system identified all *NFE2L2* mutations as hotspot cancer mutations, meaning that they are recurrent mutations where the altered amino acid was detected as a frequently occurring hotspot within a dataset of tumors from different cancer types. In the *KEAP1* gene the mutation identified by Pire and colleagues occurred in the exon 2 that encodes for the BTB region important for the homodimerization of KEAP1 (25).

In summary, analysis of a cohort of 189 hepatoblastoma patients revealed that *CTNNB1* is the most frequently mutated gene, followed by *TERT* promoter, *NFE2L2*, *APC*, *AXIN* and *KEAP1*.

3.2 Clinical and transcriptomic insights into NFE2L2 mutated hepatoblastoma patients

In order to provide more information about disrupted NFE2L2-KEAP1 pathway in hepatoblastoma patients, we first performed RNA sequencing (**Fig. 4 A**) on three *NFE2L2* mutated patients previously reported in a study of our lab performed by Eichenmüller and colleagues (14). All three cases exhibited heterozygous *NFE2L2* mutations leading to amino acid changes in the protein (**Fig. 4 B**); in T253 an arginine (R) at position 34 mutated to glycine (G), in T577 a tyrosine (Y) at position 80 mutated to alanine (A), and in HepT1 a leucine (L) at position 30 mutated to proline (P).

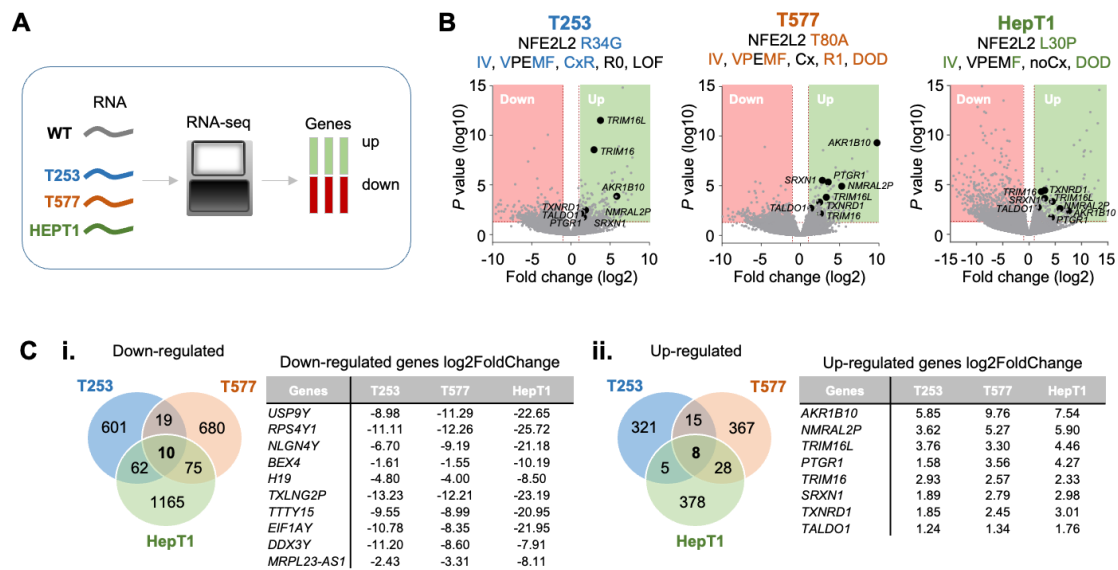


Figure 4 Transcriptomic analysis of NFE2L2-mutated HB patients. **A** Flowchart of RNA sequencing. RNA was extracted from several non-NFE2L2 mutated and 3 NFE2L2-mutated HB patients (T253, T577 and HepT1) and sent for next generation RNA sequencing (RNA-seq). Lists of up- and downregulated genes were calculated by comparing NFE2L2-mutated against non NFE2L2-mutated patients. **B** Volcano plots display RNA expression differences, with significance thresholds set at a P value of 0.05 and a log2 fold change of 1. Genes with transcriptional down-regulation are shown in the left quadrant (light pink), while transcriptionally up-regulated genes appear in the right quadrant (light green). Clinical information for each patient is provided above the corresponding volcano plot. Commonly upregulated genes are labeled by name. **C** Venn diagrams highlighting the overlap of downregulated and upregulated genes among the three patients with a $p < 0.05$ and a fold change > 2 . A total of 10 commonly downregulated genes (i.) and 8 commonly upregulated genes (ii.) were identified across the samples. Log2 fold changes of shared genes are detailed in the table next to each Venn diagram.

According to the PRETEXT classification system, all three cases were PRETEXT IV lacking contiguous tumor-free liver sections. Using the PRETEXT annotation factors (VPEFRM), patient T253 had involvement of the vena cava and all three hepatic veins (V), presence of distant extrahepatic metastases (M), and multifocal tumor involvement (F) (91). Additionally, T253 was chemotherapy resistant (CxR) and underwent complete resection resulting in R0 status (no residual tumor). Patient T577 had involvement of the vena cava and all three hepatic veins (V), involvement of the portal vein and its bifurcation (P), presence of distant extrahepatic metastases (M), and multifocal tumor involvement (F). In terms of treatment, T577 responded to chemotherapy (Cx) with microscopic

residual tumor (R1 status). Patient HepT1 had multifocal tumor involvement (F) and tumor was resected without prior chemotherapy (86). In terms of clinical outcomes T253 had loss of follow-up (LOF), T577 and HepT1 experienced death of disease (DOD).

In the first step RNA was extracted from several non *NFE2L2* mutated patients (wildtype) and from the three *NFE2L2* mutated patients and sent for next generation RNA sequencing (RNA-seq) (**Fig. 4 A**). Expression values of *NFE2L2*-mutated cases were then compared to non-mutated samples, ranked by log fold change and *P* value significance, organized as up- or down-regulated and plotted in a volcano plot (**Fig. 4 B**). Remarkably, 10 commonly down-regulated (*USP9Y*, *RPS4Y1*, *NLGN4Y*, *BEX4*, *H19*, *TXLNG2P*, *TTY15*, *EIF1AY*, *DDX3Y* and *MRPL23-AS1*) and 8 commonly up-regulated genes (*AKR1B10*, *NMRAL2P*, *TRIM16L*, *PTGR1*, *TRIM16*, *SRXN1*, *TXNRD1* and *TALDO1*) were identified across the three *NFE2L2*-mutated samples (**Fig. 4 C**).

Taken together, these findings indicate that *NFE2L2* mutations in HB are associated with aggressive tumor features and are characterized by a common transcriptional signature.

3.3 Characterization of cell lines and patient derived xenografts used within this study

Within this project we used 5 classic liver cancer cell lines (HepT1, HuH7, Hep3B, HuH6 and HepG2) and 2 PDXs (214 and 303). In **Fig.5 A** these cell lines and PDXs are detailed with their tumor type, tumor origin, sex, age and what mutations they carry.

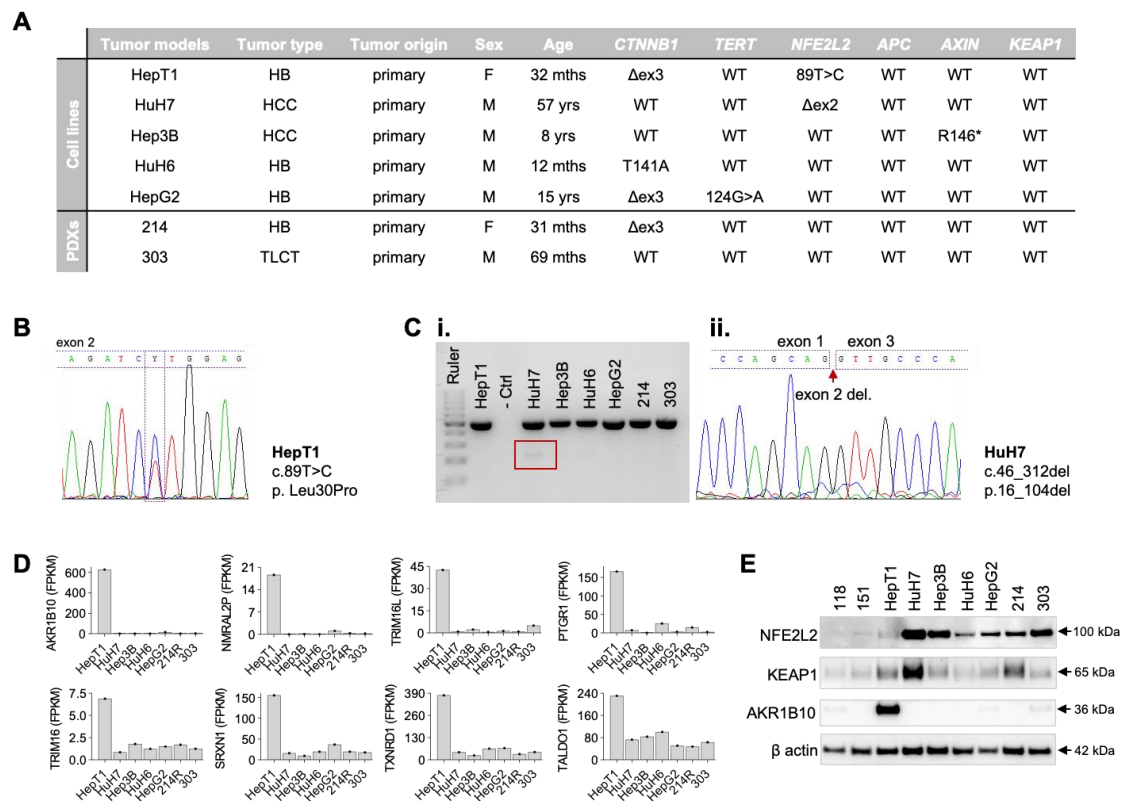


Figure 5 Characterisation of cell line and PDXs used within the study. **A** Table displaying information such as tumor models, tumor type, tumor origin, sex, age and mutations found in 5 classical liver tumor cell lines and 2 patient derived xenografts (PDXs). **B** Chromatogram displaying the heterozygous point mutation identified in the *NFE2L2* gene of HepT1 cell line by Sanger sequencing. **C i.** Investigation of exon 2 deletion at the cDNA level in *NFE2L2* gene in the cells. Primer pairs used were designed to amplify exon 2 and 3 and generate an amplicon of 485 bp. HuH7 cells showed an additional band around 218 bp, which denotes that there is a deletion. **ii.** Sanger sequencing of the excised band revealed that exon 2 in *NFE2L2* gene is deleted in HuH7 cells. **D** Bar graphs showing endogenous gene expression levels of 8 *NFE2L2* target genes in fragments per kilobase of transcript per million mapped reads (FPKM) in the cells. **E** Western blot analysis illustrating the following proteins: *NFE2L2* at 100 kDa, *KEAP1* at 65 kDa, *AKR1B10* at 36 kDa, and as a loading control β actin at 42 kDa.

As already previously mentioned, HepT1 harbors a heterozygous point mutation inside exon 2 of the *NFE2L2* gene (**Fig. 5 B**). As in HCC exon 2 skipping inside *NFE2L2* gene has been reported to occur, we wanted to check if the cohort of cell line and PDXs used within this study also have this kind of mutation (24, 77). Therefore, RNA was extracted from all cell lines, converted into cDNA, and an amplicon of 485 bp containing exon 2

and 3 was amplified. Strikingly, HuH7 showed a shorter band in the gel, which turned out to be an alternative transcript with an exon 2 skipping proved by subsequent Sanger sequencing (**Fig. 5 C**). Of note HuH7 cell line has been reported to have a hyperdiploid karyotype with altered chromosomal structures linked to chromosomal instability (92). Additionally, NFE2L2 gene resides on chromosome 2 which has 3 copies according to Carloni and colleagues (92).

As already discussed in the previous chapter, patients carrying *NFE2L2* mutations had 8 commonly up-regulated genes including *AKR1B10*, *NMRAL2P*, *TRIM16L*, *PTGRI*, *TRIM16*, *SRXN1*, *TXNRD1* and *TALDO1*. Therefore, we wanted to check the mRNA levels of these genes in the PDXs and cell lines used within this study. Notably, HepT1 was the only cell line with high expression levels of these 8 genes (**Fig. 5 D**). Regarding HuH7, even though we found an exon 2 skipping, we did not observe high expression levels of the 8 mentioned genes. Therefore, we presume that this is an alternative splicing that produce mRNA transcripts that are not translated into proteins lacking the Neh2 domain encoded by exon 2 (see Western blot in **Fig. 5 E** where no mutated protein is expressed). By comparing the degree of target gene activation, we identified AKR1B10 as the most pronounced activated target compared to the other 7 genes in *NFE2L2*-mutated HepT1 cells (**Fig. 5 D**). To get a better understanding how AKR1B10 is expressed between cancer cells and normal liver cells we performed a Western blot analysis (**Fig. 5 E**). Strikingly, AKR1B10 was highly abundant in HepT1. A subtle expression was observed in one normal liver sample (118), in the HepG2 cell line, and in the PDX 303. As our focus in this study was the role of NFE2L2 and KEAP1 in pediatric liver cancer, we also checked the protein levels of these two. High protein expression levels of NFE2L2 were observed in cancer cells compared to normal liver. Between all cancer cells, HepT1 and HuH6 were the two cell lines expressing slightly lower protein levels of NFE2L2, whereas HuH7 had the highest expression. Of note, it is important to mention that there are misconceptions related to NFE2L2 molecular weight, isoforms, antibody specificity, and functional regulation. The study by Kopacz and colleagues elucidated this and identified the correct molecular weight of NFE2L2 at 95 -110 kDa (93). This abnormal migration of NFE2L2 protein is caused by the presence of by high content of negatively charged amino acids (93). KEAP1 protein levels were also investigated, which revealed a similar trend, that cancer cells generally express higher levels when compared to normal liver cells.

In summary, within this project we used five classic cell lines (HepT1, HuH7, Hep3B, HuH6, HepG2) and two PDXs (214 and 303). Given prior reports of exon-skipping mutations in the *NFE2L2* gene in HCC, we identified an exon-skipping mutation in *NFE2L2* in HuH7 cells, yet this did not result in truncated protein expression, nor activation of target gene expression. Moreover, the *NFE2L2*-mutated HepT1 cell line showed notably high expression of AKR1B10 at both mRNA and protein levels. Protein analysis further indicated elevated *NFE2L2* and *KEAP1* levels in cancer cell lines against normal liver tissue, with HuH7 showing the highest *NFE2L2* and *KEAP1* levels.

3.4 CRISPR-Cas9 engineering of *NFE2L2* and *KEAP1* clones

Since *NFE2L2* mutations are rare, limiting the availability of patient-derived cell models for drug testing, we developed several liver cancer cell models that mimic patient-specific *NFE2L2* or *KEAP1* mutations.

First, we tried to generate heterozygous point mutations as those observed in the sequenced patients. However, this would have needed a protospacer adjacent motif (PAM) near the region where these point mutations usually occur and additionally a gRNA with as few as possible mismatches (off target sites). In fact, once we pasted the whole exon 2 into the ChopChopTool, only one gRNA had 0 mismatches (see Supplementary Figures Fig. 20). However, this gRNA is located right in between the DLG and ETGE motifs that we wanted to mutate, therefore too far away from the exact location where the point mutations usually occur. Another option could have been to use the Homology-Directed Repair (HDR) system, where a repair template is provided in addition to the designed plasmid that contains the gRNA. However, efficient delivery of both the plasmid and the repair template is difficult to achieve. Therefore, we opted for a faster and more efficient way, which was to completely eliminate the exon 2 of the *NFE2L2* gene. Small deletions inside exon 2 have been already reported in HCC and this kind of mutations also drive the *NFE2L2* gain-of-function as the DLG and ETGE motifs are eliminated (24, 77).

We established several mutants following the protocol described by Ran and colleagues (88). **Fig. 6 A** displays a flow chart showing all necessary steps to obtain clones using the CRISPR-Cas9 editing system.

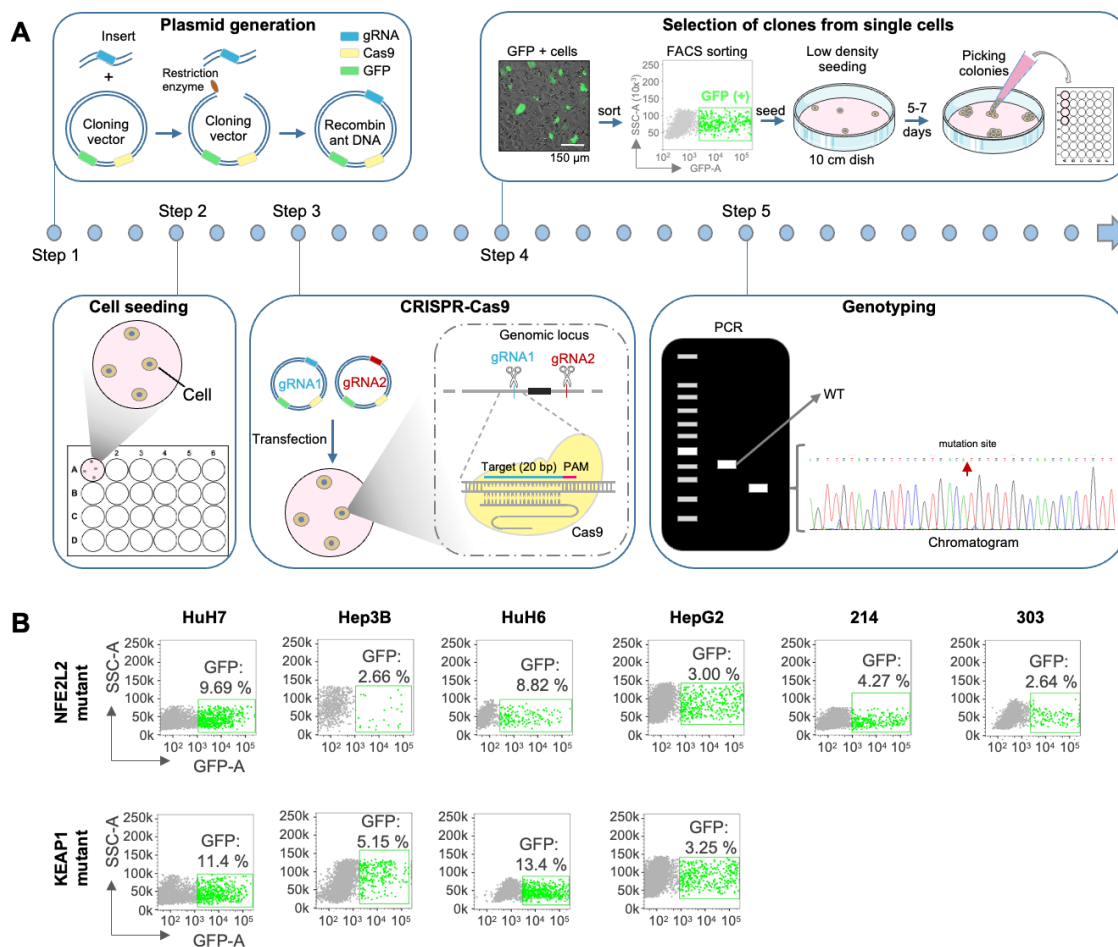


Figure 6 Flow chart of CRISPR-Cas9 editing system. **A** Step 1 involves plasmid generation where the insert, containing the designed gRNA, is inserted into the backbone of the cloning vector containing the sequence to express Cas9 and green fluorescent protein (GFP). Step 2 is cell seeding and step 3 cell transfection with designated plasmids. Step 4 displays sorting of GFP positive cells and growing single cell colonies. Step 5 shows genotyping using PCR amplification, Sanger sequencing, and analysis of the chromatogram. **B** Scatter plots of all sorted NFE2L2 and KEAP1 mutants derived from 5 classical cells lines (HuH7, Hep3B, HuH6 and HepG2) and 2 PDXs (214 and 303). On the x axis is show the fluorescence intensity and on y axis the side scatter (SSC). Additionally, the percentage of sorted cells is shown inside each scatter plot.

In step 1, specific gRNAs targeting *NFE2L2* or *KEAP1* were designed, ensuring minimal off-target sites. For *NFE2L2*, two gRNAs were designed to target the introns flanking exon 2 in order to delete the Neh2 domain. For *KEAP1*, one gRNA targeting exon 3 (previously described in a study by Zheng and colleagues) was designed in order to insert frameshift mutation and generate a premature stop codon to disrupt the KELCH domains

(89). The gRNAs were cloned into the pSpCas9(B.B)-2A-GFP vector, which also expresses GFP and Cas9. In step 2 four classic cell lines (HuH6, HuH7, Hep3B, HepG2) and two PDX models (214, 303) were seeded for transfection. In step 3 CRISPR-Cas9 system performs its function disrupting the selected genes. In step 4, post-transfection GFP-positive cells were sorted. Step 5 highlights the sequence verification of the mutated sites. **Fig. 6 B** illustrates scatter plots showing the percentage of finally sorted GFP-positive cells. For HuH7 and HuH6 cell lines an average transfection efficiency of 10.5 - 11% was reached, followed by 214 with 4.3%, Hep3B with an average of 3.9% and 303 with 2.6%.

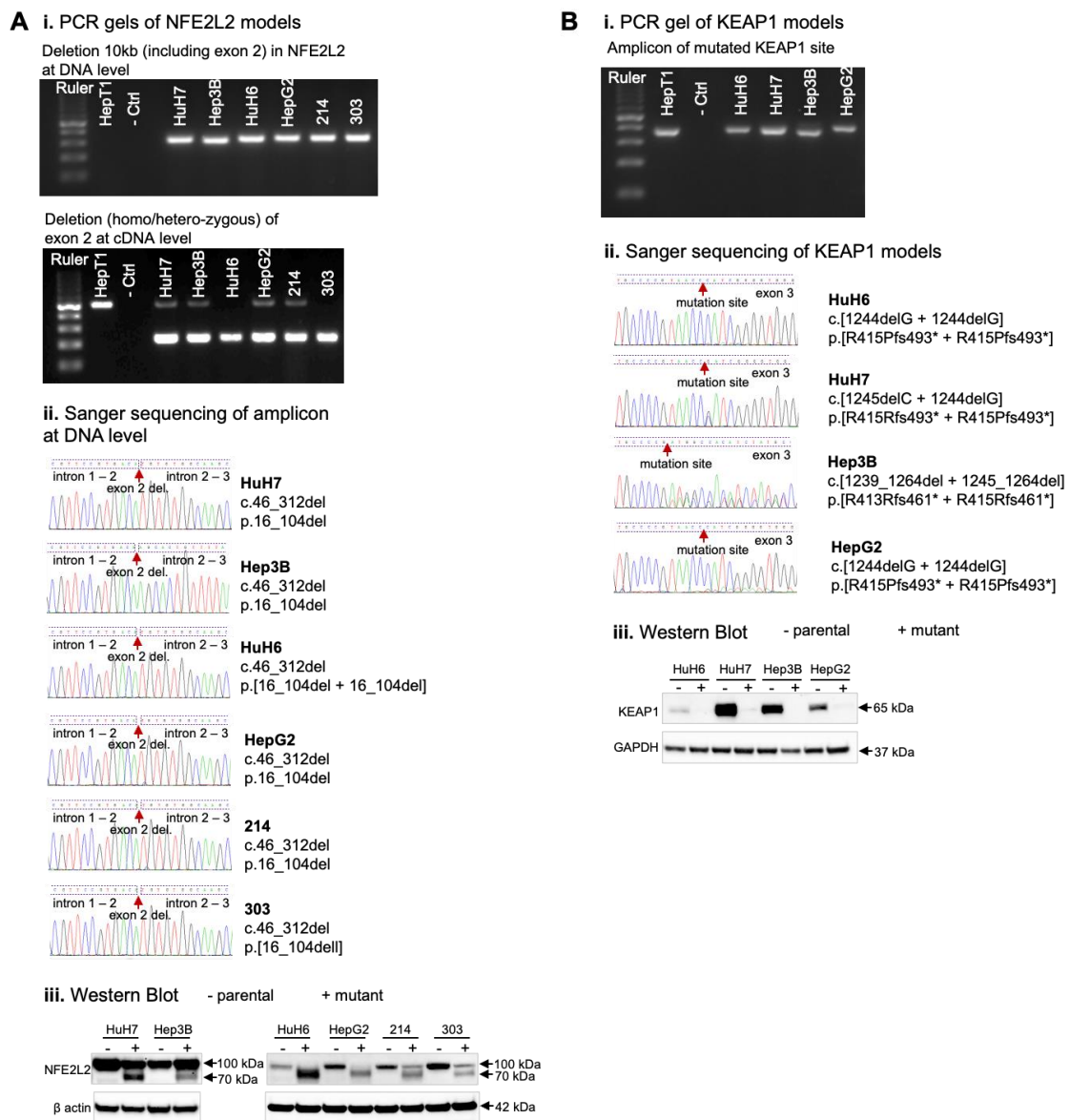


Figure 7 Characterisation of NFE2L2 and KEAP1 models. **A i.** PCR gels of established NFE2L2 mutants, the top one confirms the deletion of ~10 kb (containing the exon 2) at the DNA level in the NFE2L2 gene. DNA extracted from HepT1 cell line was used as a positive control where no band is formed, as the Taq polymerase can't generate such a

*big amplicon. As a negative control we used the PCR mixture without DNA. 4 classic cell lines and 2 PDX have a band of 313 bp indicative of a 10 kb deletion. At the cDNA level, the band at 485 bp denotes exon 2 + exon 3 and the band at 218 bp denotes only the exon 3 (exon 2 was deleted). cDNA extracted from HepT1 was used as a positive control for a full-length amplicon. ii. Chromatograms of PCR amplicons sequenced at DNA level of NFE2L2 mutants. The red arrow denotes the mutated site. For each mutant the mutation at the cDNA and protein level is written. iii. Western blot analysis of all NFE2L2 mutants, the upper band at 100 kDa showing the NFE2L2 protein expressed by the wildtype (WT) allele and the lower band at 70 kDa showing the altered protein expressed by the mutated allele. As a loading control β actin was used. **B i.** PCR gel of KEAP1 mutants, with an amplicon generated at the DNA level near the mutation site. ii. Chromatograms of KEAP1 mutants are shown together with the mutation at the cDNA and protein level. The red arrow denotes the mutation site. iii. Western blotting analysis showing the KEAP1 protein at 70 kDa for the WT and no band for the mutants as the epitope of the antibody resides on the deleted region. GAPDH was used as a loading control.*

As shown in **Fig. 7 A**, we successfully generated six NFE2L2 clones. Of these, HuH7, Hep3B, HepG2 and 214 exhibited a heterozygous deletion of exon 2 at the cDNA level, while HuH6 and 303 displayed a homozygous deletion of exon 2. All observed deletions in the NFE2L2 models occur at the position 46 - 312 of the cDNA, either homo- or heterozygously. As seen in the **Fig. 7 A iii.** the mutants compared to the WT cells display two bands, one at 100 kDa showing the NFE2L2 protein and one band at 70 kDa showing the NFE2L2 protein with the deleted Neh2 domain. As it can be observed for HuH6 mutant we see only one band at 70 kDa due to the fact that both alleles are mutated. For 303 despite the cDNA analysis shows homozygous deletion of exon 2 in NFE2L2, the non-mutated allele is probably incompletely captured at the cDNA level due to alternative splicing or changes in transcriptional regulation, nevertheless allowing it to produce a NFE2L2 protein detected at 100 kDa, while the mutated allele produces a mutated NFE2L2 protein with a band observed at 70 kDa.

In addition to the NFE2L2 models, we established four KEAP1 knockout models derived from the four fast-growing classical cell lines: HuH6, HuH7, Hep3B and HepG2 (**Fig. 7 B**). These models were obtained by introducing frameshift mutations in exon 3 of both alleles, resulting in premature stop codons and the production of truncated KEAP1 proteins. As already mentioned above, we considered the study by Zheng and colleagues,

where they established mutated KEAP1 liver cancer cell lines by disrupting the exon 3 (89). From each classic cell line, we generated a KEAP1 model carrying a homozygous frameshift mutation within exon 3, disrupting the KELCH domains. In the HuH6 and HepG2 KEAP1 models, the same type of mutation was observed: a guanine deletion at position 1244 in both alleles, leading to a frameshift mutation (**Fig. 7 B**). For the HuH7 KEAP1 model, one allele harbored a guanine deletion at position 1244, while the other had a cytosine deletion at position 1245, both resulting in frameshift mutations. In the Hep3B KEAP1 model, one allele had a 25-base pair deletion starting at position 1239, while the other had a 19-base pair deletion starting at position 1245, both mutations not in frame and therefore resulting in a premature stop codon downstream.

In summary, several NFE2L2 and KEAP1 models were developed using the CRISPR-Cas9 editing system, effectively mimicking patient conditions and providing valuable tools for screening potential therapeutic inhibitors targeting the KEAP1-NFE2L2 pathway.

3.5 *NFE2L2* and *KEAP1* disruption enhances NFE2L2 activity and target gene expression

Mutations in either the *NFE2L2* or *KEAP1* genes have been shown to make NFE2L2 resistant to ubiquitination and subsequent degradation by the proteasome system (75, 84, 94). In order to assess for increased abundance of NFE2L2 protein in NFE2L2 mutants, we first stained the NFE2L2 protein in the HepT1 cell line that endogenously carries a NFE2L2 mutation. As seen in **Fig. 8 A i**, HepT1 cells exhibited high levels of NFE2L2 protein. With a 60X magnification (**Fig. 8 A ii**.) we observed that most of the cells had NFE2L2 protein present in the cytoplasm and in the nuclei, however some cells exhibited a more prominent localization in the nuclei rather than in the cytoplasm. Based on the fluorescence intensity, we quantified this difference and found that around 63% of the cells had cytoplasmatic and nuclear NFE2L2 localization, whereas around 30% of the cells had a more prominent nuclear localization rather than in the cytosol (**Fig. 8 A iii**.). Moreover, we found that NFE2L2 was absent from the nucleolus that is specialized for ribosome biogenesis (**Fig. 8 A ii**.) (95).

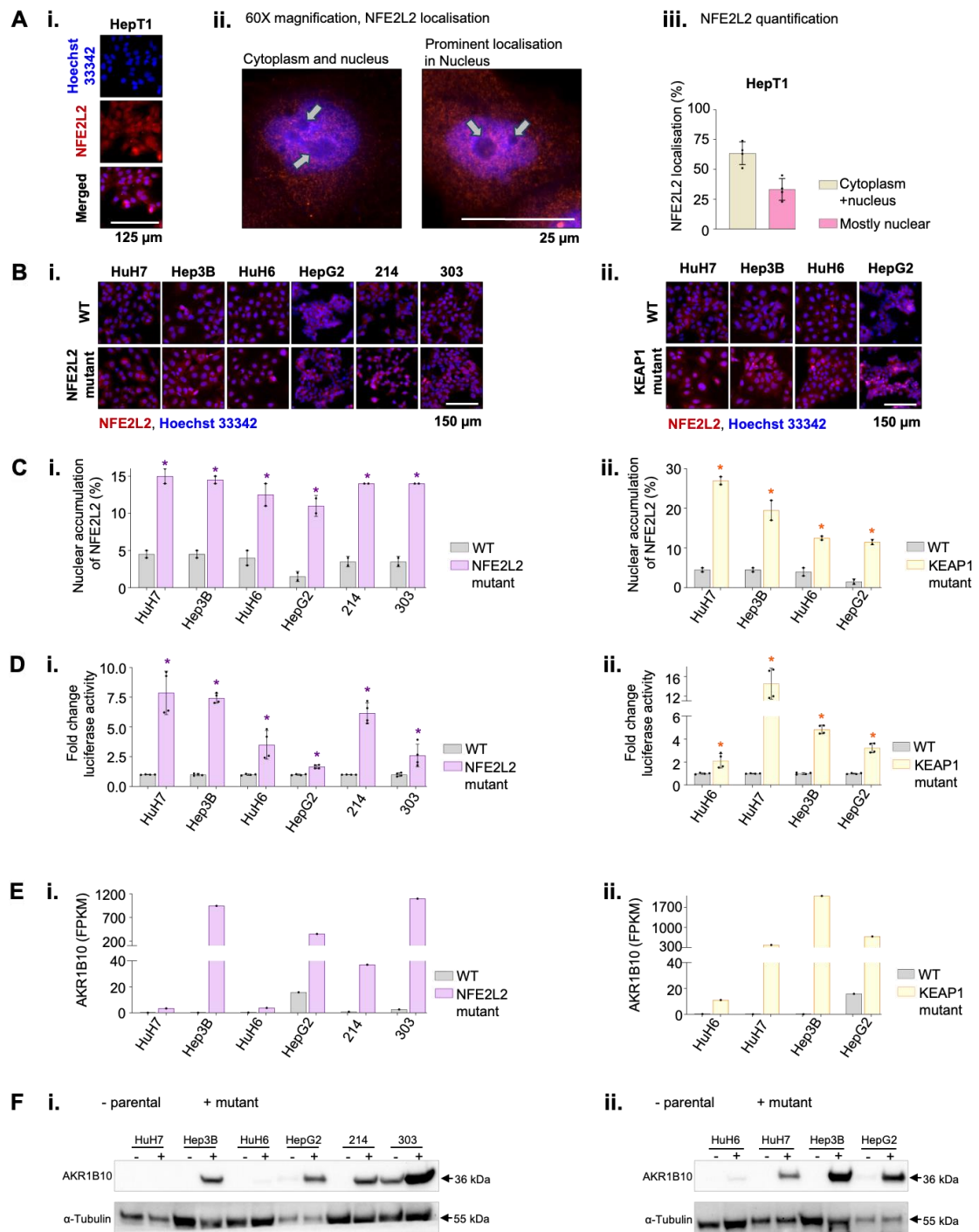


Figure 8 NFE2L2 localisation, activity and AKR1B10 expression in mutants. **A i.** Immunofluorescent staining of NFE2L2 protein (Alexa fluor 555, red) and nuclei (Hoechst 33342, blue) in HepT1 cells with a 10X magnification. **ii.** 60X magnification images showing NFE2L2 protein localization within HepT1 cells in the cytoplasm and nucleus (left image) or cytoplasm with higher fluorescence intensity in nuclei (right image). Arrows point at the nucleolus where no NFE2L2 accumulation occurs. **iii.** Quantification of NFE2L2 localization within the cytoplasm and nuclei. Bars represent mean \pm standard deviation (SD) of one experiment with quadruplicates. **B** Immunofluorescence images of

wildtype (WT) versus mutant cells, depicting NFE2L2 protein in red and the nuclei in blue. (i.) WT cells and respective NFE2L2 mutants and WT versus KEAP1 mutants (ii.). **C** Bar graphs showing the nuclear localization of NFE2L2 in percentage within WT and NFE2L2 mutants (i.) and WT versus KEAP1 mutants (ii.). The bars represent mean \pm standard deviation (SD) from a single experiment with duplicates. **D** ARE-driven luciferase activity was measured in WT versus NFE2L2 (i.) and WT versus KEAP1 (ii.) mutated cells, transiently transfected with the pNQO1-ARE-Luc and pRL-CMV vector for 48 h. Each bar represents the mean \pm standard deviation (SD) of two independent experiments with duplicates. Luciferase activity in WT cells was normalized to 1. Statistics were calculated using a two-tailed unpaired Student's *t* test with * $p < 0.05$. **E** mRNA levels of AKR1B10 retrieved from RNA sequencing in WT versus NFE2L2 displayed as bar graphs (i.) or WT versus KEAP1 (ii.) mutated cells. **F** Western blot analysis of AKR1B10 (at 36 kDa) showing WT versus NFE2L2 mutants (i.) and WT versus KEAP1 mutants (ii.). Alpha tubulin (at 55 kDa) was used as a loading control.

In the next step we wanted to investigate the NFE2L2 protein localization differences between WT and NFE2L2 or KEAP1 mutants. As seen in **Fig. 8 B**, NFE2L2 and KEAP1 mutants exhibited generally a slightly higher abundancy of NFE2L2 when compared to parental cells. For instance, there is a clear visual difference between 214 WT and NFE2L2 mutant, or between all WT cells and all KEAP1 mutants. Additionally, we observed that in the clones some cells had a higher fluorescence intensity in the nuclei rather in the cytoplasm, prompting a translocation of NFE2L2 in the nuclei to perform its activity. Therefore, we decided to quantify this localization difference (**Fig. 8 C**). Thus, we found that between WT and NFE2L2 clones, the clones had on average a 10% higher accumulation of NFE2L2 protein in the nuclei. Whereas in the KEAP1 this difference was even more prominent, for instance in HuH7 between WT and mutant cells there was about 20% difference with higher accumulation of NFE2L2 in the nuclei of the clones. To determine whether the increased abundance of NFE2L2 in these mutant cells activated the NFE2L2 pathway, we measured its transcriptional activity. Cells were transfected with a plasmid containing ARE sequences upstream of a luciferase reporter gene. As shown in **Fig. 8 D**, compared to WT cells all NFE2L2 and KEAP1 mutant cells exhibited significantly elevated ARE-driven luciferase activity, confirming enhanced NFE2L2 transcriptional activity.

To explore if NFE2L2 activation affected gene expression, we examined the expression levels of AKR1B10, the most reliable NFE2L2 target gene described in our RNA sequencing analysis of the three NFE2L2-mutated HB patients, in the NFE2L2 or KEAP1 models and compared it to parental cell lines (**Fig. 8 E**). Most of the NFE2L2 mutants displayed extremely high AKR1B10 mRNA levels when compared to parental cells, including Hep3B, HepG2, 214 and 303. However, only a slight increase was observed in the NFE2L2 HuH6 and HuH7 mutants. Concerning KEAP1 mutants, HuH6 mutant compared to parental models displayed only a slight increased expression of AKR1B10 gene, whereas the other mutants had significantly higher levels compared to their parental counterparts. Considering these results, we wanted to investigate the protein levels of AKR1B10 in the mutants and compare this to the parental cells. Western blot analysis was perfectly in line with the mRNA levels observed (**Fig. 8 F**). Regarding the NFE2L2 mutants, HuH7 and HuH6 models had very low AKR1B10 protein expression. Hep3B, HepG2, 214 and 303 mutants expressed high AKR1B10 proteins compared to their parental cells. A slightly high expression is observed in WT 303 due to the fact that we exposed the membrane for longer time trying to see if any AKR1B10 signal would be captured for HuH7 samples. Nevertheless, a slight endogenous level of AKR1B10 in 303 WT sample was expected as it can be seen in **Fig. 5 E**. All KEAP1 mutants expressed high protein levels of AKR1B10, from the lowest to the highest we have HuH6, HuH7, HepG2 and Hep3B.

In summary, we found that disrupting *NFE2L2* or *KEAP1* genes increased NFE2L2 protein levels, with a higher accumulation in the nuclei of mutant cells compared to parental cells. This nuclear localization correlates with enhanced transcriptional activity of the NFE2L2 pathway, as evidenced by elevated ARE-driven luciferase activity, followed by high mRNA and protein levels of the NFE2L2 target gene AKR1B10.

3.6 Morphology and growth analysis in WT versus NFE2L2 or KEAP1 models

To assess whether the disruption of *NFE2L2* or *KEAP1* affected cell morphology, we seeded all clonal cell lines and their parental counterparts in 6-well plates, allowing them to grow to approximately 80% confluence. Images were then captured using a digital phase-contrast microscope at 10X magnification (**Fig. 9 A**). No observable differences in morphology were found between parental and clonal cells after disruption of the *NFE2L2* or *KEAP1* genomes.

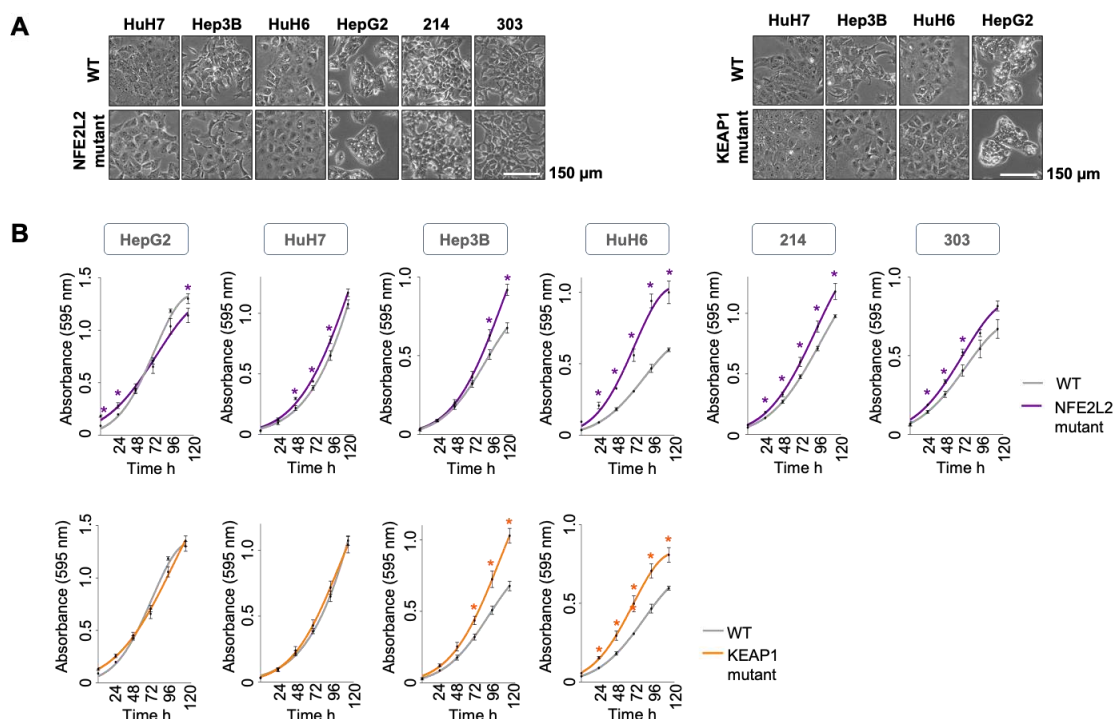


Figure 9 Morphology and growth in WT and mutant cells. **A** Cell morphology analysis of NFE2L2 or KEAP1 mutants illustrating no changes in cell morphology when compared to their parentals. **B** Growth curves of NFE2L2 and KEAP1 clones along with their respective parental cell lines were assessed over a 120 h period using an MTT viability assay performed every 24 h. Experiments were conducted three times with duplicates, and error bars indicate the mean \pm standard error of the mean (\pm SEM).

Hyperactivation of NFE2L2-ARE signaling pathway has been described to enhance cell survival and promotes uncontrolled growth (79, 84, 96). To evaluate this effect, the proliferation rate of parental and clonal cells was monitored over 120 h. Strikingly, most clones including Hep3B, HuH6, 214 and 303 in both NFE2L2 and KEAP1 models displayed significantly increased proliferation rates compared to WT cells (**Fig. 9 B**). HuH7 and HepG2 in both NFE2L2 and KEAP1 models did not show this phenotype.

In summary, the disruption of the *NFE2L2* and *KEAP1* genes did not affect cellular morphology. However, it significantly impacted cell growth, with most of the mutant cells proliferating faster than their parental counterparts.

3.7 *NFE2L2* and *KEAP1* mutations increase resistance towards cisplatin and doxorubicin

NFE2L2 activation is a well-established driver of chemotherapeutic resistance (26, 84, 96). Therefore, we evaluated the sensitivity of our NFE2L2 and KEAP1 mutant models

to cisplatin and doxorubicin during 72 h of treatment (**Fig. 10**). Globally, all NFE2L2 and KEAP1 mutants exhibited reduced sensitivity to 1 or 10 μ M of cisplatin when the drug response was compared to WT cells. A similar trend was observed when the cells were treated with 1 μ M of doxorubicin. However, HepG2 and HuH7 in both NFE2L2 and KEAP1 mutant cells retained normal sensitivity or even exhibiting enhanced sensitivity to both drugs. These results highlight that mutations in *NFE2L2* and *KEAP1* significantly impact cancer cell sensitivity to cisplatin and doxorubicin. Strikingly, HepG2 and HuH7 models failed consistently to show most of the phenotypes observed in the other clones including the resistance towards cisplatin and doxorubicin.

In summary, *NFE2L2* and *KEAP1* mutations result in reduced sensitivity to chemotherapeutic agents like cisplatin and doxorubicin in most of the models, emphasizing their role in drug resistance.

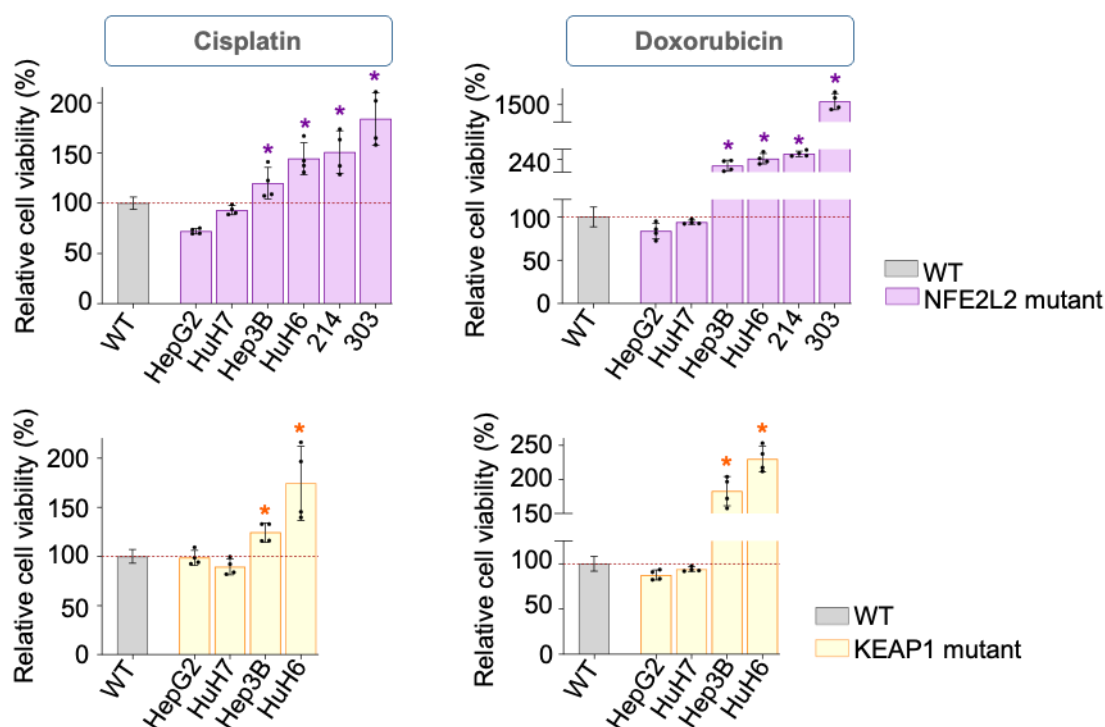


Figure 10 Drug response in the models towards cisplatin and doxorubicin. Bar graphs showing drug response of NFE2L2 and KEAP1 mutants along with WT cells, exposed to 10 μ M of cisplatin (except Hep3B NFE2L2 mutant exposed to 1 μ M) and 1 μ M of doxorubicin exposed for 72 h. Drug response of WT cells was normalized to 100%, error bars represent the mean \pm standard deviation (SD) of two independent experiment with duplicates. Statistics were calculated using a two-tailed unpaired Student's *t* test, with * $p < 0.05$.

3.8 Validation of NFE2L2 and KEAP1 mutant models using RNA sequencing and Gene Set Enrichment Analysis (GSEA)

To validate that our established models accurately mimic the transcriptomic patterns of previously described NFE2L2-mutated and sequenced patients (T253, T577 and HepT1), we extracted RNA from our NFE2L2 and KEAP1 mutants, as well as WT cells, and sent it for RNA-seq (**Fig. 11 A**).

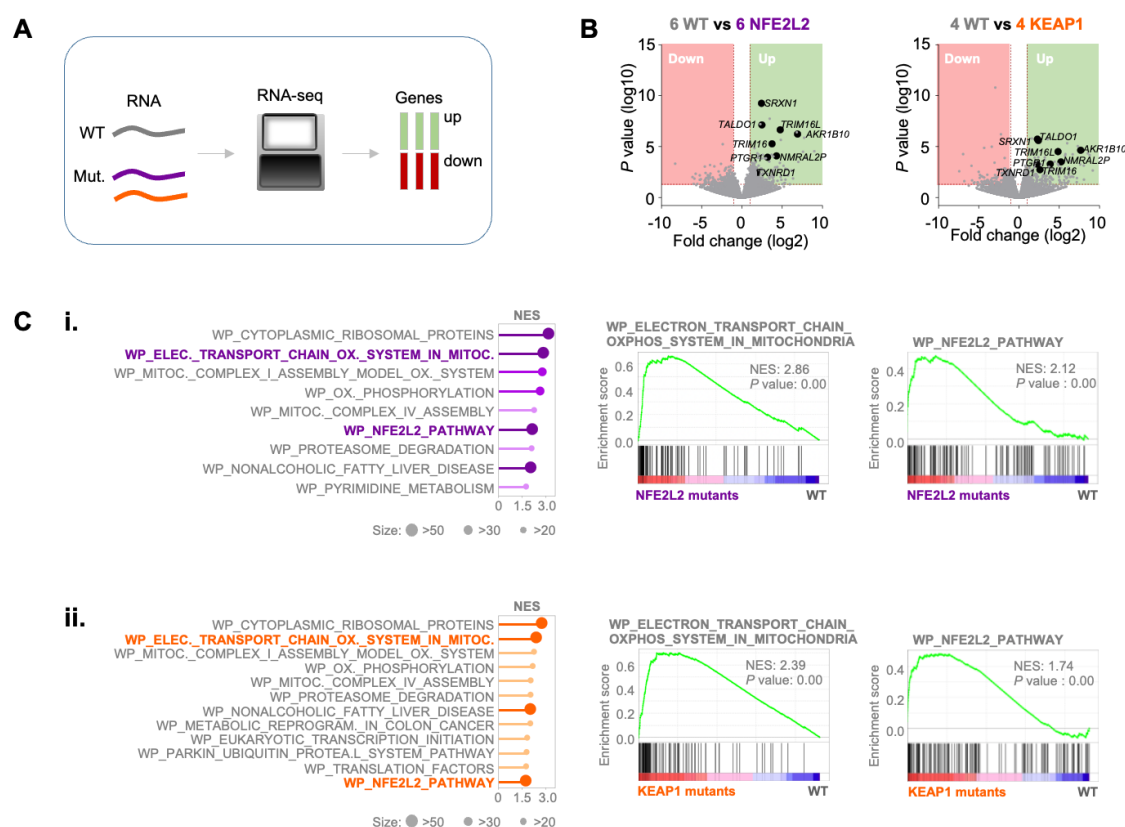


Figure 11 Transcriptomic profiling and GSEA of NFE2L2/KEAP1 mutants. **A** Flowchart illustrating RNA extraction from WT and mutant cells, followed by next generation RNA sequencing (RNA-seq), and generation of lists with up- and down-regulated genes of mutant versus WT cells. **B** Volcano plots displaying RNA expression differences, with significance thresholds set at a P value of 0.05 and a log2 fold change of 1. Genes with transcriptional down-regulation are shown in the left quadrant (light pink), while transcriptionally up-regulated genes appear in the right quadrant (light green), with 8 up-regulated genes highlighted by name (AKR1B10, NMRAL2P, TRIM16L, PTGR1, TRIM16, SRXN1, TXNRD1 and TALDO1). **C** Gene set enrichment analysis of RNA-seq data displaying positively enriched Wikipathways (WP) gene sets, given as normalized enrichment scores (NES) and number of genes involved in the respective gene sets (size). Upper part of the figure shows NFE2L2 mutants (i.) and the lower part KEAP1 mutants (ii.). Two important WP gene sets are highlighted and shown as individual enrichment

plots on the right side of the panel; electron transport chain oxidative phosphorylation system in mitochondria and NFE2L2 pathway.

The up- and down-regulated genes were compared to non-mutated cell lines and visualized using a volcano plot (**Fig. 11 B**). By applying significance thresholds of a P value ≤ 0.05 and a $\log_2\text{FoldChange} \geq 1$, we identified the same eight up-regulated genes previously described in patients: *AKR1B10*, *NMRAL2P*, *TRIM16L*, *PTGR1*, *TRIM16*, *SRXN1*, *TXNRD1*, and *TALDO1*. This confirmed that our models do indeed mimic the transcriptomic patterns observed in NFE2L2-mutated patients. While single-gene analyses provide valuable insights into specific genes with differential expression, they often lack the broader context of biological pathways. To get a broader vision, we employed gene set enrichment analysis (GSEA), which examines whether entire pathways or sets of related genes exhibit systematic differences in expression between two biological conditions (97). We performed GSEA on the RNA-seq data from NFE2L2 and KEAP1-mutant cells, which revealed several significant WikiPathways (**Fig. 11 C**, left panel). Among these, two gene sets stood out as particularly relevant triggered by NFE2L2 and KEAP1 mutation: the electron transport chain and oxidative phosphorylation system in mitochondria as well as the NFE2L2 pathway (**Fig. 11 C**, right panel).

These data demonstrate that the NFE2L2 and KEAP1-mutated models closely replicate key features of patient phenotypes, particularly in terms of individual gene expression. GSEA moreover identified significant enrichment of pathways related to the electron transport chain and oxidative phosphorylation system in mitochondria as well as the NFE2L2 pathway in the models.

3.9 *In silico* drug prediction identifies Na⁺/K⁺-ATPase inhibitors as a novel class of drugs against NFE2L2 activated pediatric liver cancers

In order to identify potential drug candidates to treat NFE2L2 activated HBs, we made use of the RNA-seq data derived from six NFE2L2 and four KEAP1 established models. Up regulated genes of NFE2L2 activated HBs were compared to non-mutated samples and organised by statistical significance, then the top 50 up-regulated genes were used as an input in a drug prediction tool ConnectivityMap (CMap) (**Fig. 12 A**).

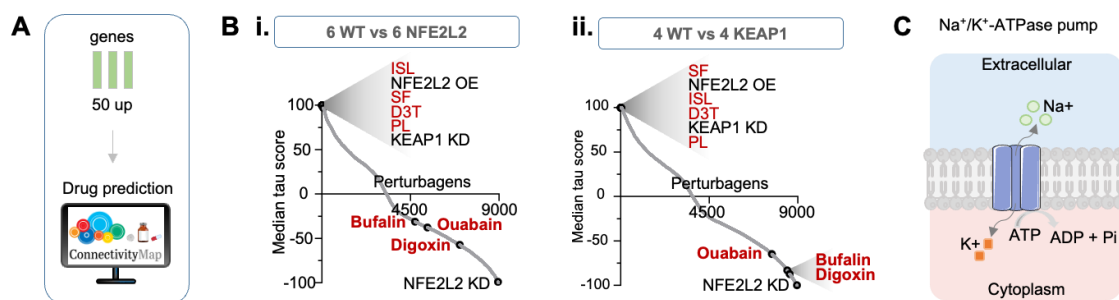


Figure 12 *In silico* drug prediction using NFE2L2/KEAP1 models. **A** Flow chart showing *in silico* drug prediction where top 50 up-regulated genes derived from NFE2L2-activated cells organised by significance of *P* value were fed into the drug prediction tool ConnectivityMap (CMap). **B** Drug prediction using 6 wildtypes (WT) versus 6 NFE2L2 mutants (**i.**) or 4 WT vs 4 KEAP1 mutants (**ii.**). CMap provides a list of perturbagens (*x* axis) organized by a median tau score (*y* axis). Perturbagens can be drugs (listed in red) or gene perturbations (listed in black) with overexpression (OE) or knockdown (KD). Isoliquiritigenin (ISL), parthenolide (PL), sulforaphane (SF), 1,2 dithiole 3 thione (D3T). **C** Illustration of the Na⁺/K⁺-ATPase pump actively transporting two K⁺ ions into the cell and three Na⁺ ions out of the cell using energy from ATP hydrolysis.

CMap gives as a readout a list of perturbagens (almost 9,000), which can be overexpressed and downregulated genes (5,959) or compounds (2,837), that have a connectivity score (also called median tau score). These genes and compounds are then organised in a graph based on their connectivity score (**Fig. 12 B**). Positive scores denote similarities between the input dataset (our models in this case) and the datasets in the CMap, whereas negative connectivity score denote opposite signatures. As illustrated seen in **Fig. 12 B**, established NFE2L2 and KEAP1 models have positive scores for NFE2L2 gene overexpression (OE) and KEAP1 gene knockdown (KD), which is in line with activating and inactivating mutations we generated in the models, respectively. Additionally, several NFE2L2 activators were identified with positive scores, meaning that these compounds can simulate NFE2L2 activation. These compounds included: isoliquiritigenin (ISL), parthenolide (PL), sulforaphane (SF) and 1,2 dithiole 3 thione (D3T) (70, 98-100). Contrarily, we found NFE2L2 knockdown with one of the highest positive scores, which is in line with an inverse expression pattern compared to NFE2L2 activated cells. Most interestingly, we identified a class of drugs, known as Na⁺/K⁺-ATPase inhibitors, that is able to simulate NFE2L2 gene knockdown upon treatment in the cells, namely bufalin, oua-

bain and digoxin (**Fig. 12 B i. and ii.**). These inhibitors are known to act on the myocardium contractility by acting on the Na^+/K^+ -ATPase pump (**Fig. 12 C**) and thus have therapeutic applications in cardiology (101-103).

In summary, we integrated transcriptomic data derived from NFE2L2 and KEAP1 mutated cell lines into the drug prediction tool CMap and identified a class of drugs known as ATPase inhibitors that could potentially be used to treat NFE2L2 and KEAP1 mutated patients.

3.10 NFE2L2 target genes are downregulated upon treatment with ATPase inhibitors

CMap works with expression profiles to predict drug classes that can potentially reverse gene expression. Given our prediction of ATPase inhibitors as a candidate drug class, we aimed to evaluate their ability to reverse the expression of the upregulated genes identified in our established models, specifically AKR1B10. Therefore, NFE2L2 and KEAP1 models were treated with vehicle (DMSO) and bufalin, ouabain and digoxin and treated for 24 h with a specific concentration tailored to each cell line (see **Fig. 13**).

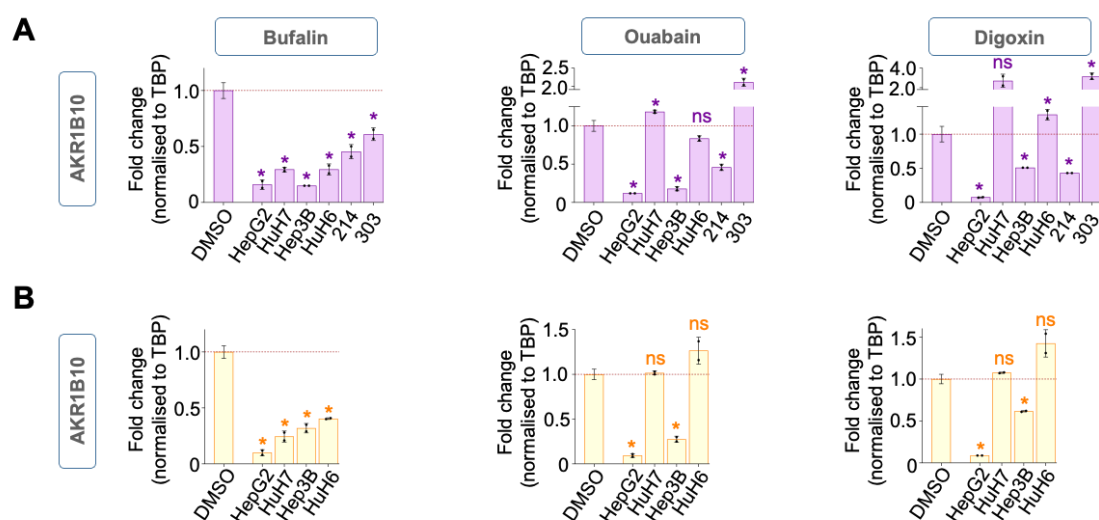


Figure 13 AKR1B10 expression in mutants upon treatment with ATPases. Expression levels of the NFE2L2 target gene AKR1B10 in (A) NFE2L2 mutants and (B) KEAP1 mutants after 24 h treatment with vehicle (DMSO) or ATPase inhibitors (bufalin, ouabain or digoxin). Treatment concentrations were as follows: HepG2 (1 μM), HuH7 (100 nM, except KEAP1 models treated with 1 μM bufalin), Hep3B (1 μM), HuH6 (100 nM), 214 (1 μM), and 303 (100 nM). TBP (TATA-binding protein) was used as a housekeeping gene for normalization of gene expression data. Expression levels of AKR1B10 was compared to untreated controls. Error bars represent the mean \pm standard deviation (SD) of one

experiment with duplicates. Statistics were calculated using a two-tailed unpaired Student's *t* test, with *ns* = not significant and $*p < 0.05$.

Quantitative PCR revealed that in general all three drugs had the capacity to lower the expression levels of AKR1B10, however, bufalin in particular was much more effective to reducing the gene repression. As seen in the **Fig. 13**, when NFE2L2 and KEAP1 models were exposed to bufalin all models showed a decrease in mRNA levels of the measured AKR1B10 gene, with statistical significance in all models.

These data clearly demonstrate that the predicted class of drugs, ATPase inhibitors, is acting on the NFE2L2 pathway by reducing the expression of NFE2L2 target gene AKR1B10. While all drugs showed moderate efficacy, bufalin was more effective in lowering the gene expression when compared to ouabain and digoxin.

3.11 Protein levels upon treatment with bufalin

In order to define the ATPase inhibitor with the highest capacity to act on NFE2L2 activated liver cancer models, we tested the three identified drugs (bufalin, ouabain and digoxin) in the HepT1 cell line that carries a *NFE2L2* mutation (86). Three distinct experiments were performed to compare the efficacy of these compounds: a reporter assay to measure NFE2L2 activity, a quantitative PCR to measure expression levels of AKR1B10, and an MTT-based viability assay (**Fig. 14**).

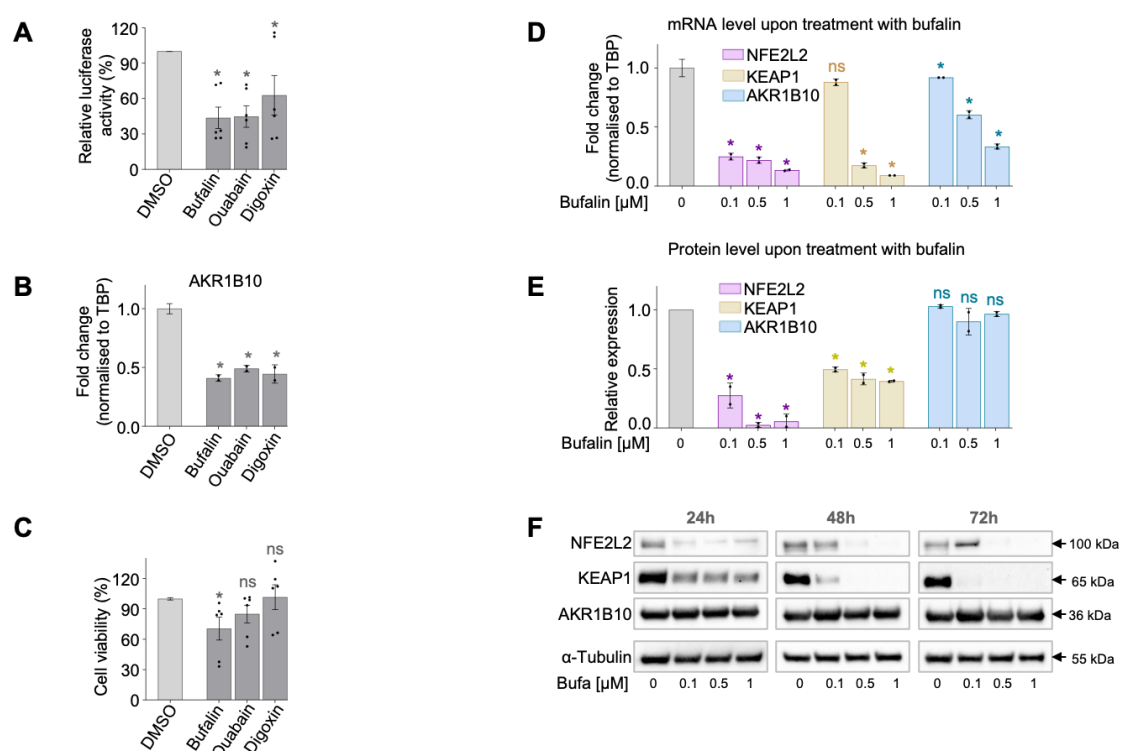


Figure 14 Effects of ATPases inhibitors on NFE2L2 pathway, AKR1B10, and viability in HepT1 cells. **A** Reporter assay experiments of HepT1 cells, transiently transfected with the pNQO1-ARE-Luc and pRL-CMV vector for 48 h and treated with vehicle (DMSO) and bufalin, ouabain and digoxin at the concentration 1 μ M for 24 h. ARE-driven luciferase activity was assessed and normalized to the activity of Renilla luciferase. Assays were performed three times with duplicates and error bars correspond to the mean \pm standard error of the mean (\pm SEM). Luciferase activity of cells treated with DMSO was normalized to 100%. **B** Expression levels of AKR1B10 in HepT1 cells treated with vehicle (DMSO) and the three ATPase inhibitors at a concentration of 1 μ M and exposed for 24 h. Gene expression levels were quantified and normalized to untreated controls. Error bars correspond the mean \pm standard deviation (SD) of one independent experiment with duplicates. **C** MTT-based viability assays of HepT1 cell line towards ATPase inhibitor exposure with 1 μ M concentration for 72 h. Error bars illustrate standard error of the mean (\pm SEM) of three separate experiments, each one with two replicates. **D** Quantitative PCR analysis depicting expression of the NFE2L2, KEAP1 and AKR1B10 gene upon treatment with vehicle (DMSO) and increasing doses of bufalin (0.1, 0.5 and 1 μ M) exposed for 24 h. Error bars display the mean \pm standard deviation (SD) of one experiment with duplicates. **E** Western blot protein quantification of NFE2L2, KEAP1 and AKR1B10 upon treatment with vehicle (DMSO) and bufalin at the concentration of 0.1, 0.5 and 1 μ M for 24 h. Error bars represent the mean \pm standard deviation (SD) of two independent experiment with duplicates. Using a two-tailed unpaired Student's *t* test statistics were calculated, with ns = not significant and * $p < 0.05$. **F** Western blot analysis illustrating the expression levels of NFE2L2 (100 kDa), KEAP1 (65 kDa) and AKR1B10 (36 kDa) proteins in HepT1 cells treated with DMSO or increasing doses of bufalin (0.1, 0.5 and 1 μ M) for 24, 48 and 72 h. α -tubulin was used as loading control (55 kDa).

In the reporter assays, bufalin and ouabain showed a similar reduction in transcriptional activity of NFE2L2, both decreasing activity to 45%, while digoxin reduced it to around 60% (**Fig. 14 A**). Quantitative PCR analysis showed that all three inhibitors effectively reduced mRNA levels of AKR1B10, though bufalin exhibited a slightly stronger reduction compared to ouabain and digoxin (**Fig. 14 B**). MTT assays revealed that bufalin reduced cell viability by approximately 30%, ouabain by 20%, and digoxin showed minimal

effect on cell death (**Fig. 11 C**). Based on the results of these three experiments, we conclude that among the ATPase inhibitors tested, bufalin demonstrates the most promising efficacy in the NFE2L2 mutated HepT1 cell line.

Mechanistically, bufalin has been described to target a plethora of pathways. The review by Soumoy and colleagues summarises how bufalin acts through direct or indirect regulation of key proteins and pathways such as MAPK (mitogen activated protein kinase), Na⁺/K⁺-ATPase, PI3K/AKT/mTOR (phosphatidylinositol 3-kinase/ak strain thymoma/mammalian target of rapamycin), NF-κB (nuclear factor kappa-light-chain-enhancer of activated B cells), SRC-3 (steroid receptor coactivator-3), HIF-1α (hypoxia-inducible factor 1-alpha) and others (see supplementary Fig. 24) (104). In order to unveil how bufalin exerts its effect on the NFE2L2-KEAP1 pathway we investigated the mRNA and protein levels of NFE2L2, KEAP1 and AKR1B10 by quantitative PCR and Western blot in NFE2L2-mutated HepT1 cells, respectively. As shown in **Fig. 14 D**, all genes exhibited a dose-dependent and significant reduction in mRNA expression following bufalin treatment for 24 h. Interestingly, this reduction was reflected on the protein level only for NFE2L2 and KEAP1, while AKR1B10 levels stayed unchanged (**Fig. 14 E**). To evaluate whether the protein expression levels would be affected upon longer exposure times, we repeated the protein extraction from HepT1 cells treated with increasing bufalin doses for 48 and 72 h. We found a drastic decrease in NFE2L2 and KEAP1 protein expression after longer drug exposure times, but not for AKR1B10 (**Fig. 14 F**).

Altogether, these results suggest that bufalin effectively downregulates both NFE2L2 and KEAP1 at the gene and protein levels in a concentration-dependent manner, indicating its potential impact on the NFE2L2-KEAP1 pathway in HepT1 cells.

3.12 Bufalin inhibits short/long term proliferation, reduces tumor spheroid growth and induces apoptosis in HepT1 cells

To explore the cellular consequences upon of bufalin exposure, we applied 100 nM of the drug on HepT1 and evaluated short/long-term proliferation, tumor spheroid volume inhibition and apoptotic properties. Using the Click-iT EdU cell proliferation kit short-term growth was detected, which revealed a significant inhibition upon treatment for 24 h (**Fig. 15 A**). Additionally, the long-term proliferation was assessed by colony formation assay after either DMSO treatment or 100 nM of bufalin for 6 days (**Fig. 15 B**). A dramatic decrease of colony formation was observed when bufalin treatment was applied. Given that the cells showed a considerably decreased ability to form colonies after treatment,

this assay shows that the reproductive integrity of tumor cells was severely compromised in long-term cultures. Next, HepT1 tumor spheroids formed in ultra-low attachment plates after 5 days underwent strong accumulation of dying cells in the spheroid center after treatment with 100 nM of bufalin for 3 additional days (**Fig. 15 C**). Moreover, apoptosis was detected upon treatment for 24 h, which revealed that there is a strong induction of apoptosis upon treatment with bufalin (**Fig. 15 D**).

The findings suggest that treatment with bufalin at nanomolar concentrations leads to a decrease of short-term and long-term cell proliferation in HepT1. Furthermore, the growth of three-dimensional tumor spheroids effectively decreased and apoptosis was triggered upon treatment with bufalin, emphasizing its strong anti-tumor properties.

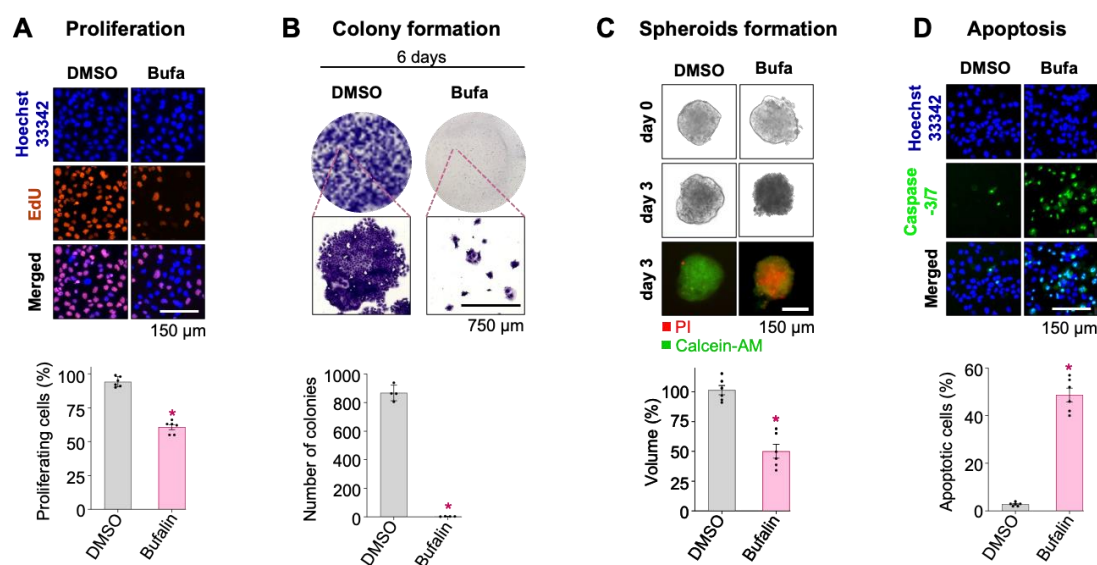


Figure 15 Cellular consequences in HepT1 cells upon treatment with bufalin. **A** Short-term proliferation evaluated HepT1 cell line treated with vehicle (DMSO) or 100 nM bufalin (Bufa) for 24 h using ethynyl deoxyuridine (EdU, red) and nuclear counterstaining with Hoechst 33342 (blue). **B** Long-term proliferation of HepT1 cells after treatment with DMSO or 100 nM bufalin for 6 days, using a colony formation assay to measure growth potential. Crystal violet-stained wells (upper panel) along with close-up views of single colonies (lower panel). **C** Brightfield images (top two panels) illustrating the three-dimensional development of HepT1 tumor spheroids following a 3-day treatment with DMSO or 100 nM Bufa. The bottom panel illustrates spheroids stained with propidium iodide (PI) (red) and calcein-acetoxymethyl (Calcein-AM) (green). **D** Apoptosis assay was conducted using fluorescent labeling of active caspase-3/7 substrates (green) and nuclei counterstained with Hoechst 33342 (blue). Images of HepT1 apoptotic cells were taken after 24-hour exposure with DMSO or 100 nM bufalin. Quantification of performed

*experiments are shown under each figure. Error bars represent the mean \pm standard error of the mean (\pm SEM) of two independent experiment with triplicates for proliferation, tumor spheroid formation and apoptosis (A+C+D). For colony formation assay (B) error bars represent the mean \pm standard deviation (SD) of two independent experiment with duplicates. Using a two-tailed unpaired Student's *t* test statistics were calculated, with * $p < 0.05$.*

3.13 Bufalin re-establishes sensitivity towards cisplatin or doxorubicin in NFE2L2 activated cells

Cisplatin is consistently used as the primary agent in all treatment phases (preoperative and postoperative) of HB, while doxorubicin serves as a supporting agent alongside cisplatin during these phases (47). When we tested the response of cisplatin and doxorubicin in our established NFE2L2-activated liver cancer models, we observed lower sensitivity to these drugs compared to non-NFE2L2-activated cells (results section chapter 3.7, **Fig. 10**). Given that bufalin effectively affected NFE2L2-activation, we explored whether bufalin could enhance the therapeutic response in tumors with reduced sensitivity to cisplatin and doxorubicin. As it can be seen in **Fig. 16** NFE2L2 and KEAP1 disrupted models, alongside with their respective parental cells were exposed towards standard chemotherapy and in combination in bufalin.

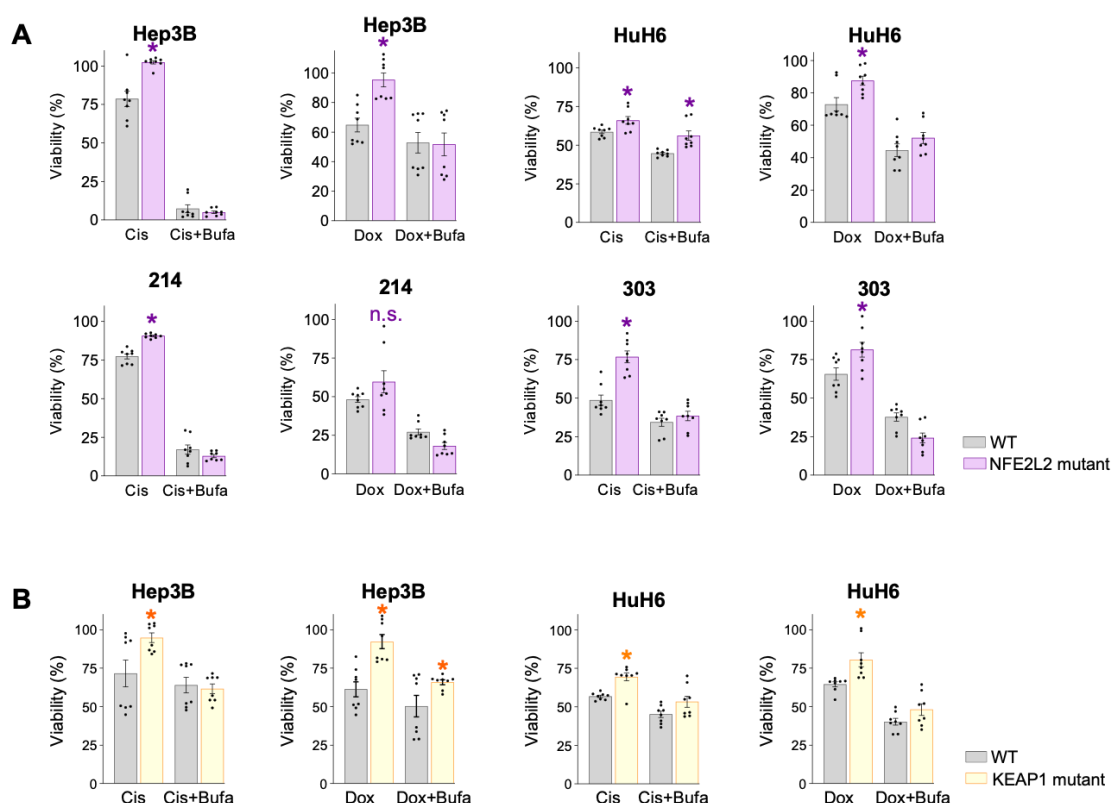


Figure 16 Bufalin enhances cytotoxic effects of cisplatin and doxorubicin in the models. MTT viability screening illustrating the cellular response of wildtype (WT), NFE2L2 (A) and KEAP1 (B) mutant clones towards cisplatin (Cis), doxorubicin (Dox) and in combination with bufalin (Bufo). All cell lines were treated with 10 μ M of Cis. Hep3B and 214 received 1 μ M of Dox, HuH6 and 303 200 nM of Dox. Hep3B received 200 nM of Bufo (except the Cis+Bufo combination in NFE2L2 mutant where 500 nM were used), 214 with 1 μ M, 303 with 200 nM and HuH6 with 300 nM (except for the Cis+Bufo combination in NFE2L2 mutant where 250 nM were used). Error bars illustrate the mean \pm standard error of the mean (SEM) from four individual experiments performed in duplicate. Using a two-tailed unpaired Student's *t* test statistics were calculated, with * $p < 0.05$ and ns = not significant.

Strikingly, the combination of cisplatin+bufalin or doxorubicin+bufalin abolished lower sensitivity to standard chemotherapy. For example, when Hep3B, 214, and 303 NFE2L2-mutated cells were treated with cisplatin alone, they showed lower sensitivity in comparison to WT cells. By contrast, treatment with cisplatin combined with bufalin resulted in comparable responses between WT and mutant cells, thereby eliminating drug insensitivity in the mutated models (Fig. 16 A).

A similar trend was observed with doxorubicin treatment: NFE2L2-mutated cells, including Hep3B, HuH6, 214, and 303, displayed reduced sensitivity to doxorubicin when used individually. However, when combined with bufalin, mutant cells responded similarly to WT cells, restoring sensitivity to the drug.

In KEAP1-mutated models, we successfully re-established sensitivity to cisplatin and doxorubicin in Hep3B and HuH6 cells, though this was not statistically significant in doxorubicin-treated Hep3B KEAP1 mutants (**Fig. 16 B**).

In summary, treating NFE2L2-activated liver cancer models with cisplatin or doxorubicin in combination with bufalin globally restored drug sensitivity in the mutated cells.

3.14 ATPase inhibitors are predicted using RNA sequencing data derived from NFE2L2 mutated patients

Using NFE2L2 and KEAP1 mutated cells, we successfully identified ATPase inhibitors as a novel class of drugs for treating NFE2L2-activated liver cancers. To validate our *in silico* prediction, we repeated the drug prediction process using RNA sequencing data from the three previously reported NFE2L2 mutated patients (T253, T577 and HepT1). We used as an input the top 50 up-regulated genes, ranked by p-value significance (see supplementary Fig. 23), into CMap for analysis. Remarkably, the perturbagen patterns (genes and drugs) predicted with patient data closely mirrored those identified using our CRISPR-Cas9 engineered models. These patients exhibited NFE2L2 gene overexpression and KEAP1 gene knockdown (**Fig. 17 A**), and the same four NFE2L2 activators were consistently predicted: ISL, PL, SF and D3T. Additionally, ATPase inhibitors were identified as potential therapeutic candidates based on the patient-derived data, as shown in the graphs of **Fig. 17 A**.

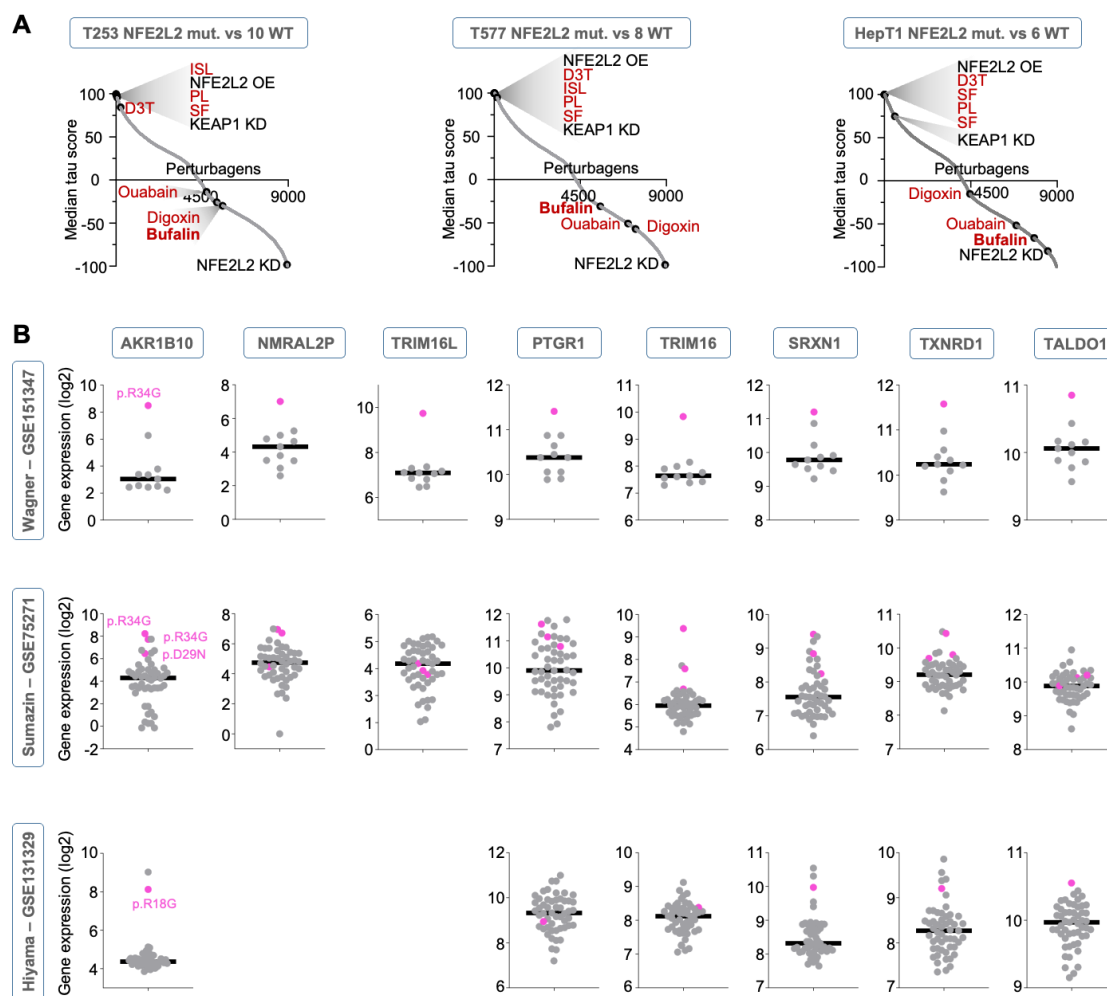


Figure 17 Drug prediction and gene expression analysis in NFE2L2-mutated patients. **A** Drug prediction using patient data (T253, T577 and HepT1) normalized to non-mutated NFE2L2 samples (WT). ConnectivityMap provides a list of perturbagens (x axis) organized by a median tau score (y axis). Perturbagens can be drugs (listed in red) or genes (listed in black) with overexpression (OE) or knockdown (KD). Isoliquiritigenin (ISL), parthenolide (PL), sulforaphane (SF), 1,2 dithiole 3 thione (D3T). **B** Gene expression of the genes AKR1B10, NMRAL2P, TRIM16L, PTGR1, TRIM16, SRXN1, TXNRD1 and TALDO1 with data retrieved from the Gene Expression Omnibus with the accession number GSE151347 (Wagner), GSE75271 (Sumazin) and GSE131329 (Hiyama). NFE2L2 mutated patients are highlighted in pink with protein mutation annotation.

Our findings confirm that the models we established are reliably and replicate patient specific mutations, driving similar transcriptional activity. This provides strong evidence supporting the use of ATPase inhibitors as a novel therapeutic strategy for NFE2L2-activated liver cancers.

As discussed in chapter 3.2, analysis of three NFE2L2-mutated patients identified a set of eight commonly upregulated genes: *AKR1B10*, *NMRAL2P*, *TRIM16L*, *PTGRI*, *TRIM16*, *SRXN1*, *TXNRD1* and *TALDO1* (**Fig. 4 C**). To determine whether other studies also reported these genes as upregulated in HB NFE2L2-mutated patients, we analysed datasets from the Gene Expression Omnibus with the accession numbers GSE131329 (Hiyama and colleagues), GSE75271 (Sumazin and colleagues) and GSE151347 (Wagner and colleagues) (**Fig. 17 B**) (17, 105, 106). The study by Wagner and colleagues included patient T253, confirming that all eight genes were highly upregulated in this patient. The study by Sumazin and colleagues reported three NFE2L2-mutated patients. Although these patients showed high expression of the eight genes, the expression levels were only slightly higher than those observed in the general cohort, making the distinction less pronounced compared to Wagner's findings. In the dataset from Hiyama and colleagues one patient with an NFE2L2 mutation was identified (personal communication Dr. Eiso Hiyama). While the expression levels of *NMRAL2P* and *TRIM16L* were not assessed in their study, the NFE2L2-mutated patient demonstrated elevated expression of *AKR1B10*, *SRXN1* and *TALDO1* compared to the rest of the cohort. Overall, a comparison of NFE2L2-mutated patients analysed in this thesis and in former studies from Sumazin and Hiyama, highlights *AKR1B10* as the most consistently and markedly upregulated gene in NFE2L2-mutated patients. This pronounced upregulation suggests that *AKR1B10* could serve as a potential biomarker for identifying NFE2L2-mutated patients.

3.15 AKR1B10 is a promising biomarker clinically relevant in

NFE2L2/KEAP1 mutated hepatoblastoma patients

In this final step of the study, we wanted to investigate if *AKR1B10* could serve as a potential biomarker for NFE2L2 activated liver cancers. Therefore, we stained the NFE2L2 mutated HepT1 cell line for this protein. According to the Human Protein Atlas, *AKR1B10* is primarily localized in the cytosol and plasma membrane. Fluorescent *AKR1B10* staining confirmed that *AKR1B10* is mainly localized in the cytosol of the cells (**Fig. 18 A**).

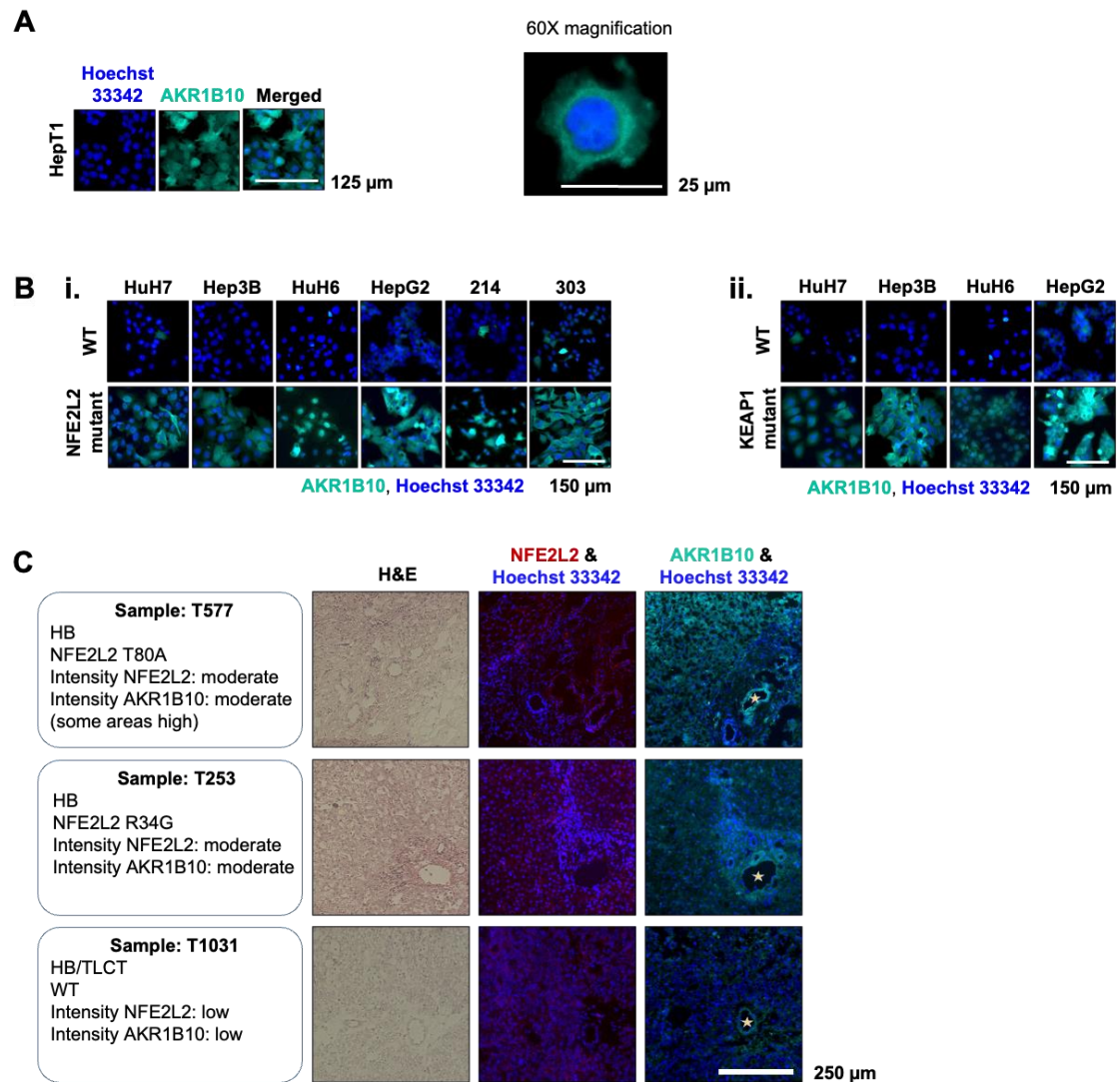


Figure 18 AKR1B10 protein localisation in parental, mutant cells and human liver cancer tissues. **A** Immunofluorescence staining of AKR1B10 protein (green) and Hoechst 33342-positive nuclei (blue) in HepT1 cells with 10X magnification. On the right side is shown merged picture with 60X magnification image of HepT1 showing AKR1B10 localization in the cytoplasm and nucleus. **B** Merged immunofluorescence images of WT versus mutant cells. In green is depicted AKR1B10 protein and in blue the nuclei. On the left (**i.**) are illustrated WT cells and respective NFE2L2 mutants and on the right side (**ii.**) WT and KEAP1 mutants. **C** Representative human HB tissues analysed by H&E and immunofluorescent staining. The first column displays general information about each tissue, the second column shows the H&E staining, the third column displays Hoechst 33342-stained nuclei (blue) and NFE2L2 protein (red), while the fourth column shows Hoechst 33342-stained nuclei alongside AKR1B10 protein (green). Periportal zones are marked by a star. Staining intensities were categorized into three levels: high, moderate and low.

Additionally, we stained wildtype, NFE2L2 and KEAP1 mutated cells for AKR1B10. The results revealed a striking difference: both NFE2L2 and KEAP1 mutated cells showed significantly higher levels of AKR1B10 compared to their parental cells (**Fig. 18 B**). This is in contrast to the abundance of NFE2L2 protein we reported before, which did not exhibit noticeable expression differences between WT and mutated cells. However, the quantification of NFE2L2 protein showed an increased nuclear accumulation of the protein in the mutants (result section 3.5 **Fig. 8 B**). Nevertheless, the strong contrast in AKR1B10 levels between WT and mutated cells underscores its higher potential to serve as a biomarker for NFE2L2-activated liver cancers than NFE2L2.

In the final step of this work, we wanted to evaluate the value of AKR1B10 as a possible biomarker candidate for NFE2L2-activated tumors in a small cohort of pediatric liver cancer patients. 19 tumor liver tissue samples were blindly stained using hematoxylin and eosin (H&E) and immunofluorescence (IF) to assess the localization of NFE2L2 and AKR1B10. **Fig. 18 C** presents three representative samples with H&E and IF staining for these proteins, while the remaining samples are documented in supplementary Fig. 25.

NFE2L2 IF demonstrated a general cytosolic distribution of the protein across the tissue samples (**Fig. 18 C**, third column). The samples showed variable intensities of NFE2L2 protein which we then classified into 3 different levels: high, moderate and low. Our analysis revealed that T577, T253 and T1031 exhibited respectively moderate, high and low levels of NFE2L2.

The AKR1B10 fluorescence intensity was also classified following the same scoring. Hence, our analysis revealed that T577 exhibited high intensity, T253 moderate intensity and T1031 low intensity. According to the literature, AKR1B10-positive cells are predominantly localized in the periportal zone, which consist of three structures; portal vein, hepatic artery and bile conduct (107). Consistent with these findings, our stained tissues showed AKR1B10-positive cells concentrated around the periportal zone (**Fig. 18 C**, fourth column). Additionally, AKR1B10 was primarily distributed within the cytosol of the cells. The following samples showed low AKR1B10 positivity: Tu6, T1004, T291, T365 and T1031 (see **Fig. 18 C** and supplementary Fig. 25). The samples with moderate intensity were the following: T577, T253, T1006, T1120, T835, T528, T227, T254, T920 and T692. Lastly, the samples that showed high AKR1B10 positivity were the following: Tü7, T629, T1100 and T1152.

In summary, AKR1B10 was identified as a promising biomarker for NFE2L2-activated cells, as it showed significantly elevated levels in NFE2L2 and KEAP1 mutated cells

when compared to WT. IF staining of NFE2L2 and AKR1B10 in tumor tissue revealed cytosolic localization of these two proteins. Next to the AKR1B10 expression in the periportal zone of the tissue, samples carrying NFE2L2 mutation had additional strong expression of AKR1B10 in the tumor tissue. These findings underscore the strong relation between AKR1B10 expression and NFE2L2 activation in HB.

4. Discussion

Whole exome sequencing of a cohort of 189 HB patients highlighted that a small group of patients harbors *NFE2L2* (5%) and *KEAP1* (1%) mutations (14, 17, 25). These mutations, well-documented in cancers such as lung, ovarian, head and neck, remain underexplored in HB (26, 75, 77, 79, 84, 85). *NFE2L2* and *KEAP1* mutations result in persistent NFE2L2-ARE signaling activation, which has been correlated with resistance towards chemotherapeutics such as cisplatin and doxorubicin (26, 75). Moreover, according to the C1/C2 classification and the 16-gene signature, *NFE2L2/KEAP1* mutated patients fall within the C2 group which has been associated with high-risk and unfavorable outcome (14, 16, 17, 25). Therefore, considering the implication of these genetic alterations in these patients, our study aimed to address two key questions: how to optimize the clinical treatment of *NFE2L2/KEAP1* mutated patients and how to identify them in larger cohorts.

Due to the limited number of HB patient carrying *NFE2L2* or *KEAP1* mutations, testing of novel agents with unknown safety profiles and pharmacokinetics is challenging. Moreover, as pharmaceutical firms have limited interest to develop agents for rare diseases, this makes the clinical treatment of these patients even more difficult. Therefore, repurposing of compounds with known safety profiles is a cost-effective and time-saving strategy (108, 109). This was achieved by using a sophisticated drug predicting tool, known as CMap developed by the Broad Institute (110). The CMap tool has been used in several studies, such as combining rapamycin and dexamethasone to induce sensitivity to otherwise dexamethasone-resistant acute lymphoblastic leukemia cells, or to use mebendazole (an anthelmintic drug) as a potential treatment to overcome cisplatin resistance in HB (111, 112). By using transcriptomic profiles of *NFE2L2* mutated patients and several *NFE2L2* or *KEAP1* CRISPR-Cas9 engineered mutant models, ATPase inhibitors were predicted by CMap as a possible class of drugs with the capacity to reverse the *NFE2L2* activity and resensitize cells to chemotherapy in our study. A series of *in vitro* experiments further defined the ATPase inhibitor bufalin as the most effective candidate drug in *NFE2L2*-activated liver cancer cells.

Previous *in vitro* studies have already identified the anticancer effect of bufalin in cancer cells. For instance, Jing and colleagues have shown that bufalin induced apoptosis in a time and concentration dependent manner in HL-60 leukemia cells (113). Moreover, apoptosis induction in cells was achieved with very low concentrations (10^{-8} M), making

it a much more effective inducing apoptotic cell death drug compared to cisplatin. Another publication reported that in human leukemia cells bufalin triggers cell death through modulation of c-Myc and Bcl-2 (B-cell lymphoma 2) expression (114). Xie and colleagues tested bufalin in a renal cell carcinoma cell line and showed that it was able alone to suppress proliferation by inducing G2/M arrest and to decrease cell viability in a time- and concentration-dependent manner (115). Additionally, the drug reduced colony formation, induced apoptosis (again at nanomolar concentration), suppressed migration and invasion, and targeted the PI3K/Akt/mTOR signaling pathway (115). Collectively, these studies reported that bufalin has strong anticancer activity regardless of the cancer type. A shared finding across different studies is that cancer cell proliferation was decreased in a time- and concentration-dependent manner upon treatment with bufalin, with observable effects at nanomolar concentration. Although the mechanisms targeted by bufalin varied across the studies, they uniformly showed that bufalin induces apoptosis. Considering these reports, our data on the effects of bufalin on HB cell lines showing a similar reduction of short- and long-term proliferation, induction of apoptosis and decrease of tumor spheroid volume, all achieved at a dose of 100nM, clearly showed the antitumoral properties of bufalin in pediatric liver cancer cells.

A study performed by Yuan and colleagues investigated how bufalin can reverse multi-drug resistance in colorectal cancer cells (116). The study reported that bufalin acts at very low concentrations (nM levels) and that it reversed the ABCB1-mediated (ATP-binding cassette subfamily B member 1) chemoresistance in colorectal cancer cells by reducing ABCB1 protein levels, making chemotherapy treatment with doxorubicin much more effective (116). Additionally, the efficacy of bufalin alone or in combination with doxorubicin was tested in xenograft mouse model, where the combination of bufalin with low doses of doxorubicin reduced tumor growth with no toxicity. In another study, Sun and colleagues have tested bufalin in colorectal cancer using mouse models (117). The key findings were that bufalin reduced tumor formation, suppressed cell proliferation, induced apoptosis and was well tolerated with no significant toxicity. Other important key findings were that bufalin inhibited activation of NF- κ B and PI3K/AKT pathways. In a recent study performed by Li and colleagues, it was found that bufalin restores cisplatin sensitivity in drug-resistant ovarian cancer by disrupting USP36/c-Myc signaling, both *in vitro* and *in vivo* (118). In addition, bufalin was able to increase the efficacy of cisplatin without adding toxicity, making it a promising combination therapy.

Considering these findings in the literature and our results, we evaluated drug response in our CRISPR-Cas9 engineered models that showed resistance towards standard of care medications. Remarkably, the combination of bufalin with cisplatin or doxorubicin successfully increased drug sensitivity towards cisplatin and doxorubicin in most of our models. We presume that an exact titration of bufalin would allow to determine its optimal therapeutic effect. Another possible future experimental plan could be to try a pre-treatment with bufalin before applying cisplatin or doxorubicin. Pre-treatment with bufalin may sensitize cells and enhance their responsiveness to subsequent cisplatin or doxorubicin treatment. Of note, the NFE2L2 and KEAP1 models derived from HuH7 and HepG2 failed to show the drug resistance towards standard of care. We presume that the altered karyotype of HuH7 parental cells could be implicated and explain why the derived models did not show the drug resistance (92). Additionally, HepG2 cell line has been reported to have a high baseline of NFE2L2 activity, this factor may limit the observable effect of additional NFE2L2/KEAP1 disruption (i.e., the pathway may already be saturated) (14).

To assess the safety and efficacy of Huachansu (a traditional Chinese medicine that contains bufalin) non-small cell lung cancer, in pancreatic cancer and in hepatocellular carcinoma, Meng and colleagues conducted a phase I pilot clinical trial (119). The main findings were that bufalin was well tolerated, 40% of the patients had a stable disease and 20% had a tumor shrinkage. The findings suggest that Huachansu has potential anticancer effects, warranting further clinical investigation. Based on these findings a phase II randomised, single-blind trial followed, where 80 patients with advanced pancreatic adenocarcinoma were treated with gemcitabine and Huachansu versus gemcitabine and placebo (120). The results showed that adding Huachansu to chemotherapy did not improve outcomes in advanced pancreatic cancer, suggesting a need for different combinations. In 2023 the efficacy and safety of Huachansu combined with standard adjuvant chemotherapy, was assessed in cohort colorectal cancer patients thorough a phase II randomised clinical trial (121). The results were encouraging as Huachansu significantly improved 3-year disease-free survival (78.2% versus 65.9%) without increasing toxicity. Overall, survival was not significantly different, however, patients receiving Huachansu experienced fewer side effects such as leukopenia. These finding suggest that Huachansu is safe and promising in certain clinical contexts when combined with standard chemotherapy.

Given our *in vitro* results and supporting evidence from the literature, the addition of bufalin to cisplatin or doxorubicin treatments presents an emerging strategy to improve

drug sensitivity in HB patients that are resistant to cisplatin or doxorubicin. This approach could not only lower the required dose of cisplatin or doxorubicin, resulting in lower toxicity, but also improve drug sensitivity. Therefore, future experiments should focus on *in vivo* testing, through subcutaneous tumor implantation in the mouse and subsequent drug testing of standard treatment of care with or without the addition of bufalin.

ATPase inhibitors are a class of drugs that inhibit the activity of ATPases, which are enzymes that facilitate the breakdown of ATP into ADP and inorganic phosphate through hydrolysis, providing energy for various cellular processes (101, 122-127). ATPase inhibitors are widely used clinically, in particular for heart failure and in research for cancer treatment. Mechanistically, we found bufalin to reduce the mRNA expression and protein levels of NFE2L2 and KEAP1 in a time- and concentration-dependent manner. There is evidence of a negative feedback loop between NFE2L2 and KEAP1 (128). When NFE2L2 levels rise, KEAP1 increases to degrade it, and when NFE2L2 levels drop, KEAP1 also decreases, preventing excessive suppression. This regulation is explained by the fact that NFE2L2 protein binds to an ARE in the KEAP1 promoter, which leads to increased transcription of KEAP1 (128). An observed discrepancy in our study was that, in HepT1 cells treated with bufalin, AKR1B10 mRNA levels decreased but the corresponding protein levels remained unchanged, even after 3 days of treatment. To explain this effect, we presume that the AKR1B10 protein is highly stable with a long half-life, or there might be a compensatory mechanism contributing to the regulation.

To address the second question of this study, how to identify NFE2L2/KEAP1 mutated patients, we looked at the RNA-seq data derived from NFE2L2 mutated patients and NFE2L2 activated models. An accurate analysis of the data revealed 8 consistently up-regulated genes with AKR1B10 being highly up-regulated. A series of studies proved that NFE2L2 directly regulates AKR family genes, including AKR1B10, through binding to AREs in their promoter regions (129, 130). Therefore, we hypothesized that AKR1B10 could be a reliable biomarker in NFE2L2 activated cancer cells. Of note, AKR1B10 is an enzyme that has been described to be implicated in drug resistance to chemotherapeutics, including cisplatin and doxorubicin (131, 132). Doxorubicin resistance is induced through enzymatic reduction of the drug, while cisplatin resistance indirectly through modulation of oxidative stress and signaling pathways, without metabolizing the drug itself (131, 132).

Other studies reported high expression levels of AKR1B10 in HCC and in hepatic tissues of chronic hepatitis C, identifying AKR1B10 as a possible biomarker for identifying patients at high-risk for HCC (107, 133). The only biomarker widely considered and clinically used for hepatoblastoma patients is AFP. AFP is considered as a reliable biomarker for assessing prognosis and monitoring treatment response in HB, however, it can't be used to identify NFE2L2 activation (44). According to a study by Ye and colleagues, AKR1B10 demonstrated superior diagnostic accuracy for HCC with a high sensitivity and specificity, outperforming AFP (134).

Strikingly, when we stained our NFE2L2-activated models, a high cytoplasmatic and nuclear positivity of AKR1B10 was observed. To see if this applies to biopsies derived from a series of pediatric liver cancers, we stained blindly 19 liver tissues for AKR1B10. Four samples had high AKR1B10 positivity (Tü7, T629, T1100, T1152). Sanger sequencing analysis revealed that only Tü7 was NFE2L2 mutated. Future experiments should focus on investigating if other genes that drive NFE2L2 activation (KEAP1 or CUL3) are mutated in these cases. This could explain why some samples were expressing high AKR1B10 positivity but not carrying a NFE2L2 mutation. Another set of samples (T577, T253, T1006, T1120, T835, T528, T227, T254, T920 and T692) revealed a moderate AKR1B10 intensity with only 2 of them being NFE2L2 mutated (T577 and T253). As this analysis gave no clear definition when to discern between positive and negative and correlate this with the mutations, future experiments should focus on the immunohistochemical staining of the samples. The gold standard in clinical pathology is immunohistochemical staining, especially for cancer biomarker evaluation. Immunofluorescence can introduce bias and even false positives, especially due to light intensity, exposure settings and nonspecific staining. Thus, future steps should include AKR1B10 immunohistochemical staining complemented with Sanger sequencing and staining for other biomarkers for liver cancer.

4.1 Perspectives and future directions

Analysis of the cell lines and PDXs used within this study revealed that HuH7 cells display an exon 2 skipping at the RNA level. As the mutation observed in HuH7 did not result in a truncated protein, this RNA variant represents most likely an alternative splicing rather than a deletion at the DNA level. Nevertheless, future experiments should focus on investigation of exon 2 deletion in pediatric liver tumor patients, as this kind of mutation has been reported to occur in HCC (24). Recent findings have reported KEAP1 to be

mutated in HB (25). In HCC KEAP1 mutation have been reported to occur between exons 2 and 6, suggesting that a particular attention should be given in these regions (77). A series of functional studies have demonstrated that knockout of CUL3 leads to NFE2L2 protein accumulation and subsequent NFE2L2-ARE activation due to impaired degradation of NFE2L2 (68, 135). While *CUL3* mutations have not yet been reported in HB or HCC, evidence from knockout studies confirm that CUL3 can activate the NFE2L2-ARE pathway. Thus, both *KEAP1* and *CUL3* should be considered to be investigated for possible mutations, which could possibly explain why some of our AKR1B10 highly positive tumor samples were not NFE2L2 mutated.

As discussed, a series of *in vitro*, *in vivo* and clinical trials have demonstrated the efficacy of bufalin across various cancer types. Based on our *in vitro* preliminary positive results of bufalin testing in NFE2L2/KEAP1-mutated cancer models, future studies should explore bufalin *in vivo*.

Additionally, as this study has identified AKR1B10 as a possible biomarker enriched in NFE2L2/KEAP1 mutated HB, future research should focus on pathway analysis in which AKR1B10 is involved and assess its potential as a therapeutic target considering its role in inactivating chemotherapeutic drugs. We believe that AKR1B10 may serve not only as a biomarker for the identification of these patients in larger cohorts but also as a clinically relevant indicator of patient response and prognosis.

References

1. Bray F, Laversanne M, Sung H, Ferlay J, Siegel RL, Soerjomataram I, et al. Global cancer statistics 2022: GLOBOCAN estimates of incidence and mortality worldwide for 36 cancers in 185 countries. *CA Cancer J Clin.* 2024;74(3):229-63.
2. Llovet JM, Kelley RK, Villanueva A, Singal AG, Pikarsky E, Roayaie S, et al. Hepatocellular carcinoma. *Nat Rev Dis Primers.* 2021;7(1):6.
3. Zimmermann A. The emerging family of hepatoblastoma tumours: from ontogenesis to oncogenesis. *Eur J Cancer.* 2005;41(11):1503-14.
4. Stiller CA, Pritchard J, Steliarova-Foucher E. Liver cancer in European children: incidence and survival, 1978-1997. Report from the Automated Childhood Cancer Information System project. *Eur J Cancer.* 2006;42(13):2115-23.
5. Blik J, Gicquel C, Maas S, Gaston V, Le Bouc Y, Mannens M. Epigenotyping as a tool for the prediction of tumor risk and tumor type in patients with Beckwith-Wiedemann syndrome (BWS). *J Pediatr.* 2004;145(6):796-9.
6. DeBaun MR, Tucker MA. Risk of cancer during the first four years of life in children from The Beckwith-Wiedemann Syndrome Registry. *J Pediatr.* 1998;132(3 Pt 1):398-400.
7. Giardiello FM, Offerhaus GJ, Krush AJ, Booker SV, Tersmette AC, Mulder JW, et al. Risk of hepatoblastoma in familial adenomatous polyposis. *J Pediatr.* 1991;119(5):766-8.
8. Hirschman BA, Pollock BH, Tomlinson GE. The spectrum of APC mutations in children with hepatoblastoma from familial adenomatous polyposis kindreds. *J Pediatr.* 2005;147(2):263-6.
9. Kitanovski L, Ovcak Z, Jazbec J. Multifocal hepatoblastoma in a 6-month-old girl with trisomy 18: a case report. *J Med Case Rep.* 2009;3:8319.
10. Spector LG, Birch J. The epidemiology of hepatoblastoma. *Pediatr Blood Cancer.* 2012;59(5):776-9.
11. McLaughlin CC, Baptiste MS, Schymura MJ, Nasca PC, Zdeb MS. Maternal and infant birth characteristics and hepatoblastoma. *Am J Epidemiol.* 2006;163(9):818-28.
12. von Schweinitz D. Hepatoblastoma: recent developments in research and treatment. *Semin Pediatr Surg.* 2012;21(1):21-30.
13. Spector LG, Feusner JH, Ross JA. Hepatoblastoma and low birth weight. *Pediatr Blood Cancer.* 2004;43(6):706.
14. Eichenmüller M, Trippel F, Kreuder M, Beck A, Schwarzmayer T, Häberle B, et al. The genomic landscape of hepatoblastoma and their progenies with HCC-like features. *J Hepatol.* 2014;61(6):1312-20.
15. Gröbner SN, Worst BC, Weischenfeldt J, Buchhalter I, Kleinheinz K, Rudneva VA, et al. The landscape of genomic alterations across childhood cancers. *Nature.* 2018;555(7696):321-7.
16. Cairo S, Armengol C, De Reyniès A, Wei Y, Thomas E, Renard CA, et al. Hepatic stem-like phenotype and interplay of Wnt/beta-catenin and Myc signaling in aggressive childhood liver cancer. *Cancer Cell.* 2008;14(6):471-84.
17. Sumazin P, Chen Y, Treviño LR, Sarabia SF, Hampton OA, Patel K, et al. Genomic analysis of hepatoblastoma identifies distinct molecular and prognostic subgroups. *Hepatology.* 2017;65(1):104-21.
18. Barker N, Clevers H. Mining the Wnt pathway for cancer therapeutics. *Nat Rev Drug Discov.* 2006;5(12):997-1014.
19. Oda H, Imai Y, Nakatsuru Y, Hata J, Ishikawa T. Somatic mutations of the APC gene in sporadic hepatoblastomas. *Cancer Res.* 1996;56(14):3320-3.

20. Taniguchi K, Roberts LR, Aderca IN, Dong X, Qian C, Murphy LM, et al. Mutational spectrum of beta-catenin, AXIN1, and AXIN2 in hepatocellular carcinomas and hepatoblastomas. *Oncogene*. 2002;21(31):4863-71.
21. Koch A, Weber N, Waha A, Hartmann W, Denkhaus D, Behrens J, et al. Mutations and elevated transcriptional activity of conductin (AXIN2) in hepatoblastomas. *J Pathol*. 2004;204(5):546-54.
22. Klaus A, Birchmeier W. Wnt signalling and its impact on development and cancer. *Nat Rev Cancer*. 2008;8(5):387-98.
23. Bläker H, Hofmann WJ, Rieker RJ, Penzel R, Graf M, Otto HF. Beta-catenin accumulation and mutation of the CTNNB1 gene in hepatoblastoma. *Genes Chromosomes Cancer*. 1999;25(4):399-402.
24. Goldstein LD, Lee J, Gnad F, Klijn C, Schaub A, Reeder J, et al. Recurrent Loss of NFE2L2 Exon 2 Is a Mechanism for Nrf2 Pathway Activation in Human Cancers. *Cell Rep*. 2016;16(10):2605-17.
25. Pire A, Hirsch TZ, Morcrette G, Imbeaud S, Gupta B, Pilet J, et al. Mutational signature, cancer driver genes mutations and transcriptomic subgroups predict hepatoblastoma survival. *Eur J Cancer*. 2024;200:113583.
26. Wang XJ, Sun Z, Villeneuve NF, Zhang S, Zhao F, Li Y, et al. Nrf2 enhances resistance of cancer cells to chemotherapeutic drugs, the dark side of Nrf2. *Carcinogenesis*. 2008;29(6):1235-43.
27. Aubert G, Lansdorp PM. Telomeres and aging. *Physiol Rev*. 2008;88(2):557-79.
28. Horn S, Figl A, Rachakonda PS, Fischer C, Sucker A, Gast A, et al. TERT promoter mutations in familial and sporadic melanoma. *Science*. 2013;339(6122):959-61.
29. Cesare AJ, Reddel RR. Alternative lengthening of telomeres: models, mechanisms and implications. *Nature Reviews Genetics*. 2010;11(5):319-30.
30. Hartmann W, Küchler J, Koch A, Friedrichs N, Waha A, Endl E, et al. Activation of phosphatidylinositol-3'-kinase/AKT signaling is essential in hepatoblastoma survival. *Clin Cancer Res*. 2009;15(14):4538-45.
31. Baynam GS, Goldblatt J. A child with an FGFR3 mutation, a laterality disorder and an hepatoblastoma: novel associations and possible gene-environment interactions. *Twin Res Hum Genet*. 2010;13(4):297-300.
32. Jia D, Dong R, Jing Y, Xu D, Wang Q, Chen L, et al. Exome sequencing of hepatoblastoma reveals novel mutations and cancer genes in the Wnt pathway and ubiquitin ligase complex. *Hepatology*. 2014;60(5):1686-96.
33. Eichenmüller M, Gruner I, Hagl B, Häberle B, Müller-Höcker J, von Schweinitz D, et al. Blocking the hedgehog pathway inhibits hepatoblastoma growth. *Hepatology*. 2009;49(2):482-90.
34. Regel I, Eichenmüller M, Joppien S, Liebl J, Häberle B, Müller-Höcker J, et al. IGFBP3 impedes aggressive growth of pediatric liver cancer and is epigenetically silenced in vascular invasive and metastatic tumors. *Mol Cancer*. 2012;11:9.
35. Tomlinson GE, Kappler R. Genetics and epigenetics of hepatoblastoma. *Pediatr Blood Cancer*. 2012;59(5):785-92.
36. Perilongo G, Shafford E, Plaschkes J. SIOPEL trials using preoperative chemotherapy in hepatoblastoma. *Lancet Oncol*. 2000;1:94-100.
37. Hiyama E. Pediatric hepatoblastoma: diagnosis and treatment. *Transl Pediatr*. 2014;3(4):293-9.
38. Pritchard J, da Cunha A, Cornbleet MA, Carter CJ. Alpha feto (α FP) monitoring of response to adriamycin in hepatoblastoma. *Journal of Pediatric Surgery*. 1982;17(4):429-30.
39. Herzog CE, Andrassy RJ, Eftekhari F. Childhood cancers: hepatoblastoma. *Oncologist*. 2000;5(6):445-53.

40. López-Terrada D, Alaggio R, de Dávila MT, Czauderna P, Hiyama E, Katzenstein H, et al. Towards an international pediatric liver tumor consensus classification: proceedings of the Los Angeles COG liver tumors symposium. *Mod Pathol*. 2014;27(3):472-91.
41. Stocker JT. Hepatoblastoma. *Semin Diagn Pathol*. 1994;11(2):136-43.
42. Czauderna P, Lopez-Terrada D, Hiyama E, Häberle B, Malogolowkin MH, Meyers RL. Hepatoblastoma state of the art: pathology, genetics, risk stratification, and chemotherapy. *Curr Opin Pediatr*. 2014;26(1):19-28.
43. Trobaugh-Lotrario AD, Tomlinson GE, Finegold MJ, Gore L, Feusner JH. Small cell undifferentiated variant of hepatoblastoma: adverse clinical and molecular features similar to rhabdoid tumors. *Pediatr Blood Cancer*. 2009;52(3):328-34.
44. Meyers RL, Maibach R, Hiyama E, Häberle B, Krailo M, Rangaswami A, et al. Risk-stratified staging in paediatric hepatoblastoma: a unified analysis from the Children's Hepatic tumors International Collaboration. *Lancet Oncol*. 2017;18(1):122-31.
45. Aronson DC, Schnater JM, Staalman CR, Weverling GJ, Plaschkes J, Perilongo G, et al. Predictive value of the pretreatment extent of disease system in hepatoblastoma: results from the International Society of Pediatric Oncology Liver Tumor Study Group SIOPEL-1 study. *J Clin Oncol*. 2005;23(6):1245-52.
46. Perilongo G, Shafford E, Maibach R, Aronson D, Brugières L, Brock P, et al. Risk-adapted treatment for childhood hepatoblastoma: final report of the second study of the International Society of Paediatric Oncology—SIOPEL 2. *European Journal of Cancer*. 2004;40(3):411-21.
47. Zsiros J, Brugières L, Brock P, Roebuck D, Maibach R, Zimmermann A, et al. Dose-dense cisplatin-based chemotherapy and surgery for children with high-risk hepatoblastoma (SIOPEL-4): a prospective, single-arm, feasibility study. *Lancet Oncol*. 2013;14(9):834-42.
48. Zsiros J, Maibach R, Shafford E, Brugières L, Brock P, Czauderna P, et al. Successful treatment of childhood high-risk hepatoblastoma with dose-intensive multiagent chemotherapy and surgery: final results of the SIOPEL-3HR study. *J Clin Oncol*. 2010;28(15):2584-90.
49. Fuchs J, Rydzynski J, Von Schweinitz D, Bode U, Hecker H, Weinel P, et al. Pretreatment prognostic factors and treatment results in children with hepatoblastoma: a report from the German Cooperative Pediatric Liver Tumor Study HB 94. *Cancer*. 2002;95(1):172-82.
50. Ortega JA, Douglass EC, Feusner JH, Reynolds M, Quinn JJ, Finegold MJ, et al. Randomized comparison of cisplatin/vincristine/fluorouracil and cisplatin/continuous infusion doxorubicin for treatment of pediatric hepatoblastoma: A report from the Children's Cancer Group and the Pediatric Oncology Group. *J Clin Oncol*. 2000;18(14):2665-75.
51. Perilongo G, Maibach R, Shafford E, Brugières L, Brock P, Morland B, et al. Cisplatin versus cisplatin plus doxorubicin for standard-risk hepatoblastoma. *N Engl J Med*. 2009;361(17):1662-70.
52. Hishiki T, Matsunaga T, Sasaki F, Yano M, Ida K, Horie H, et al. Outcome of hepatoblastomas treated using the Japanese Study Group for Pediatric Liver Tumor (JPLT) protocol-2: report from the JPLT. *Pediatr Surg Int*. 2011;27(1):1-8.
53. Häberle B, Schweinitz Dv. Treatment of hepatoblastoma in the German cooperative pediatric liver tumor studies. *FBE*. 2012;4(1):493-8.
54. Lipshultz SE, Sambatakos P, Maguire M, Karnik R, Ross SW, Franco VI, et al. Cardiotoxicity and cardioprotection in childhood cancer. *Acta Haematol*. 2014;132(3-4):391-9.

55. Knight KR, Kraemer DF, Neuwelt EA. Ototoxicity in children receiving platinum chemotherapy: underestimating a commonly occurring toxicity that may influence academic and social development. *J Clin Oncol*. 2005;23(34):8588-96.
56. Rybak LP, Whitworth CA, Mukherjee D, Ramkumar V. Mechanisms of cisplatin-induced ototoxicity and prevention. *Hearing Research*. 2007;226(1):157-67.
57. Womer RB, Pritchard J, Barratt TM. Renal toxicity of cisplatin in children. *J Pediatr*. 1985;106(4):659-63.
58. Brock Penelope R, Maibach R, Childs M, Rajput K, Roebuck D, Sullivan Michael J, et al. Sodium Thiosulfate for Protection from Cisplatin-Induced Hearing Loss. *New England Journal of Medicine*. 2018;378(25):2376-85.
59. Moi P, Chan K, Asunis I, Cao A, Kan YW. Isolation of NF-E2-related factor 2 (Nrf2), a NF-E2-like basic leucine zipper transcriptional activator that binds to the tandem NF-E2/AP1 repeat of the beta-globin locus control region. *Proc Natl Acad Sci U S A*. 1994;91(21):9926-30.
60. Huang HC, Nguyen T, Pickett CB. Regulation of the antioxidant response element by protein kinase C-mediated phosphorylation of NF-E2-related factor 2. *Proc Natl Acad Sci U S A*. 2000;97(23):12475-80.
61. Itoh K, Wakabayashi N, Katoh Y, Ishii T, Igarashi K, Engel JD, et al. Keap1 represses nuclear activation of antioxidant responsive elements by Nrf2 through binding to the amino-terminal Neh2 domain. *Genes Dev*. 1999;13(1):76-86.
62. Tong KI, Yasutake K, Hideki K, Ken I, Toshiyuki T, and Yamamoto M. Keap1 Recruits Neh2 through Binding to ETGE and DLG Motifs: Characterization of the Two-Site Molecular Recognition Model. *Molecular and Cellular Biology*. 2006;26(8):2887-900.
63. Nioi P, Truyen N, J. SP, and Pickett CB. The Carboxy-Terminal Neh3 Domain of Nrf2 Is Required for Transcriptional Activation. *Molecular and Cellular Biology*. 2005;25(24):10895-906.
64. McMahon M, Thomas N, Itoh K, Yamamoto M, Hayes JD. Redox-regulated turnover of Nrf2 is determined by at least two separate protein domains, the redox-sensitive Neh2 degron and the redox-insensitive Neh6 degron. *J Biol Chem*. 2004;279(30):31556-67.
65. Zhang J, Hosoya T, Maruyama A, Nishikawa K, Maher Jonathan M, Ohta T, et al. Nrf2 Neh5 domain is differentially utilized in the transactivation of cytoprotective genes. *Biochemical Journal*. 2007;404(3):459-66.
66. Chowdhry S, Zhang Y, McMahon M, Sutherland C, Cuadrado A, Hayes JD. Nrf2 is controlled by two distinct β -TrCP recognition motifs in its Neh6 domain, one of which can be modulated by GSK-3 activity. *Oncogene*. 2013;32(32):3765-81.
67. Wang H, Liu K, Geng M, Gao P, Wu X, Hai Y, et al. RXR α inhibits the NRF2-ARE signaling pathway through a direct interaction with the Neh7 domain of NRF2. *Cancer Res*. 2013;73(10):3097-108.
68. Furukawa M, Xiong Y. BTB protein Keap1 targets antioxidant transcription factor Nrf2 for ubiquitination by the Cullin 3-Roc1 ligase. *Mol Cell Biol*. 2005;25(1):162-71.
69. Itoh K, Chiba T, Takahashi S, Ishii T, Igarashi K, Katoh Y, et al. An Nrf2/small Maf heterodimer mediates the induction of phase II detoxifying enzyme genes through antioxidant response elements. *Biochem Biophys Res Commun*. 1997;236(2):313-22.
70. Houghton CA, Fassett RG, Coombes JS. Sulforaphane and Other Nutrigenomic Nrf2 Activators: Can the Clinician's Expectation Be Matched by the Reality? *Oxid Med Cell Longev*. 2016;2016:7857186.
71. Friling RS, Bergelson S, Daniel V. Two adjacent AP-1-like binding sites form the electrophile-responsive element of the murine glutathione S-transferase Ya subunit gene. *Proc Natl Acad Sci U S A*. 1992;89(2):668-72.

72. Sangokoya C, Telen MJ, Chi JT. microRNA miR-144 modulates oxidative stress tolerance and associates with anemia severity in sickle cell disease. *Blood*. 2010;116(20):4338-48.
73. Alam J, Stewart D, Touchard C, Boinapally S, Choi AM, Cook JL. Nrf2, a Cap'n'Collar transcription factor, regulates induction of the heme oxygenase-1 gene. *J Biol Chem*. 1999;274(37):26071-8.
74. Wild AC, Moinova HR, Mulcahy RT. Regulation of gamma-glutamylcysteine synthetase subunit gene expression by the transcription factor Nrf2. *J Biol Chem*. 1999;274(47):33627-36.
75. Shibata T, Ohta T, Tong KI, Kokubu A, Odogawa R, Tsuta K, et al. Cancer related mutations in NRF2 impair its recognition by Keap1-Cul3 E3 ligase and promote malignancy. *Proc Natl Acad Sci U S A*. 2008;105(36):13568-73.
76. Kim YR, Oh JE, Kim MS, Kang MR, Park SW, Han JY, et al. Oncogenic NRF2 mutations in squamous cell carcinomas of oesophagus and skin. *J Pathol*. 2010;220(4):446-51.
77. Schulze K, Imbeaud S, Letouzé E, Alexandrov LB, Calderaro J, Rebouissou S, et al. Exome sequencing of hepatocellular carcinomas identifies new mutational signatures and potential therapeutic targets. *Nat Genet*. 2015;47(5):505-11.
78. Kobayashi A, Kang MI, Okawa H, Ohtsui M, Zenke Y, Chiba T, et al. Oxidative stress sensor Keap1 functions as an adaptor for Cul3-based E3 ligase to regulate proteasomal degradation of Nrf2. *Mol Cell Biol*. 2004;24(16):7130-9.
79. Suzuki T, Maher J, Yamamoto M. Select heterozygous Keap1 mutations have a dominant-negative effect on wild-type Keap1 in vivo. *Cancer Res*. 2011;71(5):1700-9.
80. Yamamoto T, Takafumi S, Akira K, Junko W, Jon M, Hozumi M, et al. Physiological Significance of Reactive Cysteine Residues of Keap1 in Determining Nrf2 Activity. *Molecular and Cellular Biology*. 2008;28(8):2758-70.
81. Saito R, Takafumi S, Keiichiro H, Soichiro A, Eriko N, Hiromi S, et al. Characterizations of Three Major Cysteine Sensors of Keap1 in Stress Response. *Molecular and Cellular Biology*. 2016;36(2):271-84.
82. Hong F, Freeman ML, Liebler DC. Identification of sensor cysteines in human Keap1 modified by the cancer chemopreventive agent sulforaphane. *Chem Res Toxicol*. 2005;18(12):1917-26.
83. Fukutomi T, Kenji T, Tsunehiro M, Noriaki O, and Yamamoto M. Kinetic, Thermodynamic, and Structural Characterizations of the Association between Nrf2-DLGex Degron and Keap1. *Molecular and Cellular Biology*. 2014;34(5):832-46.
84. Ohta T, Iijima K, Miyamoto M, Nakahara I, Tanaka H, Ohtsui M, et al. Loss of Keap1 function activates Nrf2 and provides advantages for lung cancer cell growth. *Cancer Res*. 2008;68(5):1303-9.
85. Konstantinopoulos PA, Spentzos D, Fountzilias E, Francoeur N, Sanisetty S, Gramatikos AP, et al. Keap1 mutations and Nrf2 pathway activation in epithelial ovarian cancer. *Cancer Res*. 2011;71(15):5081-9.
86. Pietsch T, Fonatsch C, Albrecht S, Maschek H, Wolf HK, von Schweinitz D. Characterization of the continuous cell line HepT1 derived from a human hepatoblastoma. *Lab Invest*. 1996;74(4):809-18.
87. Chen W, Wong C, Vosburgh E, Levine AJ, Foran DJ, Xu EY. High-throughput image analysis of tumor spheroids: a user-friendly software application to measure the size of spheroids automatically and accurately. *J Vis Exp*. 2014(89).
88. Ran FA, Hsu PD, Wright J, Agarwala V, Scott DA, Zhang F. Genome engineering using the CRISPR-Cas9 system. *Nature Protocols*. 2013;8(11):2281-308.
89. Zheng A, Chevalier N, Calderoni M, Dubuis G, Dormond O, Ziros PG, et al. CRISPR/Cas9 genome-wide screening identifies KEAP1 as a sorafenib, lenvatinib, and

- regorafenib sensitivity gene in hepatocellular carcinoma. *Oncotarget*. 2019;10(66):7058-70.
90. Jeong Y, Hellyer JA, Stehr H, Hoang NT, Niu X, Das M, et al. Role of KEAP1/NFE2L2 Mutations in the Chemotherapeutic Response of Patients with Non-Small Cell Lung Cancer. *Clin Cancer Res*. 2020;26(1):274-81.
 91. Maibach R, Roebuck D, Brugieres L, Capra M, Brock P, Dall'Igna P, et al. Prognostic stratification for children with hepatoblastoma: the SIOPEL experience. *Eur J Cancer*. 2012;48(10):1543-9.
 92. Carloni V, Lulli M, Madiati S, Mello T, Hall A, Luong TV, et al. CHK2 overexpression and mislocalisation within mitotic structures enhances chromosomal instability and hepatocellular carcinoma progression. *Gut*. 2018;67(2):348-61.
 93. Kopacz A, Rojo AI, Patibandla C, Lastra-Martínez D, Piechota-Polanczyk A, Kloska D, et al. Overlooked and valuable facts to know in the NRF2/KEAP1 field. *Free Radic Biol Med*. 2022;192:37-49.
 94. Hast BE, Cloer EW, Goldfarb D, Li H, Siesser PF, Yan F, et al. Cancer-derived mutations in KEAP1 impair NRF2 degradation but not ubiquitination. *Cancer Res*. 2014;74(3):808-17.
 95. Boisvert F-M, van Koningsbruggen S, Navascués J, Lamond AI. The multifunctional nucleolus. *Nature Reviews Molecular Cell Biology*. 2007;8(7):574-85.
 96. Satoh H, Moriguchi T, Saigusa D, Baird L, Yu L, Rokutan H, et al. NRF2 Intensifies Host Defense Systems to Prevent Lung Carcinogenesis, but After Tumor Initiation Accelerates Malignant Cell Growth. *Cancer Res*. 2016;76(10):3088-96.
 97. Subramanian A, Tamayo P, Mootha VK, Mukherjee S, Ebert BL, Gillette MA, et al. Gene set enrichment analysis: A knowledge-based approach for interpreting genome-wide expression profiles. *Proceedings of the National Academy of Sciences*. 2005;102(43):15545-50.
 98. Liu Q, Lv H, Wen Z, Ci X, Peng L. Isoliquiritigenin Activates Nuclear Factor Erythroid-2 Related Factor 2 to Suppress the NOD-Like Receptor Protein 3 Inflammasome and Inhibits the NF- κ B Pathway in Macrophages and in Acute Lung Injury. *Front Immunol*. 2017;8:1518.
 99. Kim CY, Kang B, Hong J, Choi HS. Parthenolide inhibits lipid accumulation via activation of Nrf2/Keap1 signaling during adipocyte differentiation. *Food Sci Biotechnol*. 2020;29(3):431-40.
 100. Cui Y, Ma S, Zhang C, Li D, Yang B, Lv P, et al. Pharmacological activation of the Nrf2 pathway by 3H-1, 2-dithiole-3-thione is neuroprotective in a mouse model of Alzheimer disease. *Behav Brain Res*. 2018;336:219-26.
 101. Laursen M, Gregersen JL, Yatime L, Nissen P, Fedosova NU. Structures and characterization of digoxin- and bufalin-bound Na⁺,K⁺-ATPase compared with the ouabain-bound complex. *Proc Natl Acad Sci U S A*. 2015;112(6):1755-60.
 102. Gable ME, Ellis L, Fedorova OV, Bagrov AY, Askari A. Comparison of Digitalis Sensitivities of Na⁽⁺⁾/K⁽⁺⁾-ATPases from Human and Pig Kidneys. *ACS Omega*. 2017;2(7):3610-5.
 103. Garcia DG, Castro-Faria-Neto HCd, Silva CId, Souza e Souza KFCd, Gonçalves-de-Albuquerque CF, Silva AR, et al. Na/K-ATPase as a target for anticancer drugs: studies with perillyl alcohol. *Molecular Cancer*. 2015;14(1):105.
 104. Soumoy L, Ghanem GE, Saussez S, Journe F. Bufalin for an innovative therapeutic approach against cancer. *Pharmacol Res*. 2022;184:106442.
 105. Wagner AE, Schwarzmayer T, Häberle B, Vokuhl C, Schmid I, von Schweinitz D, et al. SP8 Promotes an Aggressive Phenotype in Hepatoblastoma via FGF8 Activation. *Cancers (Basel)*. 2020;12(8).

106. Kanawa M, Hiyama E, Kawashima K, Hiyama K, Ikeda K, Morihara N, et al., editors. Gene expression profiling in hepatoblastoma cases of the Japanese Study Group for Pediatric Liver Tumors-2 (JPLT-2) trial 2019.
107. Sato S, Genda T, Hirano K, Tsuzura H, Narita Y, Kanemitsu Y, et al. Up-regulated aldo-keto reductase family 1 member B10 in chronic hepatitis C: association with serum alpha-fetoprotein and hepatocellular carcinoma. *Liver Int.* 2012;32(9):1382-90.
108. Qu XA, Rajpal DK. Applications of Connectivity Map in drug discovery and development. *Drug Discovery Today.* 2012;17(23):1289-98.
109. Nosengo N. Can you teach old drugs new tricks? *Nature.* 2016;534(7607):314-6.
110. Lamb J. The Connectivity Map: a new tool for biomedical research. *Nat Rev Cancer.* 2007;7(1):54-60.
111. Wei G, Twomey D, Lamb J, Schlis K, Agarwal J, Stam RW, et al. Gene expression-based chemical genomics identifies rapamycin as a modulator of MCL1 and glucocorticoid resistance. *Cancer Cell.* 2006;10(4):331-42.
112. Li Q, Demir S, Del Río-Álvarez Á, Maxwell R, Wagner A, Carrillo-Reixach J, et al. Targeting the Unwindosome by Mebendazole Is a Vulnerability of Chemoresistant Hepatoblastoma. *Cancers (Basel).* 2022;14(17).
113. Jing Y, Ohizumi H, Kawazoe N, Hashimoto S, Masuda Y, Nakajo S, et al. Selective inhibitory effect of bufalin on growth of human tumor cells in vitro: association with the induction of apoptosis in leukemia HL-60 cells. *Jpn J Cancer Res.* 1994;85(6):645-51.
114. Masuda Y, Kawazoe N, Nakajo S, Yoshida T, Kuroiwa Y, Nakaya K. Bufalin induces apoptosis and influences the expression of apoptosis-related genes in human leukemia cells. *Leuk Res.* 1995;19(8):549-56.
115. Xie J, Lin W, Huang L, Xu N, Xu A, Chen B, et al. Bufalin suppresses the proliferation and metastasis of renal cell carcinoma by inhibiting the PI3K/Akt/mTOR signaling pathway. *Oncol Lett.* 2018;16(3):3867-73.
116. Yuan ZT, Shi XJ, Yuan YX, Qiu YY, Zou Y, Liu C, et al. Bufalin reverses ABCB1-mediated drug resistance in colorectal cancer. *Oncotarget.* 2017;8(29):48012-26.
117. Sun X, Ng TTH, Sham K WY, Zhang L, Chan MTV, Wu WKK, et al. Bufalin, a Traditional Chinese Medicine Compound, Prevents Tumor Formation in Two Murine Models of Colorectal Cancer. *Cancer Prev Res (Phila).* 2019;12(10):653-66.
118. Li B, Tan S, Yu X, Wang Y. Bufalin: A promising therapeutic drug against the cisplatin-resistance of ovarian cancer by targeting the USP36/c-Myc axis. *Biochem Biophys Res Commun.* 2024;733:150440.
119. Meng Z, Yang P, Shen Y, Bei W, Zhang Y, Ge Y, et al. Pilot study of huachansu in patients with hepatocellular carcinoma, nonsmall-cell lung cancer, or pancreatic cancer. *Cancer.* 2009;115(22):5309-18.
120. Meng Z, Garrett CR, Shen Y, Liu L, Yang P, Huo Y, et al. Prospective randomised evaluation of traditional Chinese medicine combined with chemotherapy: a randomised phase II study of wild toad extract plus gemcitabine in patients with advanced pancreatic adenocarcinomas. *Br J Cancer.* 2012;107(3):411-6.
121. Li S, Shen D, Zuo Q, Wang S, Meng L, Yu J, et al. Efficacy and safety of Huachansu combined with adjuvant chemotherapy in resected colorectal cancer patients: a prospective, open-label, randomized phase II study. *Med Oncol.* 2023;40(12):358.
122. Skou JC. The influence of some cations on an adenosine triphosphatase from peripheral nerves. *Biochimica et Biophysica Acta.* 1957;23:394-401.

123. Mitchell P. Coupling of phosphorylation to electron and hydrogen transfer by a chemi-osmotic type of mechanism. *Nature*. 1961;191:144-8.
124. Repke KRH. A model for allosteric regulation of Na⁺/K⁺-transporting ATPase. *Biochimica et Biophysica Acta (BBA) - Reviews on Biomembranes*. 1986;864(2):195-212.
125. Yatime L, Laursen M, Morth JP, Esmann M, Nissen P, Fedosova NU. Structural insights into the high affinity binding of cardiotonic steroids to the Na⁺,K⁺-ATPase. *Journal of Structural Biology*. 2011;174(2):296-306.
126. Laursen M, Yatime L, Nissen P, Fedosova NU. Crystal structure of the high-affinity Na⁺K⁺-ATPase-ouabain complex with Mg²⁺ bound in the cation binding site. *Proc Natl Acad Sci U S A*. 2013;110(27):10958-63.
127. Schönfeld W, Weiland J, Lindig C, Masnyk M, Kabat MM, Kurek A, et al. The lead structure in cardiac glycosides is 5 beta, 14 beta-androstane-3 beta 14-diol. *Naunyn Schmiedebergs Arch Pharmacol*. 1985;329(4):414-26.
128. Lee OH, Jain AK, Papusha V, Jaiswal AK. An auto-regulatory loop between stress sensors INrf2 and Nrf2 controls their cellular abundance. *J Biol Chem*. 2007;282(50):36412-20.
129. Lou H, Du S, Ji Q, Stolz A. Induction of AKR1C2 by phase II inducers: identification of a distal consensus antioxidant response element regulated by NRF2. *Mol Pharmacol*. 2006;69(5):1662-72.
130. Penning TM, Lerman C. Genomics of smoking exposure and cessation: lessons for cancer prevention and treatment. *Cancer Prev Res (Phila)*. 2008;1(2):80-3.
131. Zhong L, Shen H, Huang C, Jing H, Cao D. AKR1B10 induces cell resistance to daunorubicin and idarubicin by reducing C13 ketonic group. *Toxicol Appl Pharmacol*. 2011;255(1):40-7.
132. Matsunaga T, Suzuki A, Kezuka C, Okumura N, Iguchi K, Inoue I, et al. Aldo-keto reductase 1B10 promotes development of cisplatin resistance in gastrointestinal cancer cells through down-regulating peroxisome proliferator-activated receptor- γ -dependent mechanism. *Chem Biol Interact*. 2016;256:142-53.
133. Ma L-N, Ma Y, Luo X, Ma Z-m, Ma L-N, Ding X-C. AKR1B10 expression characteristics in hepatocellular carcinoma and its correlation with clinicopathological features and immune microenvironment. *Scientific Reports*. 2024;14(1):12149.
134. Ye X, Li C, Zu X, Lin M, Liu Q, Liu J, et al. A Large-Scale Multicenter Study Validates Aldo-Keto Reductase Family 1 Member B10 as a Prevalent Serum Marker for Detection of Hepatocellular Carcinoma. *Hepatology*. 2019;69(6):2489-501.
135. Kossatz U, Breuhahn K, Wolf B, Hardtke-Wolenski M, Wilkens L, Steinemann D, et al. The cyclin E regulator cullin 3 prevents mouse hepatic progenitor cells from becoming tumor-initiating cells. *J Clin Invest*. 2010;120(11):3820-33.

Supplementary figures

Input in cBioPortal							Output (cBioPortal)		Study
Sample ID	Cancer Type	Chromosome	Start position	End Position	Reference allele	Variant allele	Protein	Gene	
T253	HB	2	178098945	178098945	G	C	G31A	NFE2L2	Eichenmüller et al. 2014
T577	HB		178098807	178098807	T	C	R34G		
TLT-004	HB		178098945	178098945	G	C	R34G		Sumazin et al. 2017
TLT-053	HB		178098960	178098960	C	T	D29N		
TLT-058	HB		178098945	178098945	G	C	R34G		
TLT-055	HB		178098945	178098945	G	C	R34G		
3676	HB		178098804	178098804	C	T	G81S		Pire et al. 2024
3944	HB		178098944	178098944	C	T	R34Q		
5043	HB		178098815	178098815	T	C	D77G		
5233	HB		178098960	178098960	C	T	D29N		
5377	HB	19	10610243	10610243	A	T	M156K	KEAP1	

Figure 19 Genetic alterations in NFE2L2/KEAP1 mutated patients. Data are retrieved from 3 studies: Eichenmüller et al., 2014, Sumazin et al., 2017 and Pire et al., 2024 (14, 17, 25). This same table was fed into cBioPortal website in order to visualize all mutations in a lollipop plot figure.

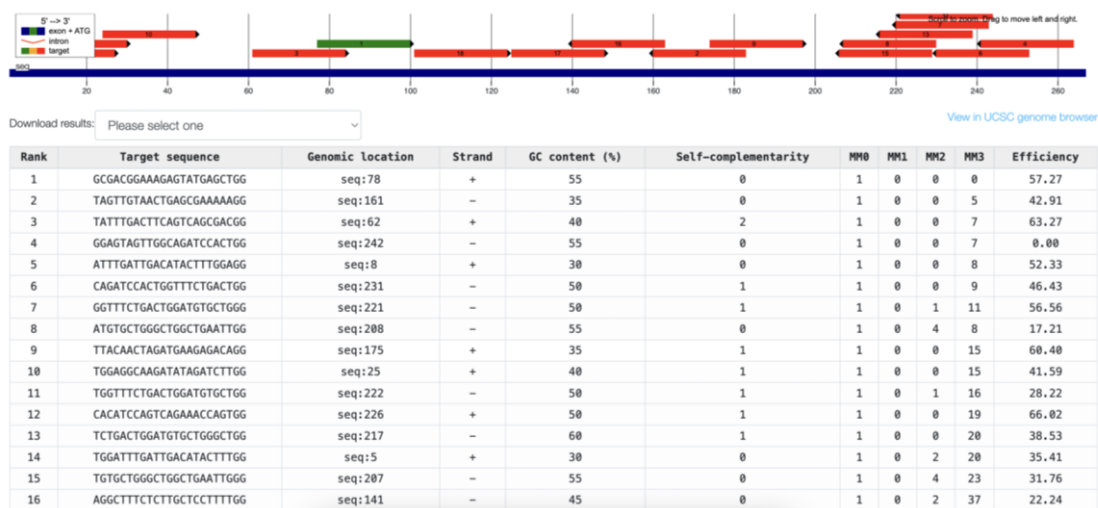


Figure 20 Identification of gRNAs in NFE2L2 gene using ChopChopTool. The figure displays all possible gRNA targeting the exon 2 of the NFE2L2 gene ranked by number of mismatches (off-target sites). Additional information is provided as GC content, self-complementarity and efficiency. The only one gRNA with 0 mismatches is shown in green.

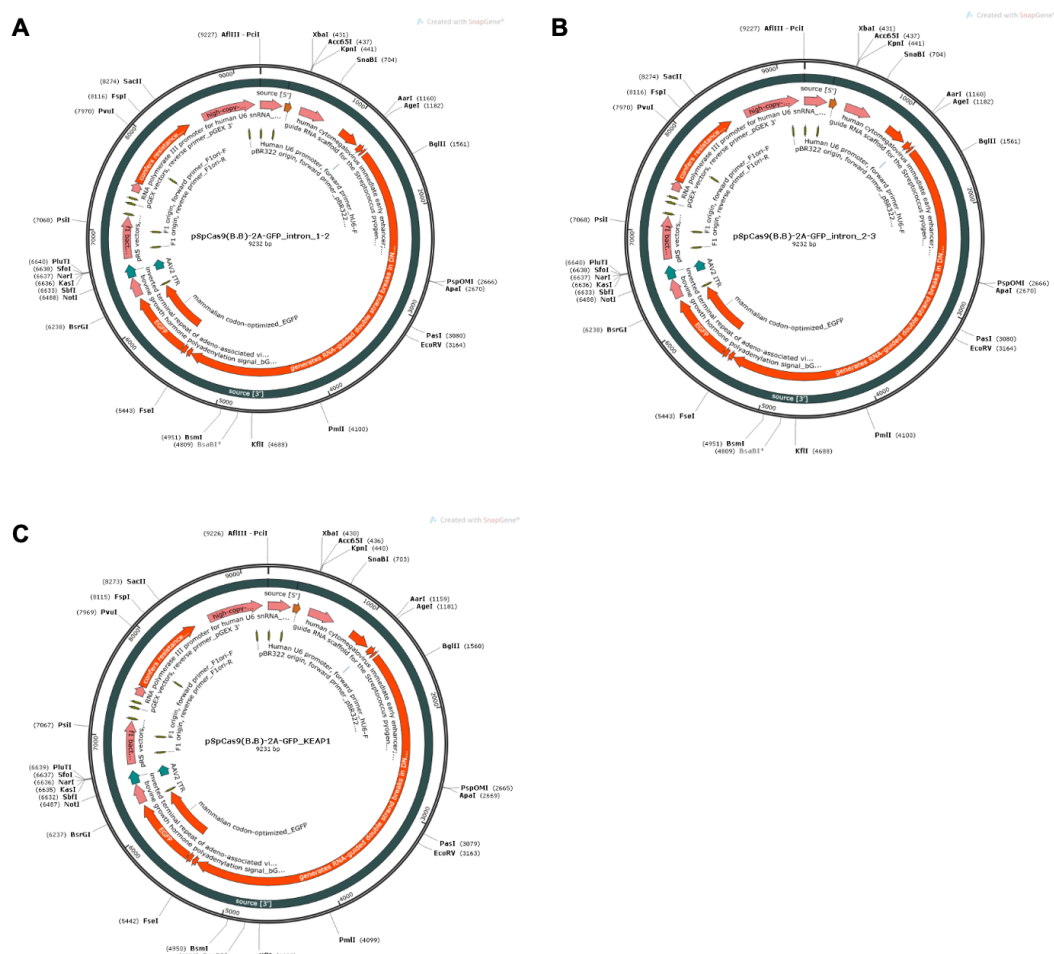


Figure 21 Plasmid maps of designed vectors. **A** pSpCas9(B.B)-2A-GFP_intron_1-2 and **B** pSpCas9(B.B)-2A-GFP_intron_2-3 were designed to cut the introns flanking exon 2 of the NFE2L2 gene. **C** pSpCas9(B.B)-2A-GFP_KEAP1, at the bottom, was designed to insert frameshift mutation in the exon 3 of the KEAP1 genome.

Commonly up-regulated genes log2FoldChange		
Genes	6 WT vs 6 NFE2L2	4 WT vs 4 KEAP1
AKR1B10	6.90	7.67
NMRAL2P	4.31	5.21
TRIM16L	4.77	2.60
PTGR1	3.19	3.88
TRIM16	3.75	4.84
SRXN1	2.43	2.42
TXNRD1	1.71	2.22
TALDO1	2.47	2.28

Figure 22 Commonly up-regulated genes in NFE2L2/KEAP1 models. Table representing the log2FoldChange values of commonly up-regulated genes that were found in 6

NFE2L2 clones and 4 KEAP1 clones. Each column represents the log2FoldChange expression level of these genes in the corresponding sample.

50 up regulated genes fed into cMap

T253 NFE2L2 mut. vs 10 WT	T577 NFE2L2 mut. vs 8 WT	HepT1 NFE2L2 mut. vs 6 WT	6 WT vs 6 NFE2L2	4 WT vs 4 KEAP1
FGF8	AKR1B10	TXNRD1	OSGIN1	CALB2
NQO1	UGDH	SLC4A3	GLA	F2RL2
GAD1	ALDH3A1	SYTL2	TALDO1	CDR2L
TRIM16	NECAB2	TRIM16	NCF2	TALDO1
PCSK2	SULT2A1	TLL1	AKR1B10	OSGIN1
KRT31	PZP	TRIM58	HHIPL2	NCF2
HOXC5	TGM3	C1R	TRIM16	FECH
CPLX2	ALDH1A1	HAO2	KEAP1	TXN
FGF9	FN1	NELFCD	KRT7	AKR1B10
EEF1A1	MAPT	MTMR10	F2RL2	GPI
G6PD	TMPRSS3	PDE8B	ABCB6	G6PD
DYM	UGT2B4	SLC9A7	GPNMB	ABCB6
GABRA3	RAD54L2	BARX1	FECH	TUBAL3
PLD2	DDI2	TP53I3	LAT2	HHIPL2
TKT	CYP3A43	DLGAP1	SQSTM1	GLA
PRSS3	FLNC	GLA	EPHX1	PGD
MPZ	CABYR	RPS6KC1	NECAB2	BLVRB
CELSR3	ARHGAP44	BCAS4	FTL	ATP1A2
AKR1B10	FGG	HAMP	PGD	BMP6
KRT5	EBLN2	ABCC5	S100A2	GSR
EEF1B2	APOA4	AP5S1	NPM3	SQSTM1
HSPA6	CLIP1	MAPK9	MAFG	ANXA1
MFNG	PSME4	RUFY2	HRASLS2	TXNRD1
UGDH	TXNRD1	OSGIN1	CLTB	KIAA0319
POPDC3	PNRC1	ETFB	PIR	GCNT3
CRH	SCUBE2	NPR2	WDR46	AKR1C2
RPL29	ALDH1L1	ABCD3	LY9	ATP5G1
GABRA4	ABCB11	CALHM2	GSR	TYRO3
BCAN	BACH1	BMP6	HN1	GPRC5A
XRCC1	SLC25A30	SDHB	SHC1	LETMD1
PRDX1	GGCX	RHBDF1	PPCDC	MAPRE3
DLX2	KBTBD11	TALDO1	NME1	TRIM29
CPVL	EVPL	DTNA	TMEM147	PIR
GDF10	CES1	NUDT11	MAP7D1	CIB1
CNR1	EGF	CDKL5	GPI	TRIM16
GORASP2	GCLC	TAOK3	VAR5	TKT
TMC5	OSGIN1	PGD	ENO1	KRT15
GPX2	FUT2	UBOX5	MTA2	NECAB2
NXPH4	HSD17B6	MED12	S100A6	CYP26A1
SST	FGB	DNM1	TMEM14B	ATP1A3
ABCA4	TALDO1	TNN	EXOSC5	ENO1
RPSA	ACSF2	ZNF335	PPME1	EMP3
CHL1	FMO5	CCNO	NHP2	B4GALNT1
NAALADL1	PPBP	LAMB4	SIRT7	EPHX1
EIF3E	ZZEF1	DOCK3	SPSB1	NPM3
CCR6	SCNN1B	AKR1B10	PPP1R14B	PPME1
AACS	SEC24A	ALDH2	TXN	MUC4
PFKFB4	SOD2	GLTSCR1	RPS10	DUSP13
CDH12	CHIT1	CYP4F2	TKT	DCPS
AFP	KEAP1	KEAP1	DUSP13	B9D1

Figure 23 Lists of top 50 up-regulated genes fed into CMap. The table displays the top 50 up-regulated genes identified in three NFE2L2-mutated patients (T253, T577, HepT1) and 6 NFE2L2-mutated models, normalized against 6 WT cell lines/PDXs. Additionally, the table includes genes from 4 KEAP1-mutated models, normalized to 4 WT cell lines. These genes were subsequently used as input in the CMap for in silico drug prediction.

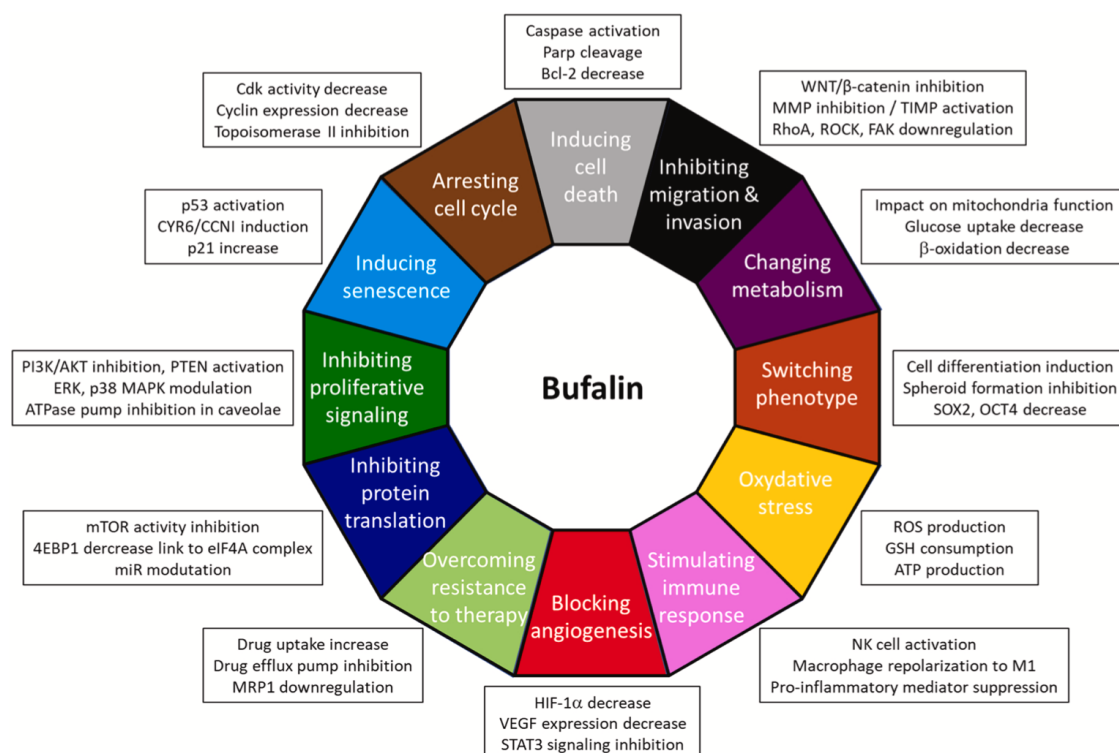
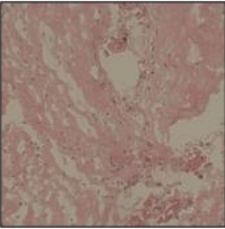
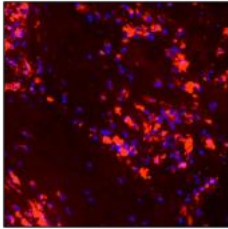
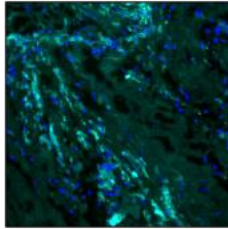
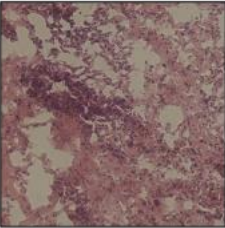
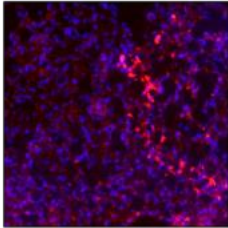
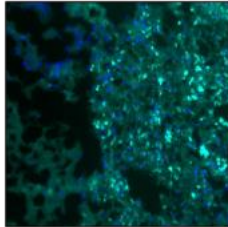
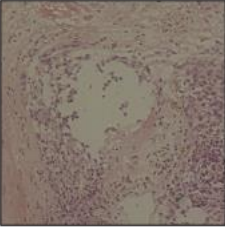
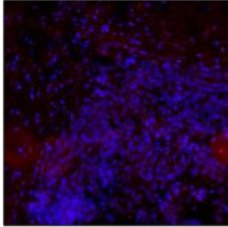
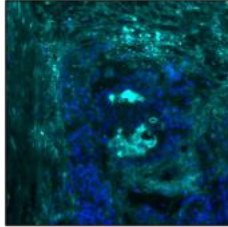
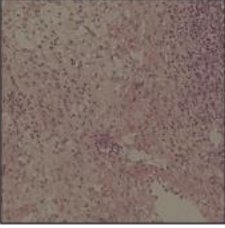
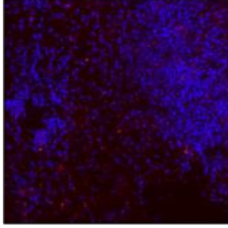
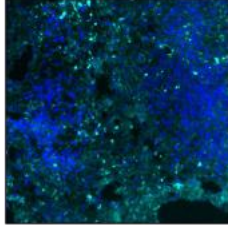
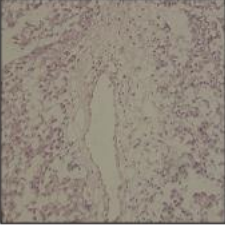
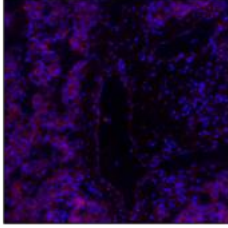
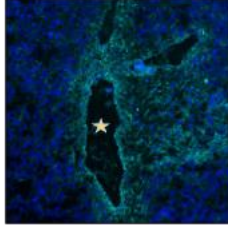
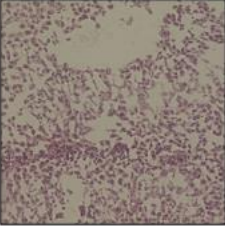
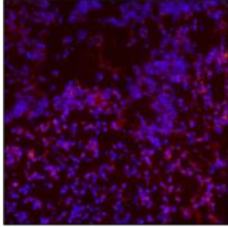
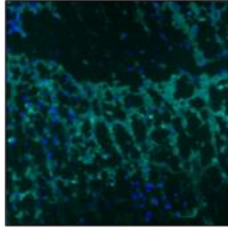
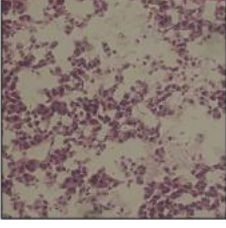
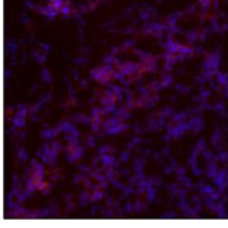
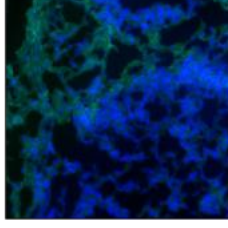
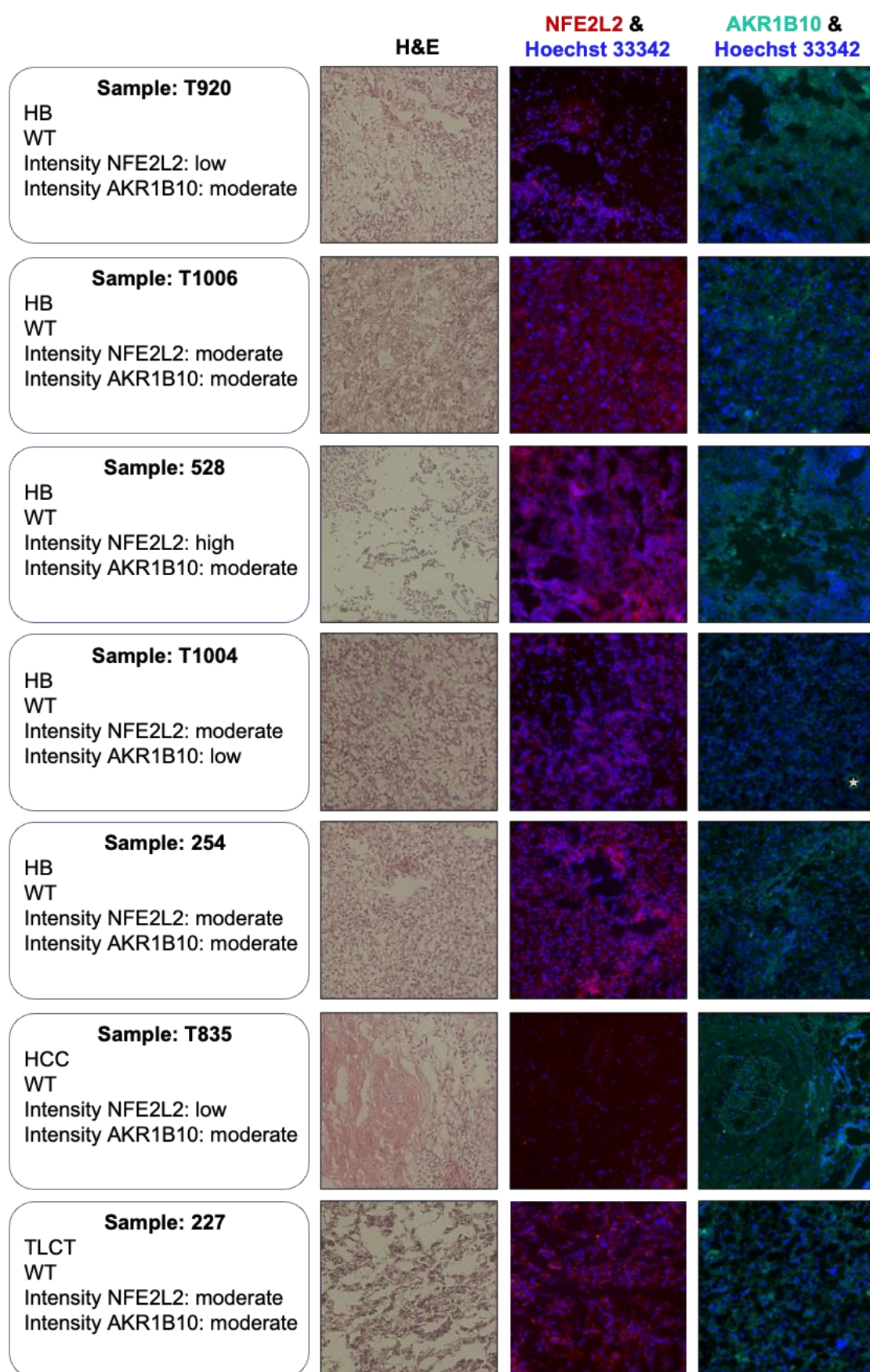


Figure 24 Hallmarks of bufalin against cancer. Figure retrieved from Soumoy et al., 2022 (104).

	H&E	NFE2L2 & Hoechst 33342	AKR1B10 & Hoechst 33342
Sample: T1100 HB WT Intensity NFE2L2: high Intensity AKR1B10: high			
Sample: T629 HB WT Intensity NFE2L2: high Intensity AKR1B10: high			
Sample: T1152 TLCT WT Intensity NFE2L2: low Intensity AKR1B10: high			
Sample: Tü7 HB R34P Intensity NFE2L2: moderate Intensity AKR1B10: high			
Sample: Tü6 HB WT Intensity NFE2L2: moderate Intensity AKR1B10: low			
Sample: T1120 HB WT Intensity NFE2L2: moderate Intensity AKR1B10: moderate			
Sample: T291 TLCT WT Intensity NFE2L2: moderate Intensity AKR1B10: low			



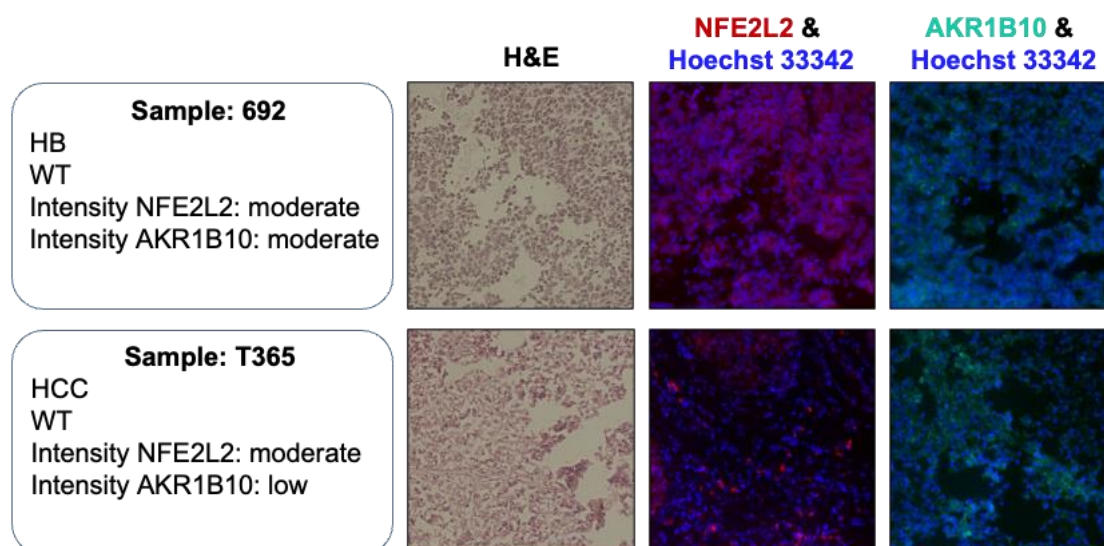


Figure 25 16 human liver cancer tissues analysed using H&E and IF. The first column displays general information about each tissue, the second column shows the H&E staining, the third column displays Hoechst 33342 and NFE2L2 fluorescence, while the fourth column shows Hoechst 33342 alongside AKR1B10 fluorescence. Hoechst staining highlights nuclear structures in blue, providing partial information about cellular architecture. NFE2L2 is predominantly localized to the nuclei and cytoplasm, exhibiting variable intensities across tissues, which were categorized into three levels: high, moderate and low. AKR1B10 displays cytoplasmic staining primarily in hepatocytes, with strong signals concentrated around the periportal zones (highlighted with a star). Its intensity was similarly classified into high, moderate and low levels.

Acknowledgements

I would like to thank **Prof. Dr. med. Oliver Muensterer**, Director of the Department of Pediatric Surgery at Dr. von Hauner Children's Hospital in Munich, for giving me the opportunity to conduct my research at his institution.

My sincere thanks go to **Prof. Dr. rer. nat. Roland Kappler**, whose guidance has been essential to my growth as a scientist. His support, advice, and belief in my work have greatly helped me throughout this journey. I am especially grateful for his open-door policy; whenever I needed help, he always made time to sit down with me and work through the challenges. I could not have completed this work without his support.

I would like to express my gratitude to my Thesis Advisory Committee members, **Prof. Dr. med. Irene Schmid** and **Dr. rer. biol. hum. Ivonne Regel**, for their curiosity about my work and insightful feedback during our TAC meetings. Their encouragement and expertise have been important in shaping the direction and progress of my research.

I want to acknowledge the valuable contributions of the members of the Kappler group. First of all, I am grateful to **Dr. Salih Demir**, who was always ready to teach me new methods and help improve my data analysis skills. I truly admire his working style and tried to learn as much as I could from him. Secondly, a big thank you goes to **Alina Hotes** and **Tatja Schmid**, who made sure I had all the reagents and lab materials needed to keep my experiments running smoothly. I also want to thank **M.Sc. Negin Razizadeh**, who has shared this PhD journey with me from the start. We faced many similar struggles, and it was a great support to have someone who understood the challenges of this process.




I would like to thank **Dr. Masayuki Yamamoto** (Tohoku University, Japan) for providing the pNQO1-ARE-Luc plasmid, **Dr. Torsten Pietsch** (University of Bonn, Germany) for the HepT1 cell line and **Xentech** (Evry, France) for providing the patient-derived xenograft models.

This thesis is dedicated to all families with children affected by hepatoblastoma. It is my hope that this work contributes, even in a small way, to advancing treatments for children battling this disease. During the challenges of my PhD journey, I often reminded myself

that this research could one day make a difference in the life of a child with hepatoblastoma. That thought has been my constant source of motivation and purpose. The motivation, ethical and honest way I approach my work has been deeply shaped by Prof. Dr. rer. nat. Roland Kappler, whose example constantly reminded me that everything we do is ultimately for the benefit of the patients.

Finally, I would like to thank my family (Elena, Mihail and Natalia) and friends (Paul S., Chiara L., Andrej M., Océane S., Florian B., Lorenzo M., Stella C., Marc P., Francesco B., Giacomo F., Luana G., Alessandro M., Valeria A., Stefan B., Agustin C., Ludwig G., Denis G., Andres C., Filipe S., and everyone else). I am truly lucky and grateful to have you all in my life. Lastly, I want to thank my partner Katsiaryna K., who always believed in me and was there in the most difficult times, your patience and encouragement have been a constant source of strength and motivation. I am deeply thankful for the time we have shared over the past years, you have been the best partner I could have ever wished for.

Affidavit

	LUDWIG- MAXIMILIANS- UNIVERSITÄT MÜNCHEN	Promotionsbüro Medizinische Fakultät		
Affidavit				

Rotari Andrei

Surname, first name

Schwanthalerstr. 74

Street

80336, Munich, Germany

Zip code, town, country

I hereby declare, that the submitted thesis entitled:

Identifying therapeutic agents targeting NFE2L2/KEAP1-mutated pediatric liver tumors

is my own work. I have only used the sources indicated and have not made unauthorised use of services of a third party. Where the work of others has been quoted or reproduced, the source is always given.

I further declare that the dissertation presented here has not been submitted in the same or similar form to any other institution for the purpose of obtaining an academic degree.




Munich, 11.09.2025

place, date

Andrei Rotari

Signature doctoral candidate

Confirmation of congruency

	LUDWIG- MAXIMILIANS- UNIVERSITÄT MÜNCHEN	Promotionsbüro Medizinische Fakultät	 
<p align="center">Confirmation of congruency between printed and electronic version of the doctoral thesis</p>			

Rotari Andrei

Surname, first name

Schwanthalerstr. 74

Street

80336, Munich, Germany

Zip code, town, country

I hereby declare, that the submitted thesis entitled:

Identifying therapeutic agents targeting NFE2L2/KEAP1-mutated pediatric liver tumors

is congruent with the printed version both in content and format.

Munich, 11.04.2025

place, date

Andrei Rotari

Signature doctoral candidate

List of publications